ABSTRACT

Title of thesis:	CONTRIBUTIONS TO THE UNDERSTANDING OF WIND TURBINE AERODYNAMICS USING A RANS SOLVER WITH TRANSITION MODELING
	Taylor Jay Rinehart, Master of Science, 2014
Thesis directed by:	Dr. James D. Baeder Department of Aerospace Engineering

Wind turbine sizes have been steadily increasing to reduce the cost of generating electricity using wind energy. The increased wind turbine blade size has led to increased interest in the accurate prediction of the aerodynamics of large wind turbine blades. In this work, two-dimensional simulations of wind turbine airfoils and three-dimensional simulations of the Sandia $100\,\mathrm{m}$ wind turbine blade were conducted. The focus of the simulations was to evaluate improvements in turbulence modeling for wind turbine applications. The flow field was modeled using a Reynolds-Averaged Navier–Stokes flow solver. The turbulence model included transition modeling to capture the significant regions of laminar flow found on wind turbine airfoils and wind turbine blades. The turbulence model was also modified to increase sensitivity to adverse pressure gradients. The effects of modifying the turbulence modeling were quantified using lift and drag for two-dimensional simulations while wind turbine thrust and power were used as metrics for three-dimensional simulations. The two-dimensional studies showed that the adverse pressure gradient

correction lowered lift predictions post-stall by about 13%, significantly reducing lift over-prediction and bringing simulations closer to experimental results. Transition modeling lowered drag predictions by 30% to 50% at low angles of attack bringing the predicted values into good agreement with experimental results. The addition of transition modeling in the three-dimensional simulations increased the predicted thrust by 1% to 3% and predicted power by 3% to 6%. The extent of laminar flow was visualized using intermittency. Laminar flow was observed on large portions of the Sandia 100 m blade at normal operating conditions. A preliminary study on the effects of leading edge tubercles on the Sandia 100 m blade was performed, no significant changes in wind turbine performance were observed at nominal operating conditions.

CONTRIBUTIONS TO THE UNDERSTANDING OF WIND TURBINE AERODYNAMICS USING A RANS SOLVER WITH TRANSITION MODELING

by

Taylor Jay Rinehart

Thesis submitted to the Faculty of the Graduate School of the
University of Maryland, College Park in partial fulfillment
of the requirements for the degree of
Master of Science
2014

Advisory Committee:
Dr. James D. Baeder, Chair/Advisor
Dr. Christopher Cadou
Dr. Anya Jones

Acknowledgments

I would like to express my gratitude to my advisor, Dr. James Baeder, for the opportunity to pursue research under his guidance. He has taught me a great deal through his insights and discussions about various research problems. I would also like to thank my thesis committee members, Dr. Christopher Cadou and Dr. Anya Jones for their time serving on my committee and for their feedback on my research.

Thank you to my friends and colleagues for two wonderful years of graduate school. Finally, none of this would have been possible without the support and encouragement of my friends and family back home, thank you.

Table of Contents

List of Figures

Nomenclature

a	Speed of sound $= \sqrt{\gamma R T}$
c	Chord length
C_d	Sectional drag coefficient
C_f	Skin friction coefficient
C_l	Sectional lift coefficient
C_p	Pressure coefficient
d	Nearest wall distance
e	Internal energy
L	Reference length
M	Mach number
p	Static pressure
Pr	Prandtl number
Re	Reynolds number $= \dfrac{\rho_\infty U_\infty L}{\mu_\infty}$
Re_θ	Reynolds number based on momentum thickness $= \dfrac{\rho_\infty U_\infty \theta}{\mu_\infty}$
$Re_{\theta t}$	Reynolds number at transition onset location
$\overline{Re_{\theta t}}$	Transport variable for $Re_{\theta t}$
Re_ν	Vorticity Reynolds number $= \dfrac{\rho d^2 \Omega}{\mu}$
t	Time
$\mathbf{T}, \mathbf{T}^{-1}$	Matrix of left and right eigenvectors respectively
Tu	Turbulence intensity
u, v, w	Cartesian components of flow velocity
u', v', w'	Cartesian components of turbulent fluctuation velocity
U	Velocity magnitude
U'	Turbulent fluctuation velocity magnitude
x, y, z	Cartesian coordinate directions

Symbols

γ	Ratio of specific heats / Intermittency
λ	Eigenvalue
Λ	Diagonal matrix of eigenvlaues
μ	Molecular viscosity
μ_t	Turbulent viscosity / Eddy viscosity
ν	Kinematic viscosity
ρ	Density
τ_{ij}	Viscous stress tensor

Subscripts

∞	Freestream flow variables

Abbreviations

AoA	Angle of attack
APG	Adverse Pressure Gradient
CPU	Central Processing Unit
DDES	Delayed Detached Eddy Simulation
DNS	Direct Numerical Simulation
DOWEC	Dutch Offshore Wind Energy Convertor
FVM	Free-Vortex Method
GPU	Graphics Processing Unit
LES	Large Eddy Simulation
MUSCL	Monotone Upstream-centered Schemes for Conservation Laws
NREL	National Renewable Energy Laboratory
OverTURNS	Overset Transonic Unsteady Rotor Navier–Stokes
RANS	Reynolds–Averaged Navier–Stokes

Chapter 1: Introduction

1.1 Motivation

The demand for energy is constantly increasing and wind based energy technology can be leveraged as an alternate source of sustainable energy to alleviate the dependence on energy generation based on fossil fuels. Currently, the price of electricity generated using wind based energy is still higher than the price of electricity generated using conventional methods, such as coal and natural gas [1]. One of the primary goals of wind turbine research is to reduce the aforementioned cost of generating electricity, and thus increase the economic viability of wind energy. Because the amount of energy extracted by a turbine is proportional to the square of the rotor diameter, an increase in rotor size leads to increased energy extraction per turbine. Therefore, to reduce the cost of using wind energy to generate electricity, the size of wind turbines has steadily increased. Current utility scale turbines have rotors around $120\,\mathrm{m}$ in diameter and are rated to generate a maximum of $5\,\mathrm{MW}$ to $6\,\mathrm{MW}$ of power [2]. A representative illustration of the increase in wind turbines sizes and their associated rated power is shown in Fig. 1.1.

The major limiting factor against increasing wind turbine size is based on the square-cube law, which states that while the energy output of wind turbines increases
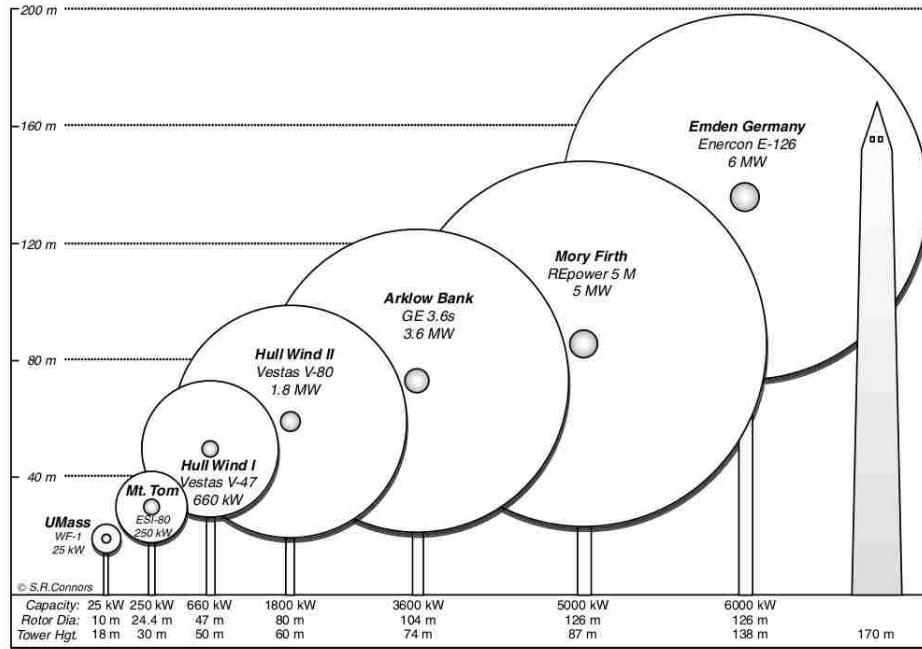
Figure 1.1 – Representative size, height, and diameter of several wind turbines (Reproduced from Ref. [2])

with the square of the rotor diameter (i.e., proportional to the rotor swept area), the mass and cost of the wind turbine, which are based on the volume of material used, increases with the cube of the rotor diameter [1]. One problem with increasing the blade mass is that the associated increase in gravitational loads causes the root bending moment of the blade to grow. In fact, the root bending moment due to gravitational loads increases with the rotor diameter to the fourth power while the root bending moment due to aerodynamic loads increases with the rotor diameter cubed. The result is that increasing blade size leads to a relative increase in the importance of gravitational loads compared to aerodynamic loads. The implication is that gravitational loads are becoming an increasingly important design constraint. To overcome this, new blade materials and blade shapes are being investigated to

minimize increases in gravitational loads due to increases in turbine size. Advanced carbon composites, such as carbon fiber [3], and modifications to the blade shape, such as flatback airfoils [4]–[6], have been investigated as part of the drive to lower the blade mass for a given rotor size. These technologies have resulted in an increase in the wind turbine generation capacity with an associated decrease in the cost per unit of power output [1].

Increasing the blade size has several important implications. An increase in the length of wind turbine blades while minimizing the increase in mass tends to increase the blade flexibility, which can affect the structural and aeroelastic properties of the blades. Aerodynamically, an increase in blade length is accompanied by an increase in both the tip Reynolds number and the tip speed (at the same rotational frequency), which has several important effects on the flow characteristics along the surface of the blade. For instance, compressibility effects on the blades are directly associated with the operating tip speed of the turbine. Lower tip speeds imply that the flow can be treated as incompressible, but as the tip speed increases, it becomes more important to consider compressibility effects when predicting blade aerodynamic performance. Reynolds number affects the extent of stalled flow on the blade and is also a critical parameter in determining the transition between laminar to turbulent flow along the blade surface. The Sandia $100\,\mathrm{m}$ blade is an example of a next generation utility scale wind turbine blade and it operates with Reynolds number between 3×10^6 and 5×10^6 and a tip Mach number between 0.136 and 0.233, which is approaching the upper limit of Mach numbers where the incompressible assumption is valid [7]. In an effort to reduce profile drag and maintain laminar

flow over the airfoil, wind turbine airfoils are designed with a high thickness-to-chord ratio (e.g., the S809 wind turbine airfoil is 21% thick). Furthermore, thicker airfoils allow for stiffer wind turbine blades. Flow transition has a significant effect on the performance of wind turbine airfoils because of the large laminar regions (e.g. up to 50% of the chord on the S809 airfoil [8]) on the airfoil. Changes in the laminar to turbulent transition location affect wind turbine performance by changing the skin friction coefficient distribution along the surface, which affect the net airfoil drag, and by extension the power produced by the wind turbine. Laminar to turbulent transition can also affect the wind turbine performance by changing the location and size of the laminar separation bubbles that form on the blade surface.

Performance of wind turbines can be evaluated by performing experiments on wind turbine models or on full scale wind turbines in field tests. An advantage of experimental studies is the ability to accurately capture effects of flow separation and flow transition. However, experimental tests on modern utility-scale turbines are not currently feasible because of physical limitations in size of wind tunnels. The Full-Scale Aerodynamics Complex at NASA Ames Research Center is currently the largest wind tunnel in the world [9], and it has a test section $24.4\,\mathrm{m} \times 36.6\,\mathrm{m}$, while the latest generation of utility scale turbines have rotor diameters around $120\,\mathrm{m}$. The National Renewable Energy Laboratory (NREL) Unsteady Aerodynamics Experiment Phase VI [10] is an example of the extensive data that can be gathered using experiments on a geometrically scaled down wind turbine. The timeline of the NREL Phase VI project involved several years for the planning the experiments, set up the equipment, and the generation of data. Furthermore, it also required the

use of the National Full-Scale Aerodynamics Complex, which is shown in Fig. 1.2 to illustrate the size of the wind turbine tested. The NREL Phase VI project highlights a major limitation of experimental studies, namely the amount of time and infrastructure required for its implementation. Field tests, like those in the NREL Combined Experiment Phase II [11], can be used to gather data on full scale turbines while they are operating. However, a significant limitation in field studies is the ability to control the incoming free-stream conditions, such as wind speed, direction and levels of free-stream turbulence. This lack of experimental control makes it difficult to study specific operating conditions of interest, particularly for operating points that occur outside the range of common wind speeds. Similar to experimental studies, field tests are also limited by the amount of time and equipment necessary to instrument a wind turbine.

The limitations of experiments and field tests, particularly during the wind turbine design phase, are overcome using simplified aeroelastic models developed to quickly evaluate the aerodynamic performance of wind turbine blades. Some examples include CAMRAD II [12, 13], a comprehensive rotorcraft analysis code, which includes a lifting line model for the near-blade aerodynamics coupled to a free-vortex wake method, and FAST [14,15], which utilizes the blade element momentum theory code AeroDyn [15,16]. The aerodynamic models utilized in these simplified models often require two-dimensional airfoil performance data, such as sectional lift, drag, and pitching moment. Performance tables for two-dimensional airfoils used on wind turbines have been generated experimentally in the past [8, 17]. However, even for two-dimensional airfoils the amount of time and infrastructure required to perform
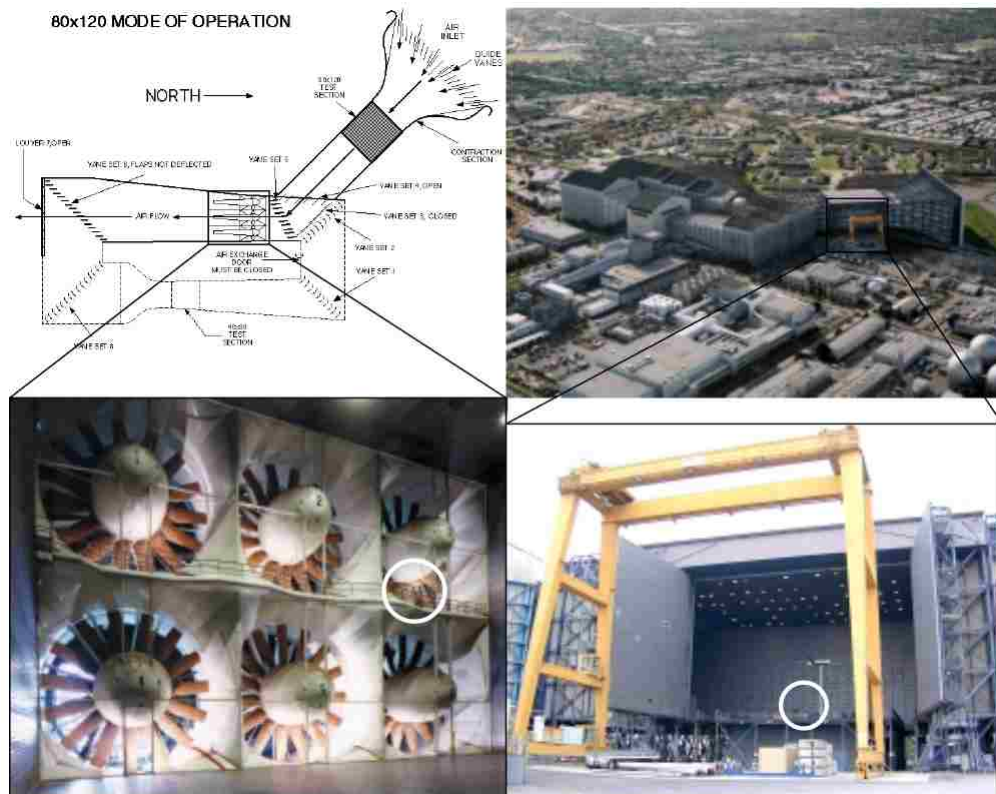
Figure 1.2 – NASA Ames Research Center Full-Scale Aerodynamics Complex in the $24.4\,\mathrm{m} \times 36.6\,\mathrm{m}$ mode of operation, note people for scale (Reproduced from Ref. [10])

experiments is significant. An alternative to experiments is to use computational fluid dynamics (CFD) simulations as a relatively inexpensive and faster method for generating the two-dimensional airfoil performance tables. Upon validation of the CFD methods using data from experimental results for the desired flow regime, the solver can then be used to produce performance data on a much larger range of airfoils.

Increasing the overall blade size generally increases both the blade flexibility and the aerodynamic loads on the blade [7]. The result is an increase in the importance of aeroelastic effects, such as aeroelastic flutter. Flutter is of particular concern because it can lead to the destruction of the wind turbine blade if the associated load fluctuations overcome the structural strength of the blade. Flutter occurs when there is not enough structural or aerodynamic damping to dampen relatively large vibratory motions caused by the interaction of aerodynamic forces with the structural dynamics of the blade. As blades approach aeroelastic design limits, such as when the margin between flutter onset speed and blade operating speed is narrow, simplified aerodynamic models are no longer sufficient to predict the complex flow fields and vortical structures around the blades [7, 18, 19].

Instead of relying on simplified aerodynamic models to predict wind turbine aerodynamic performance, full three-dimensional Navier–Stokes simulations can be used. Three-dimensional CFD simulations offer a high fidelity method for evaluating the aerodynamic performance of wind turbine blade designs. Unlike simplified models, CFD simulations can accurately capture non-linear and interactional aerodynamics, such as the spanwise flow along the blade. Three-dimensional CFD sim-
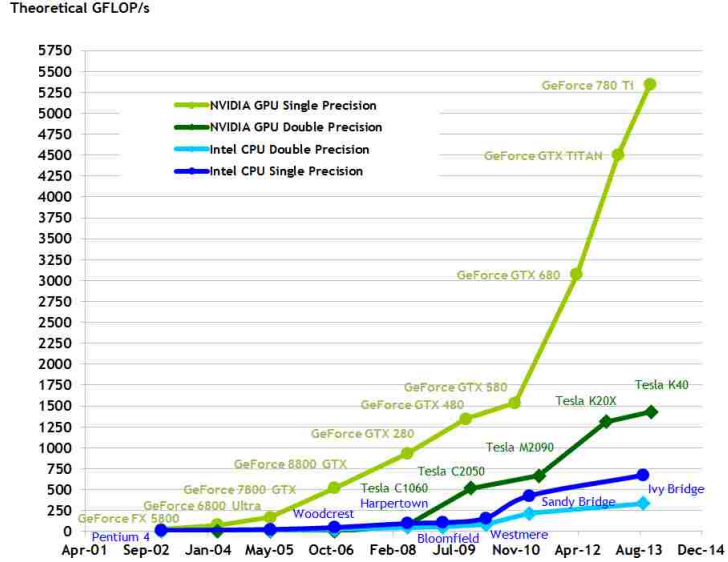
Figure 1.3 – Comparison of computing power for GPUs and CPUs since 2002, given as theoretical GFLOP/s (Reproduced from Ref. [20])

ulations also have advantages over experimental and field studies. One advantage is a smaller amount of time and infrastructure required compared to experimental and field studies. Another advantage of three-dimensional CFD simulations, particularly when compared to field studies, is the flexibility in the choice of operating conditions. However, it is important to validate the CFD solver using experimental data before relying on its predictions.

The cost of full three-dimensional Navier–Stokes simulations can be computationally expensive, especially for large intricate geometries. To reduce the computational cost, Graphics Processing Unit (GPU) based hardware acceleration is investigated. GPUs are designed to meet the demands of producing real-time, high-definition three dimensional graphics. Consequently, they are highly parallel processors with large numbers of cores and large memory bandwidth. It is useful
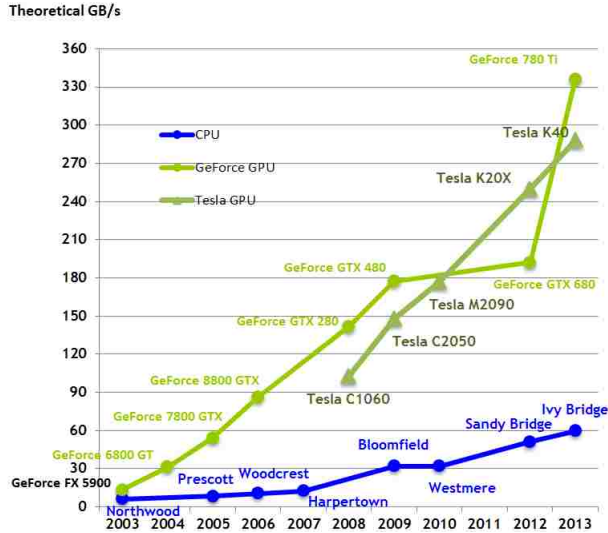
Figure 1.4 – Comparison of memory bandwidth for GPUs and CPUs since 2002, given as theoretical GB/s (Reproduced from Ref. [20])

to evaluate the advantages of GPU computing by comparing it with traditional CPU computing. A comparison between GPU and CPU (Central Processing Unit) computing power in shown in Fig. 1.3, where a single GFLOP/s is 10^9 FLOP/s (Floating-point Operations per second). The trend in computing power shows that GPUs have been equipped with higher computing power compared to CPUs since 2009, with current 2014 technology resulting in GPUs operating at over three orders of magnitude greater in GFLOP/s than their CPU counterpart. Similarly, Fig. 1.4 compares the memory bandwidth of GPUs and CPUs, showing that the GPU memory bandwidth is significantly higher than CPU memory bandwidth, which implies that GPUs can access data for computations at a significantly higher rate, improving computation speed. The combination of significantly higher memory bandwidth and computational power allows for large decreases in simulation execution time by properly utilizing GPU resources.

9

In summary, the goal of reducing wind energy generation costs is the primary driver of increasing wind turbine sizes. The increasing blade size increases the importance of accurately understanding the physical effects of transition and separated flow. Large wind turbine blade sizes prevent full scale experimental tests and performance tests at specific operating points cannot be performed on turbines in the field, as a result alternative methods of evaluating wind turbine blades are required. Simplified aeroelastic models are an alternative that allows for wind turbine performance to be evaluated quickly. However, simplified aeroelastic models do not capture transition and the increased blade sizes result in higher blade flexibility and larger aerodynamic loads on the blade, affecting the accuracy of simplified aeroelastic model wind turbine performance predictions. Three-dimensional CFD simulations are useful for investigating transition and capturing wind turbine performance in situations where the simplified aeroelastic models are no longer applicable. The additional computing power required by CFD simulations over the simplified models can be offset by utilizing GPU based hardware acceleration.

1.2   Literature Review

The present work focuses on utilizing CFD to improve the aerodynamic performance predictions for contemporary wind turbine blade designs. To ensure the CFD simulations accurately predict the aerodynamics of the blade, the CFD solver must be validated using experimental results. Results from NREL experiments on wind turbine airfoils and full wind turbines are a key component of the validation.

The limitations of simplified aerodynamic modeling from previous works have been explored using a comparison of the model predictions of the NREL Phase VI wind turbine to the experimental results. Previous works on transition modeling aimed at improving the CFD aerodynamic predictions is investigated. In addition, background on the application of GPU based hardware acceleration to CFD is provided. Finally, information on the geometry of the wind turbine blade studied in this work is provided along with information on the usage of leading edge tubercles.

1.2.1   Experimental Studies

This section focuses on past experimental studies conducted on two-dimensional wind turbine airfoils and full-scale wind turbines. Important results from the S809 and S827 wind turbine airfoil experiments are shown and discussed. In addition, background on both the NREL Phase VI and the NREL Phase II experiments is discussed, as well as the role of the NREL Phase VI in CFD validation.

1.2.1.1   Wind Turbine Airfoils

It should be noted that the design requirements for wind turbine airfoils do not match the criteria of aircraft airfoils [8]. Typically, airfoils used in aircraft/rotorcraft are designed with an emphasis on robustness as these airfoils are required to operate efficiently in a wide range of aerodynamic and freestream conditions. Wind turbine airfoils, however, are designed to operate highly efficiently at a "point" design condition with much less emphasis on off-design performance. For instance, the primary
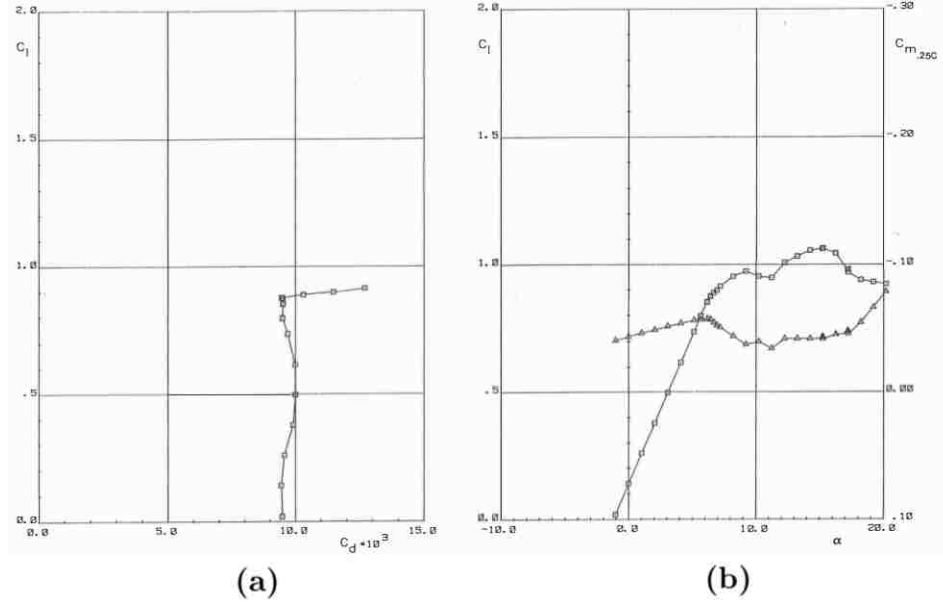
Figure 1.5 – S809 experimental results at Re $= 1 \times 10^6$; (a) drag polar, and (b) lift and pitching moment coefficient, for various angles of attack (Reproduced from Ref. [8])

design goals of the S809 airfoil are low profile drag and a restrained maximum lift [8], while the primary goals of the S827 airfoil are docile stall characteristics and low profile drag [17] which minimizes the power losses because of aerodynamic drag.

The experimental results for the S809 show a restrained maximum lift and low drag coefficients, which can be seen in the plots of lift coefficient and drag coefficient in Fig. 1.5 for Re $= 1 \times 10^6$. A comparison of the S809 and NACA 4421 lift and drag coefficients at Re $= 3 \times 10^6$ is shown in Fig. 1.6, where it is seen that the S809 generates lower lift coefficients and also has significantly lower drag coefficients for most of the operating region. The differences between the performance characteristics of the S809 and the NACA 4421 airfoils highlights how wind turbine airfoils are designed for different operating conditions than typical

12
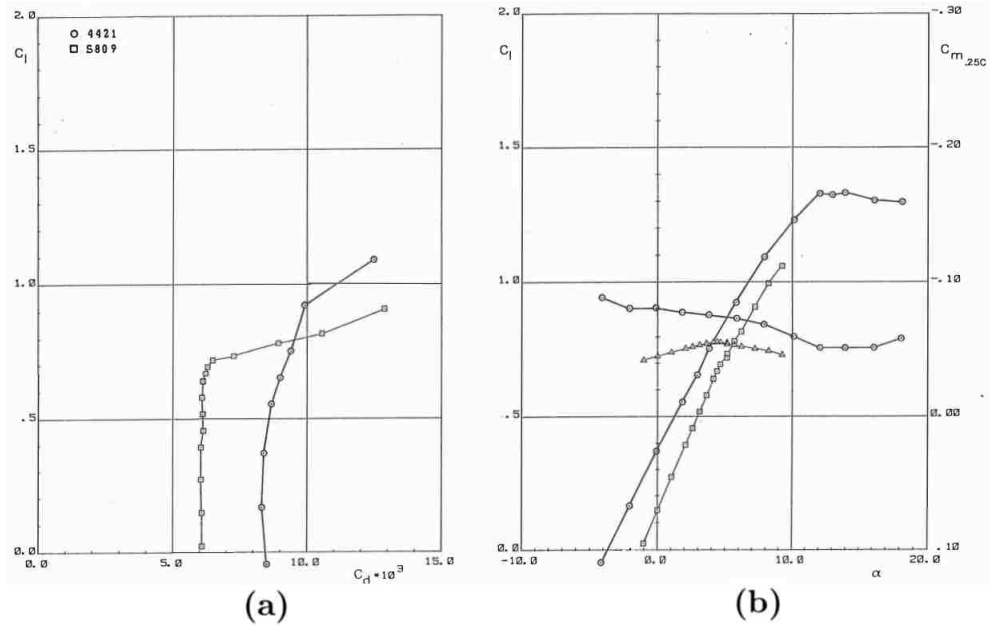
Figure 1.6 – Comparison of the S809 results to NACA 4421 results at Re $= 3 \times 10^6$; (a) drag polar, and (b) lift and pitching moment coefficient, for various angles of attack (Reproduced from Ref. [8])
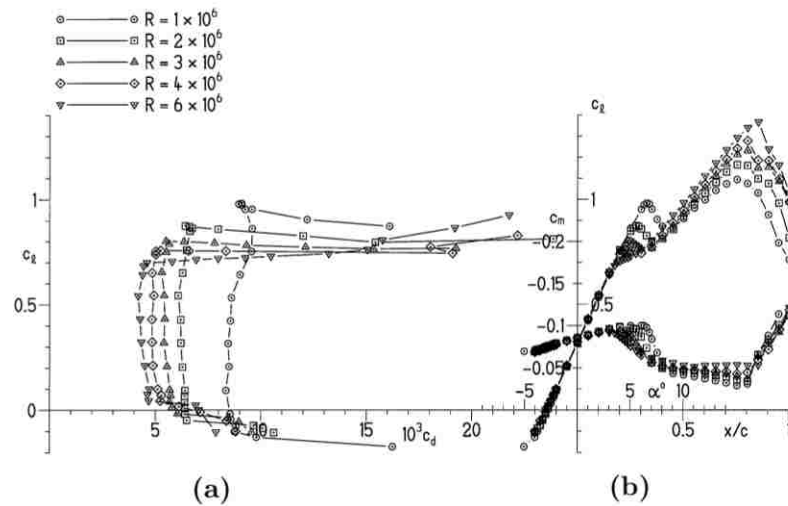
Figure 1.7 – S827 experimental results for Re $= 1 \times 10^6$ to Re $= 6 \times 10^6$; (a) drag polar, and (b) lift and pitching moment coefficient, for various angles of attack (Reproduced from Ref. [17])

13
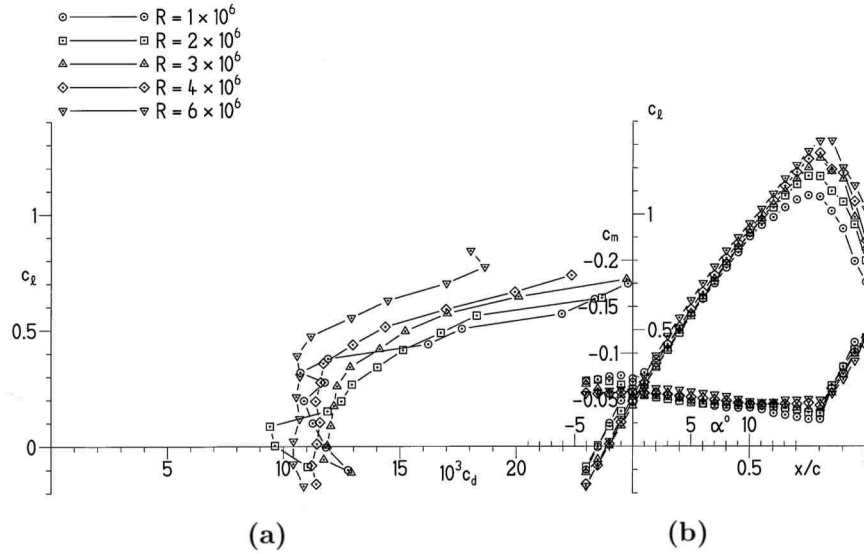
Figure 1.8 – S827 experimental results with a fixed transition location for Re = 1×10^6 to Re = 6×10^6; (a) drag polar, and (b) lift and pitching moment coefficient, for various angles of attack (Reproduced from Ref. [17])

aerospace airfoils.

The lift and drag coefficients measured by the S827 experiment are shown in Fig. 1.7, which also shows low drag coefficients as well as docile stall characteristics for Re = $1 \times 10^6 - 6 \times 10^6$. The effect of Reynolds number can be seen, increasing the Reynolds number reduces lift coefficient (and by extension, angle of attack) required to produce separated flow. The onset of significant levels of separated flow can be seen as the sudden increase in drag coefficient. Another important issue highlighted in the S827 experiments is the influence of transition on the lift curve. Figure 1.8 plots lift and drag coefficients for the S827 airfoil when the transition location is fixed, illustrating that with the transition location fixed there is no longer a drop in lift for angles of attack around 5° to 7°.

14

The NREL experiments on the S809 and S827 illustrate the current capabilities for experimental generation of airfoil performance tables. In addition, the S827 experiments highlight the importance of laminar to turbulent transition for wind turbine airfoils by showing significant differences in performance depending on if the boundary layer is tripped to produce a fixed transition location.

1.2.1.2 Wind Turbines

NREL has performed several experiments on full wind turbines. The NREL Combined Experiment Phase II [11] focused on utilizing an instrumented wind turbine using blades based on the S809 airfoil, whose performance characteristics are well documented. The NREL Phase II experiment produced data on aerodynamic coefficients, unsteady aerodynamic data, flow-visualization, and blade loads. The NREL Unsteady Aerodynamics Experiment Phase VI carried out experimental measurements on a 10 m diameter turbine for a large range of operating conditions. The data gathered during the NREL Phase VI included aerodynamic coefficients, pressure data, blade loading, and flow visualization [10].

The NREL Phase II experiment conducted measurements to evaluate the wind turbine at a range of operating wind conditions. The results were compared to values predicted based on the S809 airfoil performance characteristics. Figure 1.9 compares the normal force coefficient at the $80\%(r/R)$ spanwise location for the NREL Phase II experiment to the normal force coefficient predicted based on the S809 airfoil characteristics. Comparing the predicted normal force coefficient to the measured
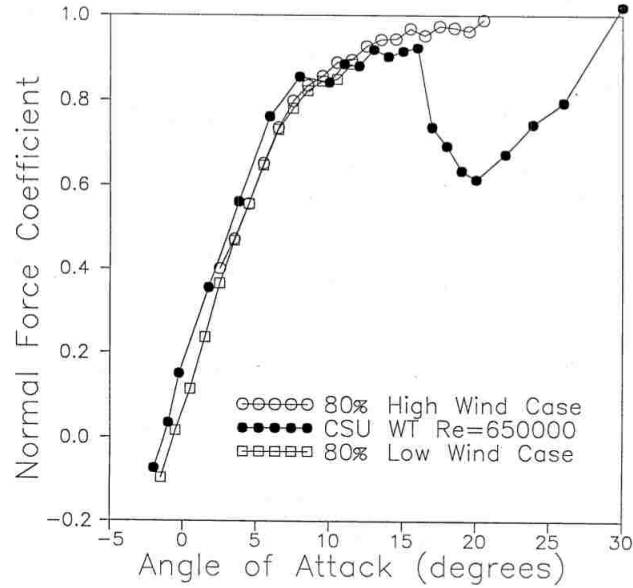
Figure 1.9 – Comparison of normal force coefficient for predictions based on the S809

performance values to the values determined experimentally using the

NREL Phase II wind turbine (Reproduced from Ref. [11])

coefficient revealed that at low angles of attack the predicted values matched the

experimental results well [11]. However, at higher angles of attack, the normal force

coefficient remained high while the predicted value dropped off significantly, which

is shown in Fig. 1.9 for the high wind case. This trend indicated that stall onset

was delayed because of rotational effects, Dumitrescu and Cardos [21] have since

observed that the primary cause of the stall delay is the Coriolis forces affecting flow

in the boundary layer. In addition to stall delay, the NREL Phase II experiment

found that there were non-zero pressure gradients in separated flow regions on the

inboard region of the blade that did not occur in the airfoil wind tunnel testing.

Both these pressure gradients and the stall delay that occurs for the wind turbine

point to the importance of including the effects of spanwise flow when capturing

16
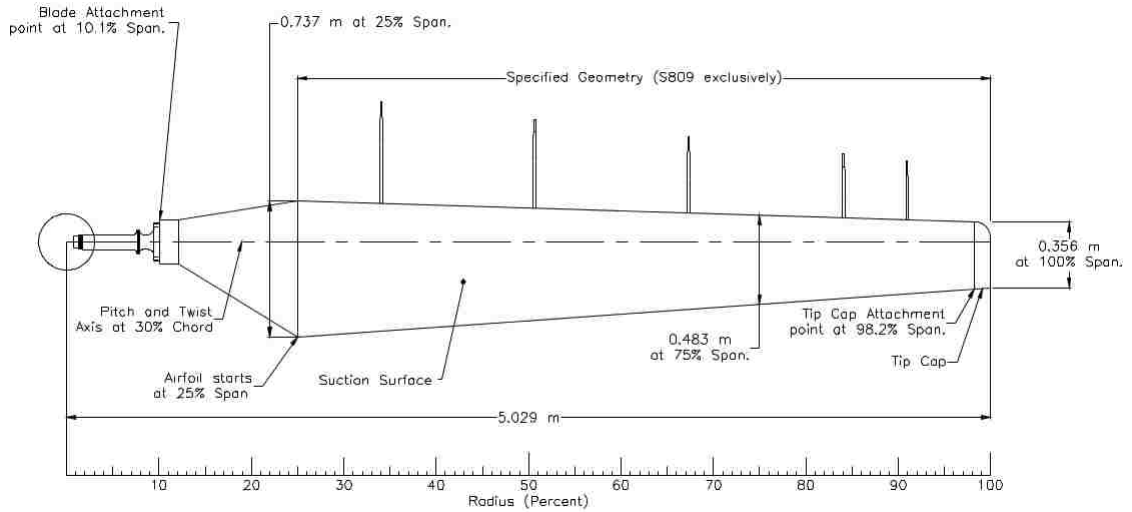
Figure 1.10 – NREL Phase VI wind turbine blade (Reproduced from Ref. [10])

wind turbine performance.

The NREL Phase VI experiments utilized a two bladed wind turbine with a 10.06 m diameter, rotational speed of 72 RPM, and the S809 airfoil [10]. The wind turbine blade dimensions are shown in Fig. 1.10. The NREL Phase VI experiment provided a wide range of data, illustrated by the test matrix in Fig. 1.11. The upwind baseline sequence, which has zero pitch angle and zero yaw angle, is of particular interest as it offers a convenient data set for evaluating CFD solvers. Flow separation occurs on the upper blade of the surface in this test sequence for wind speeds of greater than 10 m/s [22]. The presence of stall portions on the blade is useful for evaluating the predictive power of a CFD solver in capturing transitional flow phenomenon, such as incipient separation. The NREL Phase VI experiment provides a useful source of data for validating computational results under a wide range of conditions.

17

Ordinal Number	Test Sequence	Upwind/ Downwind	Rigid/ Teetered	Cone Angle (deg)	Yaw Angle (deg)	Slow Yaw Sweep	Blade Tip Pitch (deg)	Parked/ Rotating	RPM	Blade Press.	Probe Press.	Blade Tip	Day	NASA Run Number
B	Downwind Baseline (F)	Downwind	Teetered	3.4	Locked		3.0	Rotating	72.0	X	X	Baseline	1-4	11-14
C	Downwind Low Pitch (F)	Downwind	Teetered	3.4	Locked		0.0	Rotating	72.0	X	X	Baseline	1-4	11-14
D	Downwind High Pitch (F)	Downwind	Teetered	3.4	Locked		6.0	Rotating	72.0	X	X	Baseline	1-4	11-14
E	Yaw Releases (P)	Downwind	Rigid	3.4	Locked / Free		3.0	Rotating	72.0	X	X	Baseline	5	15, 16
F	Downwind High Cone (F)	Downwind	Rigid	18.0	Locked		3.0	Rotating	72.0	X	X	Baseline	6	17
G	Upwind Teetered (F)	Upwind	Teetered	0.0	Locked		3.0	Rotating	72.0	X	X	Baseline	8-9	34, 38
H	Upwind Baseline (F)	Upwind	Rigid	0.0	Locked	X	3.0	Rotating	72.0	X	X	Baseline	9,11,12,15	39, 41-43, 50
I	Upwind Low Pitch (F)	Upwind	Rigid	0.0	Locked	X	0.0	Rotating	72.0	X	X	Baseline	9,11,12	39, 41-43
J	Upwind High Pitch (F)	Upwind	Rigid	0.0	Locked	X	6.0	Rotating	72.0	X	X	Baseline	9,11,12	39, 41-43
K	Step AOA, Probes (P)	Upwind	Rigid	0.0	Locked at 0		Step & ramp	Rotating	72.0	X	X	Baseline	15	50
L	Step AOA, Parked (P)	Upwind	Rigid	0.0	Locked at 0		Step & ramp	Parked	0.0	X	X	Baseline	13	48
M	Transition Fixed (P)	Upwind	Rigid	0.0	Locked	X	3.0	Rotating	72.0	X		Baseline	16	52
N	Sin AOA, Rotating (P)	Upwind	Rigid	0.0	Locked at 0		Sinusoidal	Rotating	72.0	X	X	Baseline	14,15	49, 50
O	Sin AOA, Parked (P)	Upwind	Rigid	0.0	Locked at 0		Sinusoidal	Parked	0.0	X	X	Baseline	13	44-47
P	Wake Flow Vis. Upwind (P)	Upwind	Rigid	0.0	Locked		3.0, 12.0	Rotating	72.0			Visualize	10,11	40, 41
Q	Dynamic Inflow (P)	Upwind	Rigid	0.0	Locked at 0		Step	Rotating	72.0	X	X	Baseline	15	50
R	Step AOA, No Probes (P)	Upwind	Rigid	0.0	Locked at 0		Step & ramp	Rotating	72.0	X		Baseline	16	52
S	Upwind, No Probes (F)	Upwind	Rigid	0.0	Locked	X	3.0	Rotating	72.0	X		Baseline	16,18	52, 54
T	Upwind, 2 deg Pitch (F)	Upwind	Rigid	0.0	Locked at 0		2.0	Rotating	72.0	X		Baseline	16,18	52, 54
U	Upwind, 4 deg Pitch (F)	Upwind	Rigid	0.0	Locked at 0		4.0	Rotating	72.0	X		Baseline	16,18	52, 54
V	Tip Plate (F)	Upwind	Rigid	0.0	Locked at 0		3.0	Rotating	72.0	X		Plate	18	54
W	Extended Blade (F)	Upwind	Rigid	0.0	Locked at 0		3.0	Rotating	72.0	X		Extended	18	54
X	Elevated RPM (F)	Upwind	Rigid	0.0	Locked at 0		3.0	Rotating	90.0	X		Baseline	19	55
3	Tower Wake Measure (P)	Downwind	Rigid	3.4	Locked		53-79	Parked	0.0	X	X	Baseline	6	18
4	Static Press. Cal (P)	Downwind	Teetered	3.4	Locked at 0		3.0	Rotating	72.0	X	X	Baseline	4	14
5	Sweep Wind Speed (F,P)	Upwind	Rigid	0.0	Locked		3.0, 6.0	Rotating	72.0	X	Both	Baseline	11,19	43, 55
6	Shroud Wake Measure (P)	Downwind	Rigid	3.4	Locked		61-74	Parked	0.0	X	X	Baseline	7	19
7	Shroud Operating (P)	Downwind	Rigid	3.4	Locked		3.0	Rotating	72.0	X	X	Baseline	7	20
8	Downwind Sonics (F,P)	Upwind	Rigid	0.0	Locked		3.0	Rotating	72.0	X		Baseline	17	53
9	Sonic Validation (P)	Upwind	Rigid	0.0	Locked		3.0	Rotating	72.0			Baseline	17	53

(F) - Test conditions representative of field operation

(P) - Test conditions designed to explore specific flow physics phenomena

Figure 1.11 – NREL Phase VI test matrix, wind speed is varied within each test sequence (Reproduced from Ref. [10])

18

1.2.2 Computational Studies

Previous work on computational simulations of wind turbines and airfoils is presented in this section. The application of simplified turbine modeling tools is discussed. Background on utilizing CFD to generate two-dimensional wind turbine performance characteristics is provided. Next, studies on simulating full wind turbines using CFD are discussed. Finally, background on the implementation of GPU based hardware acceleration is presented.

1.2.2.1 Wind Turbine Modeling

Aeroelastic codes utilizing simplified aerodynamic models are useful wind turbine design tools. To evaluate the uncertainty in wind turbine models, Simms et al. [23] performed a blind comparison of experimental and computational results. Nineteen different modeling tools were used to model a subset of the operating conditions investigated by the NREL Unsteady Aerodynamics Experiment Phase VI [23]. The wind turbine modeling tools ranged from blade element momentum models to full three dimensional Navier–Stokes simulations. Wind tunnel and experimental results were not given to the researchers before the blind comparison. The results of the blind comparison showed significant differences in the predicted performance between the different models, even at lower wind speeds. The results from various codes for wind speeds ranging from $5\,\mathrm{m/s}$ to $25\,\mathrm{m/s}$ are shown in Fig. 1.12, with the experimental data represented as the bold line. Figure 1.13 shows the same data as Fig. 1.12 but focuses on the aeroelastic codes, illustrating that at higher wind
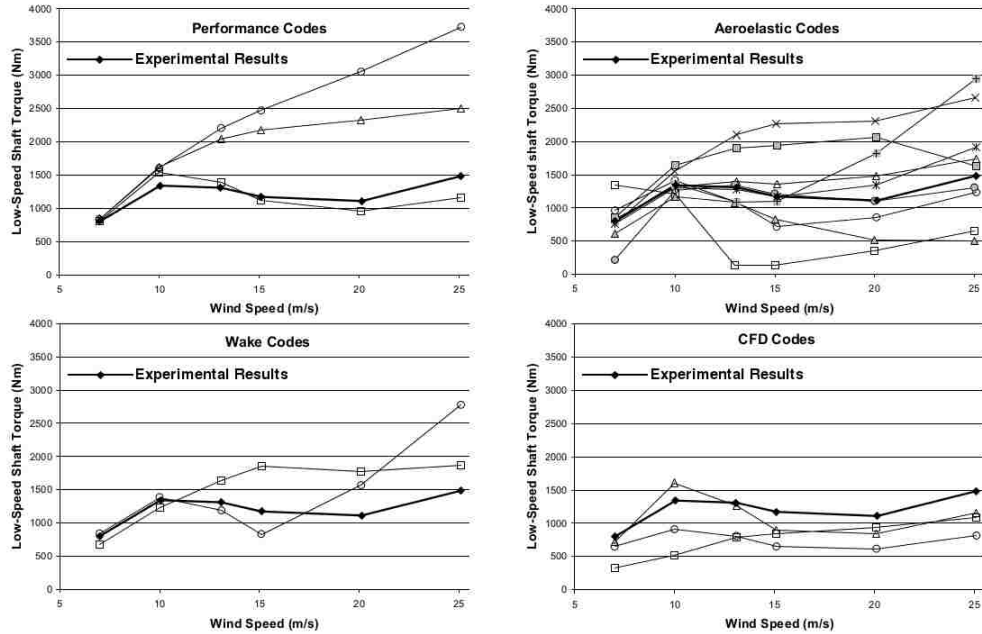
Figure 1.12 – A comparison of predicted shaft torque for different codes used to evaluate the NREL Phase VI turbine, the experimental results are shown with the bold lines and all the predictions are anonymized (Reproduced from Ref. [23])

speeds where blade stall is expected to occur, the spread of predicted shaft torque between the various aeroelastic codes increases, ranging from 30% to 200% of the experimental results. The wide range of predicted values highlights the difficulties of modeling aerodynamic performance under stalled conditions.

Duque et al. [24] found that CAMRAD II [12, 13], which utilizes a lifting-line model for aerodynamics, overpredicted aerodynamic loads on the blade even after a stall delay model was included. Figure 1.14 shows the variation of power against wind speed as measured by the NREL experiments and predicted by OVERFLOW-D and CAMRAD-II. CAMRAD II did not capture the stalled rotor performance
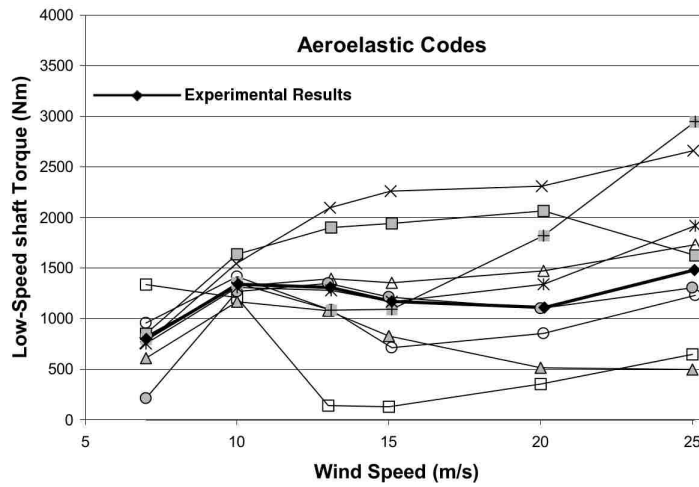
Figure 1.13 – A comparison of predicted shaft torque for different aeroelastic analysis codes used to evaluate the NREL Phase VI turbine (Reproduced from Ref. [23])
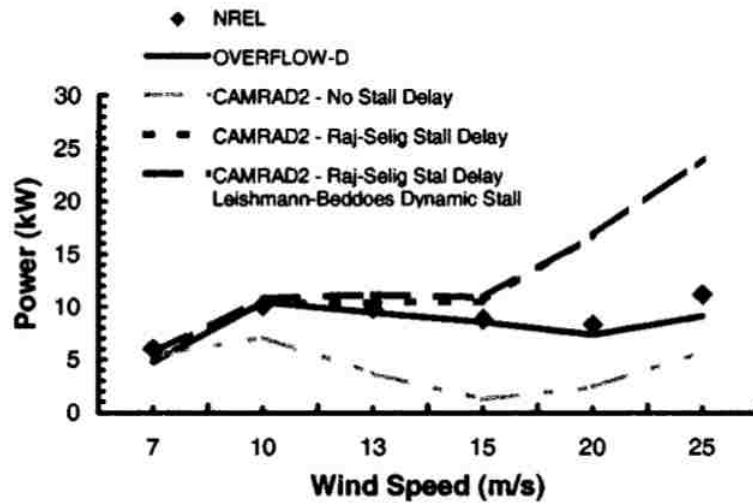
Figure 1.14 – Comparison of power predictions by CAMRAD II and OVERFLOW-D to measured power for the NREL phase VI rotor (Reproduced from Ref. [24])
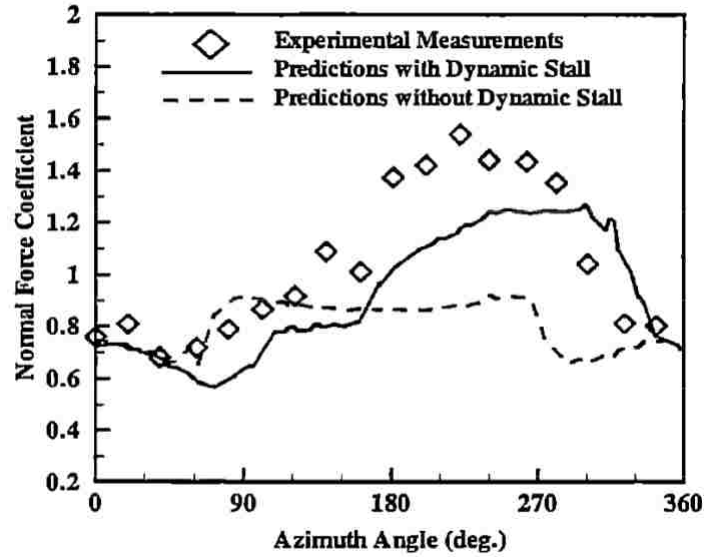
Figure 1.15 – Comparison of predicted and measured normal force coefficient distribution for the NREL Combined Experiment wind turbine at 63% span (Reproduced from Ref. [25])

at higher wind speeds, as shown in Fig. 1.14. Leclerc and Masson [25] performed Navier–Stokes simulations on the NREL Combined Experiment [11] wind turbine where the wind turbine was modeled as an actuator disk using a blade element momentum model. Figure 1.15 compares the normal force coefficient predicted by Leclerc and Masson [25] to the measured normal force coefficient distribution for the NREL Combined Experiment wind turbine at 63% of span. Simulations were performed both with and without a dynamic stall model, and Fig. 1.15 shows that the dynamic stall model improved predictions of the normal force coefficient. However, there were still significant differences between the predicted normal force coefficient and the experimental data over the blade azimuthal range. The large discrepancies seen when modeling stalled conditions highlights the need to improve

22

performance predictions in the stalled regime by either improving stall models or utilizing airfoil data to improve predictions of stalled performance.

1.2.2.2 Wind Turbine Airfoil Simulations

Two-dimensional simulations of wind turbine airfoils provides an avenue for improving the predictive capability of comprehensive analysis codes. However, one of the limitations of using CFD is the ability of current models to accurately capture the effects of stall. The adverse pressure gradient (APG) correction [26] is a modification to the turbulence model that relies on empirical correlations between the ratio of the magnitudes of local shear stress to wall shear stress and the presence of adverse pressure gradients to predict earlier separation on airfoils. Medida et al. [26] showed that the APG correction reduces the overprediction of lift typically seen in simulations of airfoils in the stall regime. The lift coefficient predictions by the several versions of the SA model are compared to experimental results in Fig. 1.16, which shows that the APG correction reduces lift overprediction in the stall regime.

Another significant enhancement to the transition modeling is the addition of transition modeling to reduce the over-prediction of drag at low angles of attack and capture laminar separation bubbles, which is of particular importance in wind turbine applications. It was shown by Medida et al. [27] that including transition modeling in simulations of the S809 wind turbine airfoil significantly improved drag prediction at low angles of attack. Figure 1.17 compares drag predictions by the
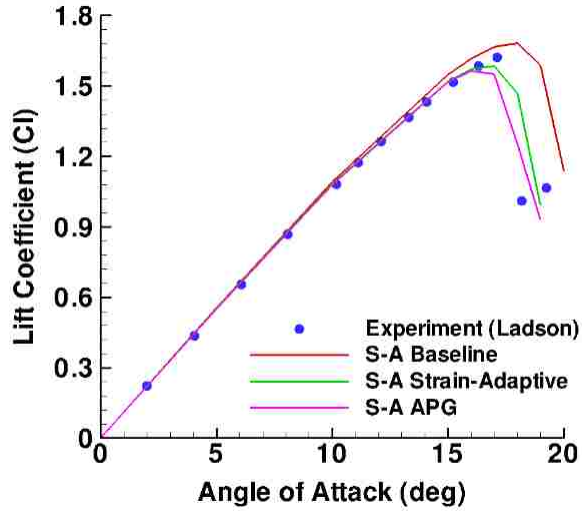
Figure 1.16 – Comparison of predicted lift with and without the adverse pressure gradient (APG) correction to experimental values for a NACA 0012 airfoil, $Re = 6 \times 10^6$, $M = 0.15$ (Reproduced from Ref. [26])
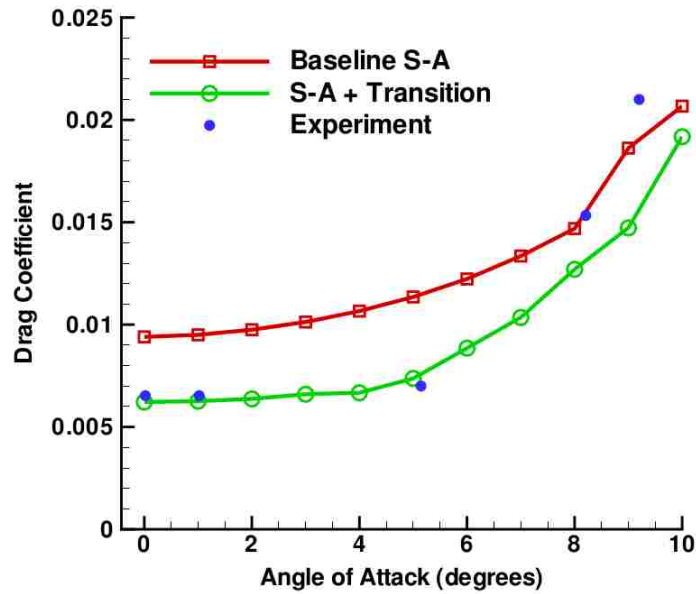
Figure 1.17 – Comparison of predicted drag with and without transition modeling to experimental values for an S809 airfoil, $Re = 2 \times 10^6$ (Reproduced from Ref. [27])

24
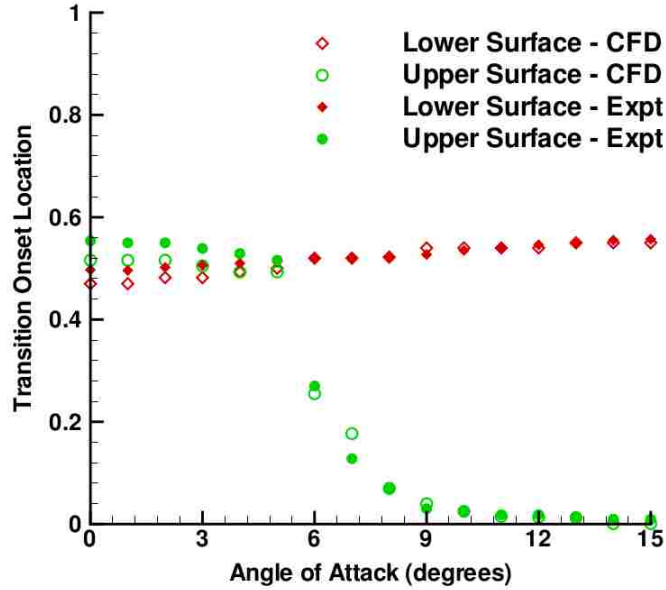
Figure 1.18 – Comparison of predicted transition onset location to experimental values for an S809 airfoil, $Re = 2 \times 10^6$ (Reproduced from Ref. [27])

baseline SA model and the SA model with transition to experimental values, illustrating the improvements in drag prediction due to transition modeling. In addition, the predicted transition location was compared to experimentally determined values for a range of angles of attack, shown in Fig. 1.18.

Previous studies of two-dimensional airfoils using turbulence model improvements including the APG correction and transition modeling show distinct improvements in the predicted performance values for the S809 airfoil. Though the simulations still show discrepancies for certain freestream conditions, such as high angle of attack, the range of regimes where the CFD simulations accurately predict experimental performance is increased compared to the baseline SA model.

1.2.2.3 Three-dimensional Wind Turbine Rotor Simulations

Full three-dimensional Navier–Stokes simulations can be used to more accurately predict wind turbine performance by capturing aerodynamic effects that may not be captured in lower order fidelity simulations, such as a free-vortex method. In a comparison of CAMRAD II and OVERFLOW-D, Duque et al. [24] found that OVERFLOW-D (a full three-dimensional Navier–Stokes solver) predicted the power produced by the NREL Phase VI wind turbine significantly better than the lifting line model utilized in CAMRAD II, as shown previously in Fig. 1.14. However, OVERFLOW-D still showed some discrepancies in the predicted aerodynamic loads when compared to the experiments. The radial normal force coefficient predictions of CAMRAD II and OVERFLOW-D are compared in Fig. 1.19, which shows larger discrepancies occurring at wind speeds of 15 m/s and higher when compared to the experimental results. In particular, OVERFLOW-D had trouble predicting the stall delay present in the 13 m/s and 15 m/s wind speed cases.

Xu et al. [28] investigated the NREL Phase VI wind turbine using both the full Navier–Stokes simulations and a hybrid method combining a Navier–Stokes solver near the blade and potential flow for the background. Figure 1.20 shows the normal force coefficient at the 30% r/R spanwise station, similar to the results obtained by Duque et al. [24], the normal force coefficient near the root deviated by as much as 50% from the experimental data. The authors mention that one possible source for the error is an inability to properly capture the massively separated flow at the root when using the one equation Spalart-Allmaras turbulence model.
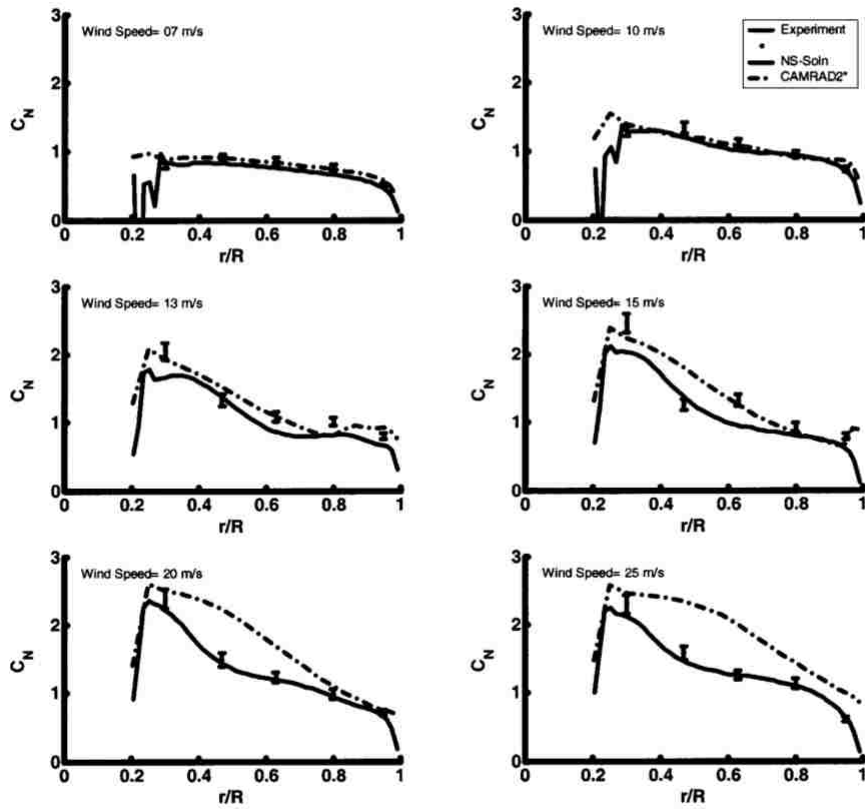
Figure 1.19 – Comparison of radial normal force coefficient predictions by CAM-
RAD II and OVERFLOW-D to measured radial normal force coeffi-
cient for the NREL phase VI rotor at multiple wind speeds (Repro-
duced from Ref. [24])

27
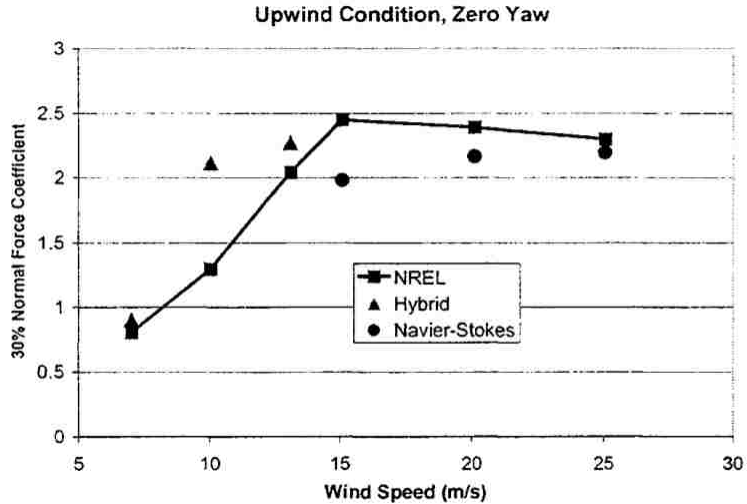
Figure 1.20 – Comparison of predicted and measured normal force coefficient at

30%R for the NREL phase VI rotor (Reproduced from Ref. [28])

Following the work by Xu et al. [28], Benjanirat et al. [29] also simulated the NREL Phase VI wind turbine, focusing on the effect of turbulence modeling on the predicted performance and aerodynamic loads. Four turbulence models were investigated, the Baldwin-Lomax model, the Spalart-Allmaras model, the $k - \epsilon$ model without near wall modeling, and the $k - \epsilon$ model with near wall modeling. Figure 1.21 compares the low speed shaft torque predicted using a variety of turbulence models to the experimental values for the NREL Phase VI, showing that one of the turbulence models investigated, the $k - \epsilon$ model with wall treatment, outperforms the other turbulence models at low wind speeds by correctly showing an initial peak in torque. The $k - \epsilon$ model with wall treatment includes some crude transition modeling by altering how the viscous sublayer region is modeled [30]. Furthermore, the calculations of the kinetic energy and dissipation were modified to use experimentally determined relations for the viscous sublayer. The improved

28
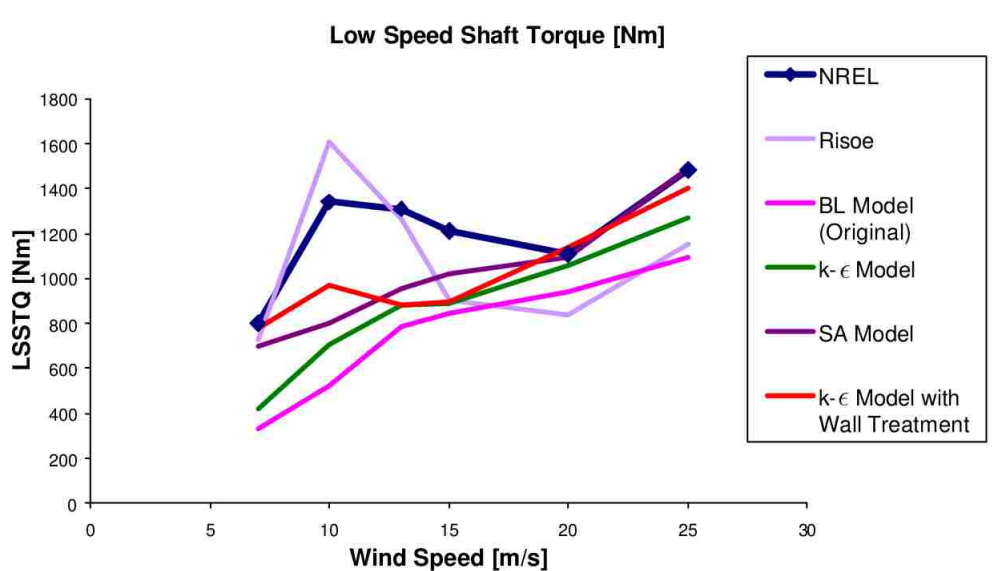
Figure 1.21 – Comparison of predicted and measured low speed shaft torque (LSSTQ) for the NREL phase VI rotor (Reproduced from Ref. [29])

performance predictions of the $k - \epsilon$ model with wall treatment points to transition modeling as an area of interest for wind turbine simulations.

1.2.2.4 GPU Based Hardware Acceleration

Utilizing GPUs for hardware acceleration can significantly reduce the amount of time and computational resources required to complete CFD simulations. Thomas [31] implemented a three-dimensional Navier–Stokes solver that utilizes GPU acceleration. The work highlights the necessity of choosing algorithms that are both accurate and can be parallelized, to fully utilize GPU resources, an area of particular concern for implicit time stepping methods. Thomas found that as long as the number of independent lines being solved by the implicit method is larger than the number of cores on the GPU, the line implicit methods can fully utilize GPU resources.

29

GPU Type	Cores	Memory (MB)	Clock (MHz)	Memory Bandwidth (Gb/s)
GTX640	384	2078	797	28.5
GTX480	480	1536	700	177.4
GTX580	512	1536	772	192.4
Titan	2688	6144	837	288

Figure 1.22 – Comparison of different GPU platforms used by Thomas to test the

GPU accelerated Navier–Stokes solver (Reproduced from Ref. [31])
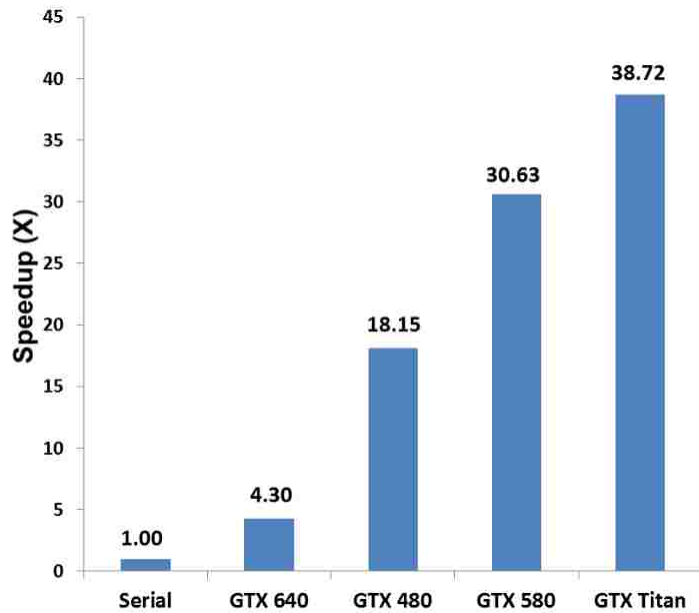
Figure 1.23 – Comparison of serial computation speed (using a 3.1 GHz Intel Core

i5 CPU) to computation speed for different GPU platforms for the

Onera M6 test case (Reproduced from Ref. [31])

Several validations cases were performed to evaluate the computational speedup achieved through GPU acceleration. The flow over the Onera M6 wing was used as one of the benchmark cases and the simulations were performed using different GPU cards. Figure 1.22 compares the memory bandwidth and computing power for different types of GPUs used to test the GPU accelerated flow solver. The highest performing card, the GTX Titan, has approximately seven times the computing power and ten times the memory bandwidth of the lowest performing card, the GTX 640. Comparing the theoretical speedup of increasing the GPU computing power to the actual speedup is useful for evaluating how well the performance gains scale with increasing GPU power. Figure 1.23 shows the computational speedup achieved using different GPU cards when compared to a single core CPU. In this study, a 3.1 GHz Intel Core i5 CPU was used as a baseline for comparison. The accelerated solver was nearly forty times faster in double precision than the serial code when the GPU with the highest computing power was used, i.e., the GTX Titan. The differences in the speedup between the other GPU cards are a result of their hardware specifications and the number of parallel cores it contains.

1.2.3   Sandia 100 m Blade

Wind turbine blade sizes have consistently grown over the years to provide more power per turbine. Currently prototype turbines with rotors approximately 80 m in radius are being tested [32]. The work by Sandia National Laboratories seeks to develop a 100 m blade design to serve as a baseline for future blade de-
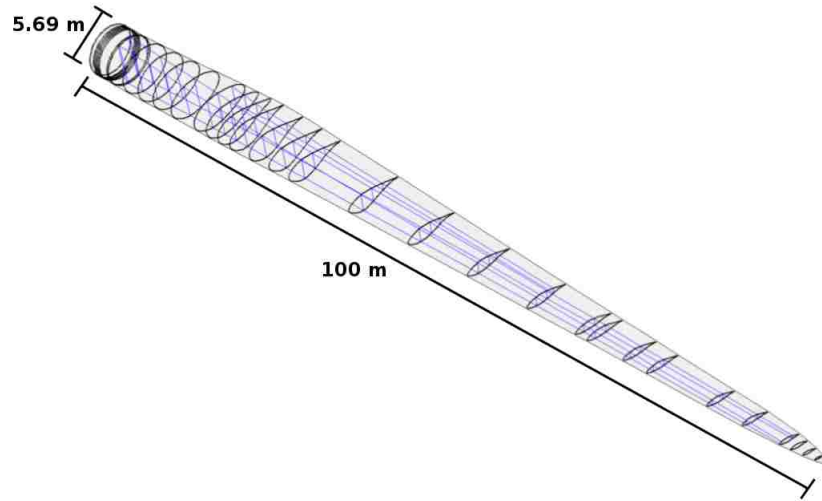
Figure 1.24 – Sandia 100 m blade geometry (Reproduced from Ref. [7])

velopment [7]. Scaling laws are used to scale up a 64.5 m blade for 5 MW turbines developed by DOWEC [33] to the 100 m blade intended for 13.2 MW turbines. Scaling laws are a method of predicting how the blade length affects design trends such as natural frequencies and bending moments by extrapolating existing wind turbine properties to larger turbines [7]. The resulting blade geometry is shown in Fig. 1.24. The chord at the tip of the blade is reduced from the scaled up DOWEC value to 0.1 m, creating a near point at the blade tip. The blade airfoil, chord, and twist properties are shown in Fig. 1.25. No aerodynamic properties were considered during the scaling of the blade because the design of the baseline 100 m blade is focused on the composite layup and structural properties [7].

1.2.4 Leading Edge Tubercles

Leading edge tubercles, like those shown in Fig. 1.26, are a possible blade geometry modification that could provide improved aerodynamic performance under

Station Number	Blade Fraction	Chord (m)	Twist (deg)	Pitch Axis (Fraction)	Airfoil Description
1	0.000	5.694	13.308	0.500	Cylinder
2	0.005	5.694	13.308	0.500	Cylinder
3	0.007	5.694	13.308	0.500	Transition (99.25%)
4	0.009	5.694	13.308	0.500	Transition (98.5%)
5	0.011	5.694	13.308	0.500	Transition (97.75%)
6	0.013	5.694	13.308	0.500	Ellipse (97%)
7	0.024	5.792	13.308	0.499	Ellipse (93.1%)
8	0.026	5.811	13.308	0.498	Ellipse (92.5%)
9	0.047	6.058	13.308	0.483	Transition (84%)
10	0.068	6.304	13.308	0.468	Transition (76%)
11	0.089	6.551	13.308	0.453	Transition (68%)
12	0.114	6.835	13.308	0.435	Transition (60%)
13	0.146	7.215	13.308	0.410	Transition (51%)
14	0.163	7.404	13.177	0.400	Transition (47%)
15	0.179	7.552	13.046	0.390	Transition (43.5%)
16	0.195	7.628	12.915	0.380	DU99-W-405
17	0.222	7.585	12.133	0.378	DU99-W-405 (38%)
18	0.249	7.488	11.350	0.377	DU99-W-350 (36%)
19	0.276	7.347	10.568	0.375	DU99-W-350 (34%)
20	0.358	6.923	9.166	0.375	DU97-W-300
21	0.439	6.429	7.688	0.375	DU91-W2-250 (26%)
22	0.520	5.915	6.180	0.375	DU93-W-210 (23%)
23	0.602	5.417	4.743	0.375	DU93-W-210
24	0.667	5.019	3.633	0.375	NACA-64-618 (19%)
25	0.683	4.920	3.383	0.375	NACA-64-618 (18.5%)
26	0.732	4.621	2.735	0.375	NACA-64-618
27	0.764	4.422	2.348	0.375	NACA-64-618
28	0.846	3.925	1.380	0.375	NACA-64-618
29	0.894	3.619	0.799	0.375	NACA-64-618
30	0.943	2.824	0.280	0.375	NACA-64-618
31	0.957	2.375	0.210	0.375	NACA-64-618
32	0.972	1.836	0.140	0.375	NACA-64-618
33	0.986	1.208	0.070	0.375	NACA-64-618
34	1.000	0.100	0.000	0.375	NACA-64-618

Figure 1.25 – Sandia 100 m blade airfoil and chord properties, thickness to chord ratio is in parentheses for transition and modified airfoil descriptions (Reproduced from Ref. [7])

Figure 1.26 – Leading edge tubercles on a humpback whale flipper (Reproduced from Ref. [36])

specific flow conditions. Based on the position and spacing of the leading edge tubercles on humpback whale fins, Fish and Battle [34] noted that the tubercles could be functional adaptations that improve the hydrodynamic performance of these fins. To evaluate the possibility of wing performance enhancements provided by leading edge tubercles, Watts and Fish [35] utilized an inviscid three-dimensional panel method to represent the aerodynamic effects of the wing and the associated tubercles. At low angles of attack, the tubercles had nearly zero effect on the predicted lift and drag. However, at an angle of attack of $10°$ performance improvements were observed with a 4.8% increase in lift and 10.9% reduction in induced drag.

The primary advantage of leading edge tubercles is in the reduction of separation occurring at high angles of attack. Modern utility scale wind turbines are

typically pitch regulated, as a result the blades operate with the majority of the blade in the attached flow regime when they are operating under steady flow conditions. However, in situations where wind gusts or other sources of unsteady flow are present, it is possible that portions of the blade could experience stall. The addition of leading edge tubercles has the possibility to improve wind turbine performance in unsteady conditions with minimal performance cost during normal operating conditions.

1.3   Thesis Contributions

The contributions of this research include the following:

1. Evaluate the use of existing transition and turbulence modeling improvements for wind turbine applications using two dimensional wind turbine airfoil simulations.

2. Perform three dimensional simulations of the Sandia 100 m reference blade to evaluate the effects of improved transition and turbulence modeling on the aerodynamic performance of large wind turbine blades.

3. Quantify the performance effects of leading tubercles at normal operating conditions.

1.4   Scope and Organization of Thesis

This thesis is focused on predicting performance characteristics for wind turbine airfoils and blades. The rest of the thesis is organized as follows.

The second chapter describes computational methodology utilized for simulations in this work. The various numerical algorithms associated with both Over-TURNS and the GPU-RANS solver are described.

The third chapter focuses on the two dimensional wind turbine airfoil simulation results. The improvements gained by improved transition and turbulence modeling are detailed using experimental results as a reference.

The fourth chapter evaluates the three dimensional wind turbine blade simulation results. The predicted performance for the Sandia $100\,\mathrm{m}$ blade is compared to other computational studies and the effects of transition modeling are explored. In addition, the performance consequences of leading edge tubercles are investigated.

The fifth chapter summarizes conclusions from this work and also provides recommendations for future work.

Chapter 2:   Methodology

This chapter presents the numerical methodology used to study the airfoil and wind turbine aerodynamics. The simulations were performed using two different structured Reynolds Averaged Navier–Stokes (RANS) solvers:

1. an overset structured RANS solver called OverTURNS (Overset Transonic Unsteady Rotor Navier–Stokes)

2. a GPU-based RANS solver

Unless otherwise noted, the finite volume algorithms used in OverTURNS and the GPU-RANS solver are the same.

The Navier–Stokes equations form a system of partial differential equations that govern unsteady, compressible fluid flow in the Eulerian frame of reference. To obtain the form of the equations used in the solvers several transformations are applied to the three-dimensional Cartesian form of the Navier–Stokes equations. The transformations are: non-dimensionalization the equations, Reynolds averaging, and the curvilinear coordinate transformation. Non-dimensionalization helps reduce numerical inaccuracies, Reynolds-averaging is required to avoid modeling all turbulence scales, and the curvilinear coordinate transform simplifies the application of numerical algorithms. The transformed equations are then discretized in space

and time to form a system of coupled algebraic equations that are solved numerically to obtain various properties of the flow.

2.1 Governing Equations

The Navier–Stokes equations are used to model fluid motion. The three-dimensional, unsteady Navier–Stokes equations consist of time dependent equations for the conservation of mass, momentum, and energy. It is assumed the the fluid being modelled is a continuum. The system of equations is expressed in Cartesian coordinates as,

$$\frac{\partial \mathbf{Q}}{\partial t} + \frac{\partial \mathbf{F}_i}{\partial x} + \frac{\partial \mathbf{G}_i}{\partial y} + \frac{\partial \mathbf{H}_i}{\partial z} = \frac{\partial \mathbf{F}_v}{\partial x} + \frac{\partial \mathbf{G}_v}{\partial y} + \frac{\partial \mathbf{H}_v}{\partial z} + \mathbf{S} \tag{2.1}$$

where $\mathbf{Q}$ is the vector of conserved variables, $\mathbf{F}_i$, $\mathbf{G}_i$, and $\mathbf{H}_i$ are the inviscid flux vectors, and $\mathbf{F}_v$, $\mathbf{G}_v$, and $\mathbf{H}_v$ are the viscous flux vectors. $\mathbf{S}$ represents the vector of body forces and/or accounts for a change in reference frame (e.g. from the inertial frame of reference to the rotational frame of reference). The vector of conserved variables, $\mathbf{Q}$, is given by,

$$\mathbf{Q} = \begin{Bmatrix} \rho \\ \rho u \\ \rho v \\ \rho w \\ E \end{Bmatrix} \tag{2.2}$$

where the density is given by ρ, the Cartesian velocity components are u, v, and w, and E is the total energy per unit volume given by,

$$E = \rho \left[e + \frac{1}{2}(u^2 + v^2 + w^2) \right] \tag{2.3}$$

where e is the internal energy per unit mass.

The inviscid flux vectors $(\mathbf{F}_i, \mathbf{G}_i, \mathbf{H}_i)$ are given by,

$$\mathbf{F}_i = \left\{ \begin{array}{c} \rho u \\ \rho u^2 + p \\ \rho uv \\ \rho uw \\ u(E + p) \end{array} \right\} \tag{2.4}$$

$$\mathbf{G}_i = \left\{ \begin{array}{c} \rho v \\ \rho vu \\ \rho v^2 + p \\ \rho vw \\ v(E + p) \end{array} \right\} \tag{2.5}$$

$$\mathbf{H}_i = \left\{ \begin{array}{c} \rho w \\ \rho wu \\ \rho wv \\ \rho w^2 + p \\ w(E + p) \end{array} \right\} \tag{2.6}$$

The viscous flux vectors $(\mathbf{F}_v, \mathbf{G}_v, \mathbf{H}_v)$ are given by,

$$\mathbf{F}_v = \left\{ \begin{array}{c} 0 \\ \tau_{xx} \\ \tau_{yx} \\ \tau_{zx} \\ u\tau_{xx} + v\tau_{xy} + w\tau_{xz} - q_x \end{array} \right\} \tag{2.7}$$

$$\mathbf{G}_v = \left\{ \begin{array}{c} 0 \\ \tau_{xy} \\ \tau_{yy} \\ \tau_{zy} \\ u\tau_{yx} + v\tau_{yy} + w\tau_{yz} - q_y \end{array} \right\} \tag{2.8}$$

$$\mathbf{H}_v = \left\{ \begin{array}{c} 0 \\ \tau_{xz} \\ \tau_{yz} \\ \tau_{zz} \\ u\tau_{zx} + v\tau_{zy} + w\tau_{zz} - q_z \end{array} \right\} \tag{2.9}$$

where q_x, q_y, and q_z are the thermal conduction terms expressed as a function of the temperature (T) and the coefficient of thermal conductivity (k) as given by,

$$q_i = -k\frac{\partial T}{\partial x_i} \tag{2.10}$$

The pressure, p, can be determined using the equation of state for a perfect gas, given by,

$$p = \rho RT \tag{2.11}$$

where R is the specific gas constant. All flows studied in this work assume air operating at standard temperature and pressure. Therefore the calorically perfect gas assumption is valid, which assumes air is an ideal gas with constant specific heats. The specific heats at constant volume (C_v) and at constant pressure (C_p) are given by,

$$C_v = \frac{R}{\gamma - 1}; \quad C_p = \frac{\gamma R}{\gamma - 1} \tag{2.12}$$

For a calorically perfect gas,

$$e = C_v T \tag{2.13}$$

Using the specific heats, Eq. (2.12), and the calorically perfect gas relation, (2.13), the equation of state can be written as,

$$p = (\gamma - 1)\rho e \tag{2.14}$$

Combining Eq. (2.3) and Eq. (2.14),

$$p = (\gamma - 1)\left[E - \frac{1}{2}\rho(u^2 + v^2 + w^2)\right] \tag{2.15}$$

where the value of the ratio of specific heats (γ) is 1.4 for air at standard temperature and pressure.

40

The viscous stress tensor for Newtonian fluids, τ_{ij}, formulated using Stokes' hypothesis is given by,

$$\tau_{ij} = \mu \left[\left(\frac{\partial u_i}{\partial x_j} + \frac{\partial u_i}{\partial x_j} \right) - \frac{2}{3} \frac{\partial u_k}{\partial x_k} \delta_{ij} \right] \tag{2.16}$$

The coefficient of molecular viscosity, μ, can be calculated using Sutherland's formula [37],

$$\mu = C_1 \frac{T^{\frac{3}{2}}}{T + C_2} \tag{2.17}$$

where $C_1 = 1.4 \times 10^{-6} \, \text{kg}/(\text{ms}\sqrt{\text{K}})$ and $C_2 = 110.4 \, \text{K}$ for air at standard temperature and pressure.

2.2 Non-Dimensional Form of the Navier–Stokes Equations

The Navier–Stokes equations are often solved in their non-dimensional form. One advantage of the non-dimensional form is that all flow variables are normalized to unity, which reduces the numerical inaccuracies that can result from numerical operations on values of significantly different order of magnitude. The non-dimensional variables used are given below (indicated by the * superscript) as,

$$x^* = \frac{x}{L}, \qquad y^* = \frac{y}{L}, \qquad z^* = \frac{z}{L}, \qquad t^* = \frac{ta_\infty}{L} \tag{2.18}$$

$$u^* = \frac{u}{a_\infty}, \qquad v^* = \frac{v}{a_\infty}, \qquad w^* = \frac{w}{a_\infty}, \qquad \mu^* = \frac{\mu}{a_\infty} \tag{2.19}$$

$$\rho^* = \frac{\rho}{\rho_\infty}, \qquad p^* = \frac{p}{\rho_\infty a_\infty^2}, \qquad T^* = \frac{T}{T_\infty} \tag{2.20}$$

where the reference length L is typically chosen as the chord length of the airfoil, a is the speed of sound, and a subscript ∞ indicates free-stream values. The resulting

non-dimensional parameters are given below,

$$\text{Reynolds number:} \qquad Re_\infty = \frac{\rho_\infty V_\infty L}{\mu_\infty} \qquad (2.21)$$

$$\text{Mach number:} \qquad M_\infty = \frac{V_\infty L}{a_\infty} \qquad (2.22)$$

$$\text{Prandtl number:} \qquad \frac{\mu C_p}{k} \qquad (2.23)$$

where V_∞ is the free-stream velocity magnitude, given by $\sqrt{u_\infty^2 + v_\infty^2 + w_\infty^2}$. Air at standard temperature and pressure has a Prandtl number of 0.72.

The non-dimensional form of the Navier–Stokes equations are identical to the dimensional form except for the viscous stress tensor and the heat conduction terms. The non-dimensional viscous stress tensor is given by Eq. (2.24) and the non-dimensional heat conduction terms are given by Eq. (2.25),

$$\tau_{ij} = \frac{\mu M_\infty}{Re_\infty} \mu \left[\left(\frac{\partial u_i}{\partial x_j} + \frac{\partial u_i}{\partial x_j} \right) - \frac{2}{3} \frac{\partial u_k}{\partial x_k} \delta_{ij} \right] \qquad (2.24)$$

$$q_j = -\frac{\mu M_\infty}{Re_\infty Pr(\gamma - 1)} \frac{\partial T}{\partial x_j} \qquad (2.25)$$

2.3 Reynolds-Averaged Navier–Stokes (RANS) Equations

In the case of inviscid or laminar flows there are no further assumptions that need to be made to solve the governing equations, Eq. (2.1). However, flows involving wind turbines are typically turbulent. One potential approach is to fully resolve the turbulence at all spatial and temporal scales using a Direct Numerical Simulation (DNS), but these simulations are prohibitively expensive with the current

computing resources, except for relatively simple, lower Reynolds number problems. Another approach that is significantly less computationally expensive is the use of RANS equations. The RANS equations decompose the dependent variables in the governing equations, Eq. (2.1), into the mean component and the fluctuating component. The resulting equations are then averaged over a period of time.

The mean (time-averaged) component of a variable f is defined as,

$$\bar{f} = \frac{1}{\Delta t} \int_{t_0}^{t_0+\Delta t} f\,dt \tag{2.26}$$

where t_0 is the current time and Δt is the timestep size. The time-average of the fluctuating component is zero. The following relations hold for any two fluctuating quantities f' and g',

$$\overline{\bar{f}g'} = 0, \qquad \overline{\bar{f}g} = \bar{f}\bar{g}, \qquad \overline{f+g} = \bar{f}+\bar{g} \tag{2.27}$$

$$\overline{f'f'} \neq 0 \qquad \overline{f'g'} \neq 0 \tag{2.28}$$

The dependent variables in the Navier–Stokes equations are written in terms of their mean and fluctuating components as,

$$u = \bar{u}+u', \quad v = \bar{v}+v', \quad w = \bar{w}+w', \quad \rho = \bar{\rho}+\rho', \quad p = \bar{p}+p', \quad T = \bar{T}+T' \tag{2.29}$$

The turbulence intensity (Tu) is defined as the ratio of the root-mean-square of the velocity fluctuations and the mean velocity,

$$Tu = \frac{U'}{\bar{U}} \tag{2.30}$$

$$U' = \sqrt{\frac{1}{3}[(u')^2 + (v')^2 + (w')^2]} \quad \text{and} \quad \bar{U} = \sqrt{(\bar{u})^2 + (\bar{v})^2 + (\bar{w})^2} \tag{2.31}$$

43

Substituting the decomposed variables from Eq. (2.29) into the Navier–Stokes equations given in Eq. (2.1) and time-averaging the equations results in the RANS equations. The resulting system of equations is identical to the Navier–Stokes equations, except for the addition of several terms that are functions of the turbulent fluctuating variables. The additional terms transport momentum through turbulent fluctuations, a behavior mirroring that of a viscous stress tensor. These terms are commonly referred to as the Reynolds stress tensor given by,

$$(\overline{\tau_{ij}})_{turb} = -\overline{\rho u_i' u_j'} \tag{2.32}$$

The Reynolds stress tensor adds six additional unknowns to the Reynolds-averaged momentum equations since it is a symmetric 3×3 matrix. To avoid adding additional independent variables the Reynolds stress tensor is represented using mean flow quantities. Turbulence models are used accomplish to represent the Reynolds stress tensor using mean flow quantities and achieve full closure for the RANS equations. Details of turbulence modeling are presented in Section 2.5.3.

2.4   Curvilinear Coordinate Transformation

The Cartesian form of the Navier–Stokes equations is applicable to any computational grid topology. However, the stencils for numerical spatial derivatives are typically based on uniform grid spacing and are not suitable for grids with non-uniform spacing, particularly in the presence of rapid mesh stretching. Because of this limitation it is often necessary to utilize a curvilinear coordinate transformation, Fig. 2.1 illustrates how the governing equations are mapped from the non-uniform

spaced body conforming domain (x,y,z) onto a computational domain (ξ,η,ζ) with equal grid spacing. Chain rule differentiation is applied to the Cartesian set of equations Eq. (2.1), resulting in,

$$\frac{\partial \tilde{\mathbf{Q}}}{\partial t} + \frac{\partial \tilde{\mathbf{F}}}{\partial \xi} + \frac{\partial \tilde{\mathbf{G}}}{\partial \eta} + \frac{\partial \tilde{\mathbf{H}}}{\partial \zeta} = \tilde{\mathbf{S}} \tag{2.33}$$

where

$$\tilde{\mathbf{Q}} = \frac{1}{J}\mathbf{Q}$$

$$\tilde{\mathbf{F}} = \frac{1}{J}[\xi_t\mathbf{Q} + \xi_x(\mathbf{F}_i - \mathbf{F}_v) + \xi_y(\mathbf{G}_i - \mathbf{G}_v) + \xi_z(\mathbf{H}_i - \mathbf{H}_v)]$$

$$\tilde{\mathbf{G}} = \frac{1}{J}[\eta_t\mathbf{Q} + \eta_x(\mathbf{F}_i - \mathbf{F}_v) + \eta_y(\mathbf{G}_i - \mathbf{G}_v) + \eta_z(\mathbf{H}_i - \mathbf{H}_v)] \tag{2.34}$$

$$\tilde{\mathbf{H}} = \frac{1}{J}[\zeta_t\mathbf{Q} + \zeta_x(\mathbf{F}_i - \mathbf{F}_v) + \zeta_y(\mathbf{G}_i - \mathbf{G}_v) + \zeta_z(\mathbf{H}_i - \mathbf{H}_v)]$$

$$\tilde{\mathbf{S}} = \frac{1}{J}\mathbf{S}$$

and J is the Jacobian of the coordinate transformation, which is the determinant of the 3×3 matrix,

$$\begin{bmatrix} \dfrac{\partial \xi}{\partial x} & \dfrac{\partial \xi}{\partial y} & \dfrac{\partial \xi}{\partial z} \\[2mm] \dfrac{\partial \eta}{\partial x} & \dfrac{\partial \eta}{\partial y} & \dfrac{\partial \eta}{\partial z} \\[2mm] \dfrac{\partial \zeta}{\partial x} & \dfrac{\partial \zeta}{\partial y} & \dfrac{\partial \zeta}{\partial z} \end{bmatrix} \tag{2.35}$$

2.5   Numerical Algorithms

The various algorithms used for discretizing the governing equations, turbulence modeling, and numerical boundary conditions are described in this section. A cell-averaged finite-volume technique is used to solve the curvilinear form of the RANS equations, (2.33). The control volume is a cell created around each grid
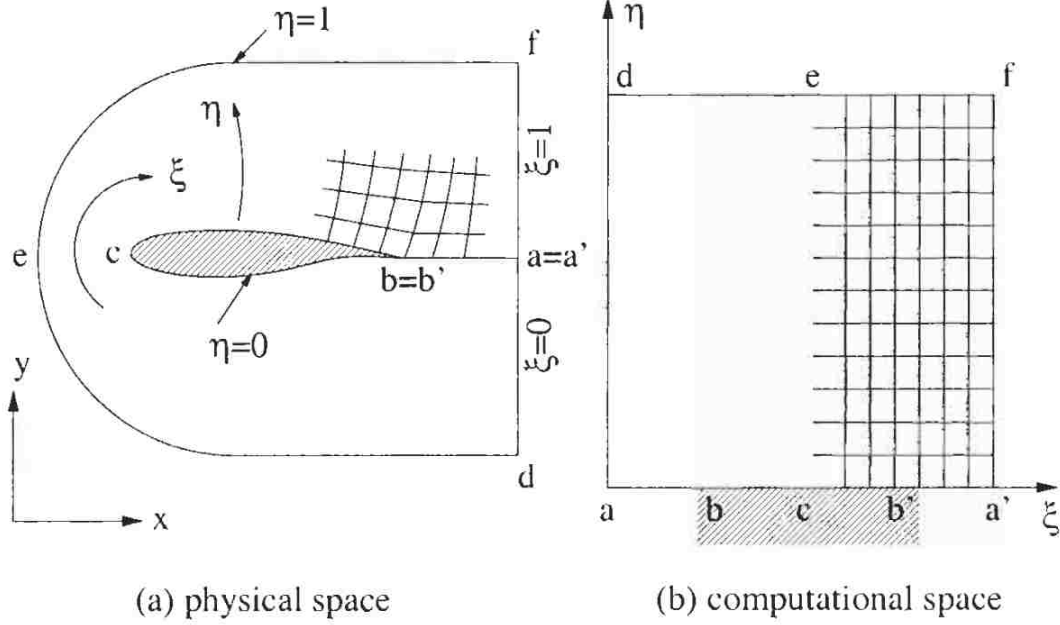
Figure 2.1 – The mapping of physical space to computational space using the curvilinear coordinate transform (Reproduced from Ref. [38]

point. The inviscid and viscous fluxes are evaluated at the interfaces between cells and integrated over all the faces of a cell to determine the time rate of change of conserved quantities within the cell at each timestep. The curvilinear form of the RANS equations can be written in semi-discrete form using the finite volume transformation as,

$$\frac{\partial \tilde{\mathbf{Q}}}{\partial t} = -\frac{\tilde{\mathbf{F}}_{j+\frac{1}{2}} - \tilde{\mathbf{F}}_{j-\frac{1}{2}}}{\Delta \xi} - \frac{\tilde{\mathbf{G}}_{k+\frac{1}{2}} - \tilde{\mathbf{G}}_{k-\frac{1}{2}}}{\Delta \eta} - \frac{\tilde{\mathbf{H}}_{l+\frac{1}{2}} - \tilde{\mathbf{H}}_{l-\frac{1}{2}}}{\Delta \zeta} + \tilde{\mathbf{S}}_{j,k,l} \tag{2.36}$$

2.5.1 Inviscid Fluxes

The inviscid fluxes describe the convection of flow field variables between computation cells. Two steps are involved in the calculation of the inviscid fluxes Eqs. (2.4) – (2.6):

46
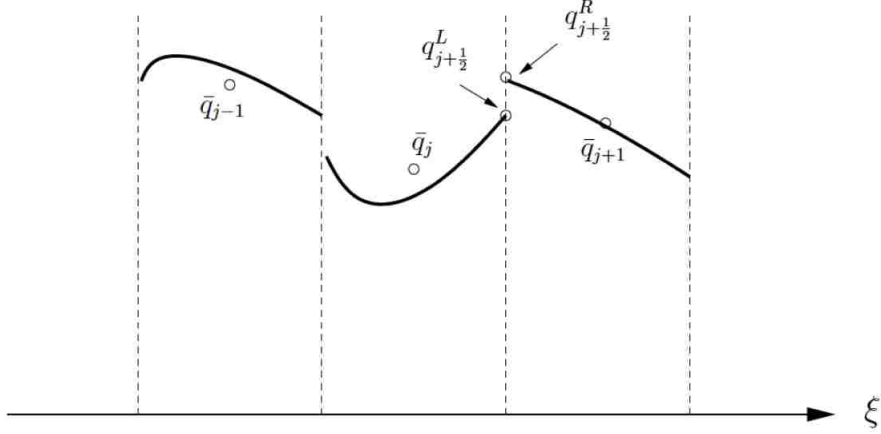
Figure 2.2 – Schematic showing a one-dimensional piecewise reconstruction

1. The primitive variables, (ρ, u, v, w, p), are reconstructed at the cell faces

2. The fluxes are evaluated at the cell faces using the reconstructed primitive variables

Upwind reconstruction schemes account for the direction of wave propagation and ensure that only upstream information is used. In this work, the third-order Monotone Upstream-Centered Scheme for Conservation Laws (MUSCL) [39] with Koren's limiter [40] is used for reconstructing the left and right states at each cell. The left and right face states at each cell interface, $\left(q^L_{i+\frac{1}{2}}, q^R_{i-\frac{1}{2}}\right)$, are calculated based on the current and neighboring cell-averaged values, i.e. $\bar{q}_{i-1}$, $\bar{q}_i$, and $\bar{q}_{i+1}$. Figure 2.2 illustrates a one-dimensional piecewise reconstruction.

Using the reconstructed left and right states, the inviscid fluxes can be computed at each face. Roe's flux difference splitting scheme [41] with an entropy fix is used to compute the left and right state fluxes, $\mathbf{F}_L$ and $\mathbf{F}_R$,

$$\mathbf{F}(q^L, q^R) = \frac{\mathbf{F}(q^L) + \mathbf{F}(q^R)}{2} - |\tilde{\mathbf{A}}(q^L, q^R)|\frac{q^R - q^L}{2} \tag{2.37}$$

where $\tilde{A}$ is the Roe-averaged Jacobian matrix. Harten's entropy correction to the eigenvalues, λ, of the flux Jacobian, $\tilde{\mathbf{A}}$, is given by,

$$|\lambda| = \begin{cases} |\lambda|, & \text{if} |\lambda| > \delta \\ \frac{\lambda^2 + \delta^2}{2\delta}, & \text{if} |\lambda| \leq \delta \end{cases} \tag{2.38}$$

where $\delta = \max\left[0, (\overline{\lambda}_{i+1/2} - \overline{\lambda}_i), (\overline{\lambda}_{i+1} - \overline{\lambda}_{i+1/2})\right]$.

2.5.2 Viscous Fluxes

The viscous fluxes in the curvilinear form of the governing equations include derivatives of the following form,

$$\frac{\partial}{\partial \xi}\left(\alpha \frac{\partial \beta}{\partial \eta}\right) \tag{2.39}$$

which are evaluated using second order central differencing,

$$\frac{1}{\Delta \xi}\left(\left[\alpha_{j+\frac{1}{2},k}\left(\frac{\beta_{j+\frac{1}{2},k+1} - \beta_{j+\frac{1}{2},k}}{\Delta \eta}\right)\right] - \left[\alpha_{j-\frac{1}{2},k}\left(\frac{\beta_{j-\frac{1}{2},k} - \beta_{j-\frac{1}{2},k-1}}{\Delta \eta}\right)\right]\right) \tag{2.40}$$

where $\delta_{j+\frac{1}{2},k} = \dfrac{\delta_{j,k} + \delta j + 1, k}{2}$ and $\delta = (\alpha, \beta)$.

2.5.3 Turbulence Modeling

The RANS equations avoid the need to model all of the turbulent fluctuations by splitting the dependent variables into a mean component and a fluctuating component. The decomposition results in the addition of several terms that are functions of the fluctuating component, these terms are called the Reynolds stress tensor and is modeled using turbulence models. The most physically realistic turbulence models are called Reynolds Stress Models [42] – [43]. These models solve six

additional transport equations, one for each of the stress tensor components and one for the energy dissipation rate. Transport equations describe how the convection and diffusion for a variable transports it between computational cells. These models are computationally expensive and have issues with robustness and convergence. It is more common for turbulence models to relate the Reynolds stress tensor to the mean strain rate using the Boussinesq eddy viscosity, as shown below,

$$(\overline{\tau_{ij}})_{\text{turb}} = -\overline{\rho u_i' u_j'} = \frac{2}{3}\overline{\rho}k\delta_{ij} - \mu_t\left[\left(\frac{\partial \overline{u_i}}{\partial x_j} + \frac{\partial \overline{u_i}}{\partial x_j}\right) - \frac{2}{3}\frac{\partial \overline{u_k}}{\partial x_k}\delta_{ij}\right] \tag{2.41}$$

where k is the turbulent kinetic energy,

$$k = \frac{1}{2}\left[\overline{(u_1')^2} + \overline{(v_1')^2} + \overline{(w_1')^2}\right] \tag{2.42}$$

and μ_t is the turbulent viscosity or eddy viscosity. Utilizing Eq. (2.41) yields the following form for the total viscous stress tensor,

$$(\overline{\tau_{ij}})_{\text{turb}} = \frac{2}{3}\overline{\rho}k\delta_{ij} - (\mu + \mu_t)\left[\left(\frac{\partial \overline{u_i}}{\partial x_j} + \frac{\partial \overline{u_i}}{\partial x_j}\right) - \frac{2}{3}\frac{\partial \overline{u_k}}{\partial x_k}\delta_{ij}\right] \tag{2.43}$$

Turbulence modeling research has proposed a large variety of models for calculating the turbulent kinetic energy and eddy viscosity as a function of mean flow quantities. Most of the turbulence models are calibrated using theoretical solutions and experimental data, resulting in a significant amount of empiricism inherent to turbulence modeling. One widely used turbulence model, particularly in aerospace applications, is the one-equation Spalart-Allmaras (SA) model [44]. It solves a transport equation for the eddy viscosity. The SA model is used for all turbulent simulations in this work, and the details of this model are presented in the next section.

2.5.4 Spalart-Allmaras (SA) Turbulence Model

The SA turbulence model is widely used turbulence model in aerospace appli-
cations. The SA model relates the Reynolds stresses to the mean strain using the
following isotropic relation,

$$\overline{u_i' u_j'} = -2\mu_t S_{ij} \tag{2.44}$$

The eddy viscosity is related to a turbulence field variable $\tilde{\nu}$ by the following equa-
tion,

$$\mu_t = \rho \nu_t = \rho \tilde{\nu} f_{v1} \tag{2.45}$$

where f_{v1} is a function of $\tilde{\nu}$ and the molecular viscosity, ν, as,

$$f_{v1} = \frac{\chi^3}{\chi^3 + c_{v1}^3} \tag{2.46}$$

where $\chi = \tilde{\nu}/\nu$ and $c_{v1} = 7.1$. The turbulence field variable $\tilde{\nu}$ is determined by
solving the following PDE,

$$\frac{\partial \tilde{\nu}}{\partial t} + u_j \frac{\partial \tilde{\nu}}{\partial x_j} = \frac{1}{\sigma} \left[\frac{\partial}{\partial x_j} \left((\nu + \tilde{\nu}) \frac{\partial \tilde{\nu}}{\partial x_j} \right) + c_{b2} \frac{\partial \tilde{\nu}}{\partial x_i} \frac{\partial \tilde{\nu}}{\partial x_i} \right] + c_{b1} \tilde{S} \tilde{\nu} - c_{w1} f_w \left(\frac{\tilde{\nu}}{d} \right)^2 \tag{2.47}$$

where d is the distance to the nearest wall and

$$\tilde{S} = \max \left[\Omega + \frac{\tilde{\nu}}{\kappa^2 d^2} f_{v2}, 0.3\Omega \right] \tag{2.48}$$

$$f_w = g \left[\frac{1 + c_{w3}^6}{g^6 + c_{w3}^6} \right]^6 \tag{2.49}$$

where Ω is the vorticity magnitude and f_{v2} and g are given by,

$$f_{v2} = 1 - \frac{\chi}{1 + \chi f_{v1}} \tag{2.50}$$

50

$$g = r + c_{w2}(r^6 - r) \tag{2.51}$$

$$r = \min\left[\frac{\tilde{\nu}}{\tilde{S}\kappa^2 d^2}, 10\right] \tag{2.52}$$

where the constants are

$$c_{b1} = 0.1355 \qquad c_{b2} = 0.622 \qquad \kappa = 0.41 \qquad \sigma = \frac{2}{3}$$
$$c_{v1} = 7.1 \qquad c_{w1} = \frac{c_{b1}}{\kappa^2} + \frac{1 + c_{b2}}{\sigma} \qquad c_{w2} = 0.3 \qquad c_{w3} = 2 \tag{2.53}$$

The left hand side of Eq. (2.47) convects the turbulence field variable ($\tilde{\nu}$) at the mean flow velocity (u). On the right hand side of Eq. (2.47) the first term represents diffusion of $\tilde{\nu}$, the second term represents production of $\tilde{\nu}$, and the final term represents destruction of $\tilde{\nu}$.

2.5.4.1 $\gamma - Re_\theta -$ SA Transition Model

Transition modeling is used to improve performance predictions for simulations involving significant amounts of laminar flow. This work utilizes the $\gamma - Re_{\theta t} - SA$ transition model developed by Medida et al. [27]. To control boundary layer transition the production of turbulent kinetic energy is controlled using the local intermittency, γ. The intermittency field is calculated using the intermittency transport equation,

$$\frac{D(\rho\gamma)}{Dt} = P_\gamma - D_\gamma + \frac{\partial}{\partial x_j}\left[\left(\mu + \frac{\mu_t}{\sigma_f}\right)\frac{\partial\gamma}{\partial x_j}\right] \tag{2.54}$$

where

$$P_\gamma = \rho F_{\text{onset}} G_{\text{onset}} \max\left(\frac{\Omega}{F_{\text{length}}}, \frac{1.0}{F_{\text{length,min}}}\right) \tag{2.55}$$

$$\text{If} \quad \gamma > 1.0, \quad P_\gamma = (1 - \gamma)P_\gamma$$

$$D_\gamma = \rho\Omega\gamma(1.0 - G_{\text{onset}}) \tag{2.56}$$

51

$$
G_{\text{onset}} = \begin{cases} 1.0, & \text{if} \quad \max(F_{\text{onset}}) > 1.0 \quad \text{at a given streamwise station} \\ \\ 0.0, & \text{otherwise} \end{cases} \tag{2.57}
$$

$$
F_{\text{onset}} = \max(F_{\text{onset2}} - F_{\text{onset3}}, 0) \tag{2.58}
$$

$$
F_{\text{onset1}} = \frac{Re_\nu}{2.193 Re_{\theta c}} \tag{2.59}
$$

$$
F_{\text{onset2}} = \min(\max(F_{\text{onset1}}, F_{\text{onset1}}^4), 4.0) \tag{2.60}
$$

$$
F_{\text{onset3}} = max(2 - (0.25 R_T)^3, 0) \tag{2.61}
$$

$$
Re_\nu = \frac{\rho d^2 S}{\mu}, \qquad Re_{\theta c} = 0.62 \overline{Re_{\theta t}}, \qquad R_T = \frac{\mu}{\mu_t} \tag{2.62}
$$

$$
F_{\text{length}} = 40.0, \qquad F_{\text{length,min}} = 2.5 \tag{2.63}
$$

The critical Reynolds number, $Re_{\theta c}$, determines the transition onset locations, which is where intermittency starts to increase in the boundary layer. The length of the transition region is determined based on the F_{length} function. Both of these values are calculated using correlations based on the local transition momentum thickness, $\overline{Re_{\theta t}}$. Another transport equation is solved to yield the $\overline{Re_{\theta t}}$ field,

$$
\frac{D(\rho \overline{Re_{\theta t}})}{Dt} = P_{\theta t} + \frac{\partial}{\partial x_j} \left[\sigma_{\theta t}(\mu + \mu_t) \frac{\partial \overline{RE_{\theta t}}}{\partial x_j} \right] \tag{2.64}
$$

where

$$
P_{\theta t} = c_{\theta t} \frac{\rho}{t} (Re_{\theta t} - \overline{Re_{\theta t}})(1.0 - F_{\theta t}) \tag{2.65}
$$

$$
F_{\theta t} = \min \left(e^{-\left(\frac{d}{\delta}\right)^4}, 1.0 \right) \tag{2.66}
$$

$$
\theta_{\text{BL}} = \frac{\overline{Re_{\theta t}} \mu}{\rho U}, \qquad \delta_{\text{BL}} = 7.5 \theta_{\text{BL}}, \qquad \delta = \frac{50 \Omega d}{U} \delta_{\text{BL}} \tag{2.67}
$$

Experimental correlations are used to determine the value of $Re_{\theta t}$, the value of $Re_{\theta t_\infty}$ is based on the freestream turbulence using a piecewise linear interpolation of the values given in Table 2.1. The value of $Re_{\theta t}$ is determined as follows,

$$Re_{\theta t} = Re_{\theta t_\infty} F(\lambda_\theta) \tag{2.68}$$

$$F(\lambda_\theta) = \begin{cases} 1 - (-12.986\lambda_\theta - 123.66\lambda_\theta^2 - 405.689\lambda_\theta^3)e^{-\left(\frac{Tu}{1.5}\right)^{1.5}}, & \lambda_\theta \leq 0 \\ \\ 1 + 0.275(1 - e^{-35\lambda_\theta})e^{-\frac{Tu}{0.5}}, & \lambda_\theta > 0 \end{cases} \tag{2.69}$$

$$\lambda_\theta = \frac{\rho\theta^2}{\mu}\frac{dU}{ds} \tag{2.70}$$

$$\sigma_f = 1.0, \qquad c_{\theta t} = 0.03, \qquad \sigma_{\theta t} = 2.0 \tag{2.71}$$

$Tu\%$	$Re_{\theta t_\infty}$
0.01	1800.0
0.03	1135.0
0.51	894.0
1.33	392.0
2.00	252.0
5.25	165.0
6.50	100.0

Table 2.1 – Piecewise linear correlations between Tu and $Re_{\theta t_\infty}$

2.5.4.2 Adverse Pressure Gradient Correction

To improve the sensitivity of the SA model to strong adverse pressure gradients Medida et al. [26] developed the adverse pressure gradient (APG) correction. Strong adverse pressure gradients primarily affect the defect layer, in the SA model the behavior of the defect layer can be modified through the damping function f_w, (2.49),

in the destruction term of the turbulence transport equation, Eq. (2.47). To increase turbulence destruction the von-Karman constant, κ, is lowered for non-equilibrium boundary layers. The decrease in κ is only for numerical purposes and does not reflect the nature of the log-law slope under strong APG. Recall that,

$$f_w = g \left[\frac{1 + c_{w3}^6}{g^6 + c_{w3}^6} \right]^6, \qquad g = r + c_{w2}(r^6 - r), \qquad r = \min \left[\frac{\tilde{\nu}}{\tilde{S}\kappa^2 d^2}, 10 \right] \qquad (2.72)$$

The APG correction modifies the calculation of r as follows,

$$r = \min \left[\frac{\tilde{\nu}}{\tilde{S}\alpha^2 d^2}, 10 \right] \qquad (2.73)$$

where

$$\alpha = \kappa - 0.2\beta, \qquad \beta = \min(\max(\delta^8 - 1.0, 0.0), 1.0), \qquad \delta = \frac{\mu_t |S_{ij}|}{1.5 |\tau_w|} \qquad (2.74)$$

The value of δ is based on the observation that the ratio of the local turbulent shear stress magnitude to the wall shear stress magnitude does not exceed 1.5 for equilibrium boundary layers.

2.5.4.3   Delayed Detached Eddy Simulation

Delayed Detached Eddy Simulation (DDES) is a hybrid RANS-LES method developed by Spalart et al. [45]. DDES is based on DES, a modification of the one equation SA model that reduces to a subgrid model outside the boundary layer while maintaining RANS behavior inside the boundary layer. To accomplish this DES replaces the length scale, d in the turbulence transport equation, (2.47), by $\tilde{d}$, which is given by,

$$\tilde{d} = \min(d, C_{\text{DES}}\Delta) \qquad (2.75)$$

where C_{DES} is a constant and typically,

$$\Delta = \max(\Delta x, \Delta y, \Delta z) \tag{2.76}$$

The implementation used in this work has been further modified based on the anisotropic grid correction of Scotti et al. [46]. The correction modifies the definition of Δ to be the following,

$$\Delta = \cosh\left(\sqrt{\frac{4}{27}[\ln(a_1)^2 - \ln(a_1)\ln(a_2) + \ln(a_2)^2]}\right) \times (\Delta x \times \Delta y \times \Delta z)^{\frac{1}{3}} \tag{2.77}$$

This formulation for $\tilde{d}$ depends only on d and Δ, which are both grid quantities. In cases with thick boundary layers or shallow separation regions, this can cause an issue known as modeled stress depletion (MSD). MSD is where the DES limiter is activated within the boundary, but the grid is not fine enough to handle the associated LES content. The result is a reduction in the modeled Reynolds stress, which can lead to premature separation, known as grid induced separation. The DDES formulation modifies $\tilde{d}$ to also depend on the eddy viscosity, the new definition is given by,

$$\tilde{d} = d - f_d\max(0, d - D_{\text{DES}}\Delta) \tag{2.78}$$

$$f_d = 1 - \tanh([8r_d]^3) \tag{2.79}$$

$$r_d = \frac{\nu_t + \nu}{\sqrt{U_{i,j}U_{i,j}}\kappa^2 d^2} \tag{2.80}$$

The added eddy viscosity dependence ensures that the DES limiter is not activated inside the boundary layer. LES behavior is still maintained for massively separated flows.

2.5.5 Time Integration

Time integration is used to calculate values for the flow variables at the next timestep based on their current values. After the inviscid Eqs. (2.4) – (2.6) and viscous fluxes Eqs. (2.7) – (2.9) on the right hand side of the semi-discrete RANS equations, Eq. (2.36), are evaluated, the semi-discrete RANS equations are integrated using an implicit (backwards-in-time) time marching method. An implicit method is employed as these methods have superior stability and convergence characteristics when compared to explicit time marching methods. Implicit methods require the fluxes and source terms on the right-hand side of the semi-discrete equations to be evaluated at the current time level. The semi-discrete equations, Eq. (2.36), discretized using using an implicit method are expressed as,

$$\frac{\partial \tilde{\mathbf{Q}}^{n+1}}{\partial t} = -\frac{\tilde{\mathbf{F}}^{n+1}_{j+\frac{1}{2}} - \tilde{\mathbf{F}}^{n+1}_{j-\frac{1}{2}}}{\Delta \xi} - \frac{\tilde{\mathbf{G}}^{n+1}_{k+\frac{1}{2}} - \tilde{\mathbf{G}}^{n+1}_{k-\frac{1}{2}}}{\Delta \eta} - \frac{\tilde{\mathbf{H}}^{n+1}_{l+\frac{1}{2}} - \tilde{\mathbf{H}}^{n+1}_{l-\frac{1}{2}}}{\Delta \zeta} + \tilde{\mathbf{S}}^{n+1}_{j,k,l} \qquad (2.81)$$

In this work a first-order accurate implicit method (Euler implicit) is used, so the left-hand side can be written as follows,

$$\frac{\partial \tilde{\mathbf{Q}}^{n+1}}{\partial t} \simeq \frac{\tilde{\mathbf{Q}}^{n+1} - \tilde{\mathbf{Q}}^n}{\Delta t} + O(\Delta t) \qquad (2.82)$$

By linearizing the non-linear equation around $\tilde{\mathbf{Q}}^n$ using a Taylor series expansion the $(n+1)^{th}$ state can be expressed in terms of the previous state. The resulting equations are as follows,

$$\tilde{\mathbf{F}}^{n+1} = \tilde{\mathbf{F}}^n + \tilde{\mathbf{A}}\Delta\tilde{\mathbf{Q}} + O(\Delta t^2) \qquad (2.83)$$

$$\tilde{\mathbf{G}}^{n+1} = \tilde{\mathbf{G}}^n + \tilde{\mathbf{B}}\Delta\tilde{\mathbf{Q}} + O(\Delta t^2) \qquad (2.84)$$

$$\tilde{\mathbf{H}}^{n+1} = \tilde{\mathbf{H}}^n + \tilde{\mathbf{C}}\Delta\tilde{\mathbf{Q}} + O(\Delta t^2) \tag{2.85}$$

where $\Delta\tilde{\mathbf{Q}} = \tilde{\mathbf{Q}}^{n+1} - \tilde{\mathbf{Q}}^n$ and $\tilde{\mathbf{A}}$, $\tilde{\mathbf{B}}$, and $\tilde{\mathbf{C}}$ are the flux Jacobians given by $\frac{\partial\tilde{\mathbf{F}}}{\partial\tilde{\mathbf{Q}}}$, $\frac{\partial\tilde{\mathbf{G}}}{\partial\tilde{\mathbf{Q}}}$, and $\frac{\partial\tilde{\mathbf{H}}}{\partial\tilde{\mathbf{Q}}}$. The linearized equations can be expressed in terms of the solution update $\Delta\tilde{\mathbf{Q}}$ as follows,

$$[I + \Delta t(\delta_\xi\tilde{\mathbf{A}}^n + \delta_\eta\tilde{\mathbf{B}}^n + \delta_\zeta\tilde{\mathbf{C}}^n)]\Delta\tilde{\mathbf{Q}} = -\Delta t(\delta_\xi\tilde{\mathbf{F}}^n + \delta_\eta\tilde{\mathbf{G}}^n + \delta_\zeta\tilde{\mathbf{H}}^n - \tilde{\mathbf{S}}^n) \tag{2.86}$$

The right-hand side of Eq. (2.86) represents the physics of the problem while the left-hand side of Eq. (2.86) represents the numerics of the problem, which determines solution stability and convergence. The system of equations results in a sparse banded matrix of algebraic equations. While it is not computationally feasible to directly invert the matrix, therefore approximate factorization methods are used to make the inversion computationally efficient, even though there may be a degradation in stability and convergence. The two methods utilized in this work are the Lower-Upper Symmetric Gauss-Seidel (LUSGS) algorithm and the Diagonalized Alternating Direction Implicit (DADI) algorithm. All OverTURNS simulations utilize the LUSGS algorithm while all of the GPU-RANS solver simulations utilize the DADI algorithm, this is because the DADI algorithm is more amenable to parallelization in the GPU framework than the LUSGS algorithm.

2.5.5.1   Lower-Upper Symmetric Gauss-Seidel (LUSGS) Algorithm

The LUSGS algorithm is an approximate factorization method that factorizes the left-hand side of the linearized form of the semi-discrete RANS equations [47], given by Eq. (2.86). This factorization groups terms into a lower diagonal (L), an

upper diagonal (U), and a main diagonal (D) with the following form,

$$[L+D+U]\Delta\tilde{\mathbf{Q}}^n \approx [D+L]D^{-1}[D+U]\Delta\tilde{\mathbf{Q}}^n = -\Delta t(\delta_\xi\tilde{\mathbf{F}}^n+\delta_\eta\tilde{\mathbf{G}}^n+\delta_\zeta\tilde{\mathbf{H}}^n-\tilde{\mathbf{S}}^n) \quad (2.87)$$

where

$$L = \Delta t(-\tilde{\mathbf{A}}^+_{j-1,k,l} - \tilde{\mathbf{B}}^+_{j,k-1,l} - \tilde{\mathbf{C}}^+_{j,k,l-1})$$

$$U = \Delta t(\tilde{\mathbf{A}}^-_{j+1,k,l} + \tilde{\mathbf{B}}^-_{j,k+1,l} + \tilde{\mathbf{C}}^-_{j,k,l+1}) \qquad (2.88)$$

$$D = I + \Delta t(\tilde{\mathbf{A}}^+_{j,k,l} - \tilde{\mathbf{A}}^-_{j,k,l} + \tilde{\mathbf{B}}^+_{j,k,l} - \tilde{\mathbf{B}}^-_{j,k,l} + \tilde{\mathbf{C}}^+_{j,k,l} - \tilde{\mathbf{C}}^-_{j,k,l})$$

The solution update $(\Delta\tilde{Q})$ can be determined by using two steps to solve the system defined by Eq. (2.87) and Eq. (2.88) as follows,

$$[D + L]\Delta\overline{\mathbf{Q}} = -\Delta t(\delta_\xi\tilde{\mathbf{F}}^n + \delta_\eta\tilde{\mathbf{G}}^n + \delta_\zeta\tilde{\mathbf{H}}^n - \tilde{\mathbf{S}}^n) \qquad (2.89)$$

$$[D + U]\Delta\tilde{\mathbf{Q}} = D\Delta\overline{\mathbf{Q}} \qquad (2.90)$$

L, D, and U are block matrices with a size of 5×5 for the three dimensional Navier–Stokes equations, and consequently it is computationally expensive to invert the $[D + L]$ and $[D + U]$ terms. The spectral radius approximation is used for the flux Jacobian matrices $(\tilde{\mathbf{A}}, \tilde{\mathbf{B}}, \tilde{\mathbf{C}})$ to reduce the main diagonal (D) to a diagonal matrix. The spectral radius approximation implementation is given by,

$$\tilde{\mathbf{A}}^+ = \frac{1}{2}(\tilde{\mathbf{A}} + \sigma_\xi), \qquad \tilde{\mathbf{A}}^- = \frac{1}{2}(\tilde{\mathbf{A}} - \sigma_\xi)$$

$$\tilde{\mathbf{B}}^+ = \frac{1}{2}(\tilde{\mathbf{B}} + \sigma_\eta), \qquad \tilde{\mathbf{B}}^- = \frac{1}{2}(\tilde{\mathbf{B}} - \sigma_\eta) \qquad (2.91)$$

$$\tilde{\mathbf{C}}^+ = \frac{1}{2}(\tilde{\mathbf{C}} + \sigma_\zeta), \qquad \tilde{\mathbf{C}}^- = \frac{1}{2}(\tilde{\mathbf{C}} - \sigma_\zeta)$$

where $\tilde{\mathbf{A}}^{+-}$,$\tilde{\mathbf{B}}^{+-}$, and $\tilde{\mathbf{C}}^{+-}$ are the left and right flux Jacobians and,

$$\sigma_\xi = |U_\xi| + c + \frac{2\mu(\xi_x^2 + \xi_y^2 + \xi_z^2)}{\rho}$$

$$\sigma_\eta = |U_\eta| + c + \frac{2\mu(\eta_x^2 + \eta_y^2 + \eta_z^2)}{\rho} \tag{2.92}$$

$$\sigma_\zeta = |U_\zeta| + c + \frac{2\mu(\zeta_x^2 + \zeta_y^2 + \zeta_z^2)}{\rho}$$

where U_k is the contravariant velocity in the k-direction. Errors associated with the approximate factorization are reduced using a dual time stepping method with Newton-like sub-iterations, which is described in Section 2.5.5.3.

2.5.5.2 Diagonalized Alternating Direction Implicit (DADI) Algorithm

The DADI algorithm developed by Pulliam and Chaussee [48] can be used to invert the left-hand side of the linearized form of the semi-discrete RANS equations, given by Eq. (2.36). Since the simulations are in three dimensions the left-hand side of Eq. (2.36) is split into three factors as follows,

$$[I + \Delta t(\delta_\xi \tilde{\mathbf{A}} + \delta_\eta \tilde{\mathbf{B}} + \delta_\zeta \tilde{\mathbf{C}})]\Delta \tilde{\mathbf{Q}} \approx [I + \Delta t \delta_\xi \tilde{\mathbf{A}}][I + \Delta t \delta_\eta \tilde{\mathbf{B}}][I + \Delta t \delta_\zeta \tilde{\mathbf{C}}]$$

$$= -\Delta t(\delta_\xi \tilde{\mathbf{F}}^n + \delta_\eta \tilde{\mathbf{G}}^n + \delta_\zeta \tilde{\mathbf{H}}^n - \tilde{\mathbf{S}}^n) \tag{2.93}$$

A further simplification can be made by diagonalizing the inviscid components of the flux Jacobians, resulting in the following terms,

$$\tilde{\mathbf{A}} = T_\xi \Lambda_\xi T_\xi^{-1}$$

$$\tilde{\mathbf{B}} = T_\eta \Lambda_\eta T_\eta^{-1} \tag{2.94}$$

$$\tilde{\mathbf{C}} = T_\zeta \Lambda_\zeta T_\zeta^{-1}$$

where Λ_ξ is the set of eigenvalues for matrix, T_ξ is set of left eigenvectors, and T_ξ^{-1} is the set of right eigenvectors for matrix $\tilde{A}$. Similar expressions are obtained for matrices $\tilde{B}$ and $\tilde{C}$. After substituting the diagonalized flux Jacobians, Eq. (2.94), for the flux Jacobians in Eq. (2.86) the left-hand side of Eq. (2.86) can be written as,

$$[T_\xi T_\xi^{-1} + (I + \Delta t \delta_\xi T_\xi \Lambda_\xi T_\xi^{-1})][T_\eta T_\eta^{-1} + (I + \Delta t \delta_\eta T_\eta \Lambda_\eta T_\eta^{-1})]$$
$$[T_\zeta T_\zeta^{-1} + (I + \Delta t \delta_\zeta T_\zeta \Lambda_\zeta T_\zeta^{-1})]\Delta\tilde{Q} = \Delta t(\delta_\xi \tilde{F}^n + \delta_\eta \tilde{G}^n + \delta_\zeta \tilde{H}^n - \tilde{S}^n)$$

(2.95)

Assuming the inviscid flux Jacobian eigenvectors are locally constant results in the following,

$$[T_\xi(I+\Delta t \delta_\xi \Lambda_\xi)T_\xi^{-1}][T_\eta(I+\Delta t \delta_\eta \Lambda_\eta)T_\eta^{-1}][T_\zeta(I+\Delta t \delta_\zeta \Lambda_\zeta)T_\zeta^{-1}]\Delta\tilde{Q} = \Delta t(\delta_\xi \tilde{F}^n+\delta_\eta \tilde{G}^n+\delta_\zeta \tilde{H}^n-\tilde{S}^n)$$

(2.96)

The system can now be inverted using the following seven steps,

$$S_1 = T_\xi^{-1}\Delta t(\delta_\xi \tilde{F}^n + \delta_\eta \tilde{G}^n + \delta_\zeta \tilde{H}^n - \tilde{S}^n)$$

$$S_2 = (I + \Delta t \delta_\xi \Lambda_\xi)^{-1}S_1$$

$$S_3 = (T_\xi^{-1}T_\eta)^{-1}S_2$$

$$S_4 = (I + \Delta t \delta_\eta \Lambda_\eta)^{-1}S_3$$

(2.97)

$$S_5 = (T_\eta^{-1}T_\zeta)^{-1}S_4$$

$$S_6 = (I + \Delta t \delta_\zeta \Lambda_\zeta)^{-1}S_5$$

$$\Delta\tilde{Q} = T_\zeta S_6$$

The resulting process reduces the inversion of the left hand side of Eq. (2.86) into four matrix vector products for each cell and five scalar tridiagonal solves per coordinate line, Eq. (2.97).

The algorithm is only rigorously valid for the Euler equations as the viscous flux Jacobians cannot be diagonalized simultaneously along with the inviscid flux Jacobians. To overcome this limitation, the viscous Jacobian eigenvalues, Λ_v, are approximated as follows,

$$\Lambda_v(\xi) = \gamma \mu Re^{-1} \rho^{-1} J^{-1}$$

$$\Lambda_v(\eta) = \gamma \mu Re^{-1} \rho^{-1} J^{-1} \tag{2.98}$$

$$\Lambda_v(\zeta) = \gamma \mu Re^{-1} \rho^{-1} J^{-1}$$

which results in the following equation that can be solved using the same seven step method in Eq. (2.86),

$$[T_\xi(I + \Delta t(\delta_\xi \Lambda_\xi - \delta_{\xi\xi} \Lambda_v(\xi))) T_\xi^{-1}][T_\eta(I + \Delta t(\delta_\eta \Lambda_\eta - \delta_{\eta\eta} \Lambda_v(\eta))) T_\eta^{-1}]$$
$$[T_\zeta(I + \Delta t(\delta_\zeta \Lambda_\zeta - \delta_{\zeta\zeta} \Lambda_v(\zeta))) T_\zeta^{-1}]\Delta \tilde{\mathbf{Q}} = \Delta t(\delta_\xi \tilde{\mathbf{F}}^n + \delta_\eta \tilde{\mathbf{G}}^n + \delta_\zeta \tilde{\mathbf{H}}^n - \tilde{\mathbf{S}}^n) \tag{2.99}$$

The second derivatives in the above equation are computed using second order central differencing. Errors associated with the approximate factorization are reduced using a dual time stepping method with Newton-like sub-iterations, which is described in Section 2.5.5.3.

2.5.5.3 Dual Time Stepping

Sub-iterations can be carried out at each physical timestep to remove factorization errors and recover accuracy in time. To perform subiterations, Eq. (2.33) can be modified to include a term that includes a fictitious pseudo time τ [49].

$$\frac{\partial \tilde{\mathbf{Q}}}{\partial \tau} + \frac{\partial \tilde{\mathbf{Q}}}{\partial t} + \frac{\partial \tilde{\mathbf{F}}}{\partial \xi} + \frac{\partial \tilde{\mathbf{G}}}{\partial \eta} + \frac{\partial \tilde{\mathbf{H}}}{\partial \zeta} = \tilde{\mathbf{S}} \tag{2.100}$$

Discretizing Eq. (2.100) results in the following,

$$\frac{\tilde{\mathbf{Q}}^{p+1} - \tilde{\mathbf{Q}}^{p}}{\Delta\tau} + \frac{\tilde{\mathbf{Q}}^{p+1} - \tilde{\mathbf{Q}}^{n}}{\Delta t} = -\frac{\tilde{\mathbf{F}}_{j+\frac{1}{2}}^{p+1} - \tilde{\mathbf{F}}_{j-\frac{1}{2}}^{p+1}}{\Delta\xi} - \frac{\tilde{\mathbf{G}}_{k+\frac{1}{2}}^{p+1} - \tilde{\mathbf{G}}_{k-\frac{1}{2}}^{p+1}}{\Delta\eta} - \frac{\tilde{\mathbf{H}}_{l+\frac{1}{2}}^{p+1} - \tilde{\mathbf{H}}_{l-\frac{1}{2}}^{p+1}}{\Delta\zeta} + \tilde{\mathbf{S}}_{j,k,l}^{p+1}$$

(2.101)

where the physical time level is denoted by n and the sub-iteration time-level is denoted by p. $\tilde{\mathbf{Q}}^{p}$ is set to $\tilde{\mathbf{Q}}^{n}$ for the first sub-iteration. The system of equations in Eq. (2.100) can be linearized about time level n, resulting in,

$$\left[\frac{1}{\Delta\tau} + \frac{1}{\Delta t} + (\delta_\xi \tilde{\mathbf{A}}^p + \delta_\eta \tilde{\mathbf{B}}^p + \delta_\zeta \tilde{\mathbf{C}}^p)\right] \Delta\tilde{\mathbf{Q}} =$$
$$- \left(\delta_\xi \tilde{\mathbf{F}}^p + \delta_\eta \tilde{\mathbf{G}}^p + \delta_\zeta \tilde{\mathbf{H}}^p - \tilde{\mathbf{S}}^p + \frac{\tilde{\mathbf{Q}}^p - \tilde{\mathbf{Q}}^n}{\Delta t}\right)$$

(2.102)

which can be rewritten as,

$$\left[I + h(\delta_\xi \tilde{\mathbf{A}}^p + \delta_\eta \tilde{\mathbf{B}}^p + \delta_\zeta \tilde{\mathbf{C}}^p)\right] \Delta\tilde{\mathbf{Q}} =$$
$$- h\left(\delta_\xi \tilde{\mathbf{F}}^p + \delta_\eta \tilde{\mathbf{G}}^p + \delta_\zeta \tilde{\mathbf{H}}^p - \tilde{\mathbf{S}}^p + \frac{\tilde{\mathbf{Q}}^p - \tilde{\mathbf{Q}}^n}{\Delta t}\right)$$

(2.103)

where $h = \dfrac{\Delta t}{1 + \frac{\Delta t}{\Delta\tau}}$. The resulting equation is similar in form to Eq. (2.86) and can be solved using either LUSGS or DADI, outlined in Sections 2.5.5.1 and 2.5.5.2, respectively. The unsteady residual is given by,

$$\delta_\xi \tilde{\mathbf{F}}^p + \delta_\eta \tilde{\mathbf{G}}^p + \delta_\zeta \tilde{\mathbf{H}}^p - \tilde{\mathbf{S}}^p + \frac{\tilde{\mathbf{Q}}^p - \tilde{\mathbf{Q}}^n}{\Delta t}$$

(2.104)

The unsteady residual should drop towards zero in the sub-iterations to recover time accuracy. A drop in the unsteady residual of one to two orders of magnitude is typically sufficient to ensure that the factorization error is lower than the remaining discretization errors.

2.5.6 Low Mach Number Preconditioning

The methodology as laid out so far is designed to solve the compressible Navier–Stokes in the subsonic and transonic flow regimes. When applied to low-Mach number regimes, i.e. essentially incompressible flows, the rate of convergence is reduced because of the large differences between the acoustic wave speed and the convective wave speed of the Euler equations. Also, the dissipation terms in the Roe's flux difference splitting scheme do not scale down accurately at low Mach numbers, which increases the solution error by causing excessive numerical dissipation. Turkel's preconditioning [50] has been implemented in OverTURNS to overcome this limitation. The GPU-RANS solver does not include low Mach number preconditioning.

2.5.7 Initial and Boundary Conditions

The unsteady Navier–Stokes equations are an Initial Boundary Value Problem, which means that the evolution of the solution is influenced by the initial conditions and boundary conditions of the simulation. To initialize a simulation the primitive variables (ρ, u, v, w, p) must be set at each grid point. In the present work, the entire flow field is initialized to free-stream values. Because of the choice of reference quantities used to non-dimensionalize the RANS equations $\rho_\infty = 1.0$, $p_\infty = \dfrac{1}{\gamma}$, and (u, v, w) are based on the free-stream Mach number components.

The boundary conditions specify the treatment of the boundary cells of the computational domain. The boundaries can be physical, artificial, or numerical. An

example of a physical boundary condition is the solid wall boundary that enforces a no-slip condition. The requirement of having a finite computational domain results in artificial inlet and outlet boundary conditions at the outer boundary of the computational domain. Numerical boundary conditions include the wake-cut found in C-topology meshes and periodicity. The boundary conditions associated with a C-mesh are illustrated in Fig. 2.3.

OverTURNS uses a cell-vertex scheme while the GPU-RANS solver utilizes a cell-centered scheme, Fig. 2.4 illustrates that the difference between the two schemes is the location where flow variables are calculated. Consequently, OverTURNS and the GPU-RANS solver utilize different methods for setting the boundary conditions. OverTURNS explicitly sets the primitive variables at the grid points that lie on the boundary. In the GPU-RANS solver, the boundaries occur on the outer faces of the boundary cells. To set the values at the face a layer of ghost cells surrounding the physical domain is used, the conservative variables inside these ghost cells are extrapolated from interior cells to enforce the desired boundary condition at their associated boundary face.

2.5.7.1 Wall Boundary

At wall boundaries, the density is extrapolated from the interior and the pressure is either extrapolated or calculated using the normal momentum equation. The velocity vector, (u, v, w), is set at the wall boundary to satisfy the no-penetration condition for inviscid walls or the no-slip condition for viscous walls. To enforce a
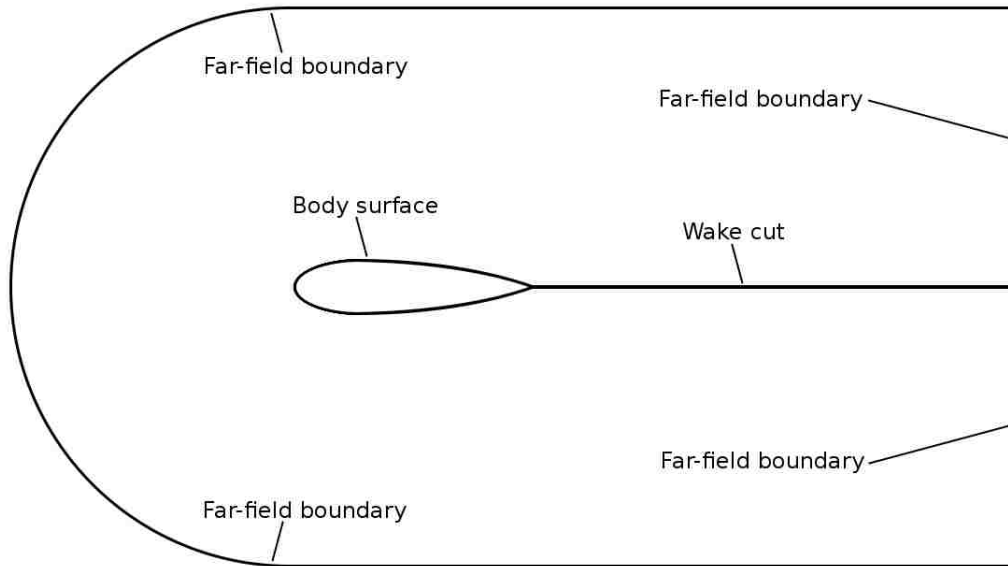
64

Figure 2.3 – Boundary conditions on a structured C-topology mesh

no-penetration condition the wall-normal component of the velocity is set to match the wall-normal component of the surface velocity at that point, the flow velocities tangent to the surface are unaffected. The no-slip condition is enforced by setting all of the velocity components to match their respective surface velocity components.

2.5.7.2 Wake Cut Boundary

In a C-mesh topology the wake cut appears adjacent to the solid wall where the grid planes overlap in the same physical space, as shown in Fig. 2.3. The wake cut is an artifact of topology and not the physical problem. Therefore, flow continuity needs to be ensured across the wake cut. In OverTURNS, flow values along the wake cut are explicitly set to the average of the solution on either side of the wake cut. In the GPU-RANS solver, the conservative variables in the ghost cell are set to match their physical counterparts on the other side of the wake cut.
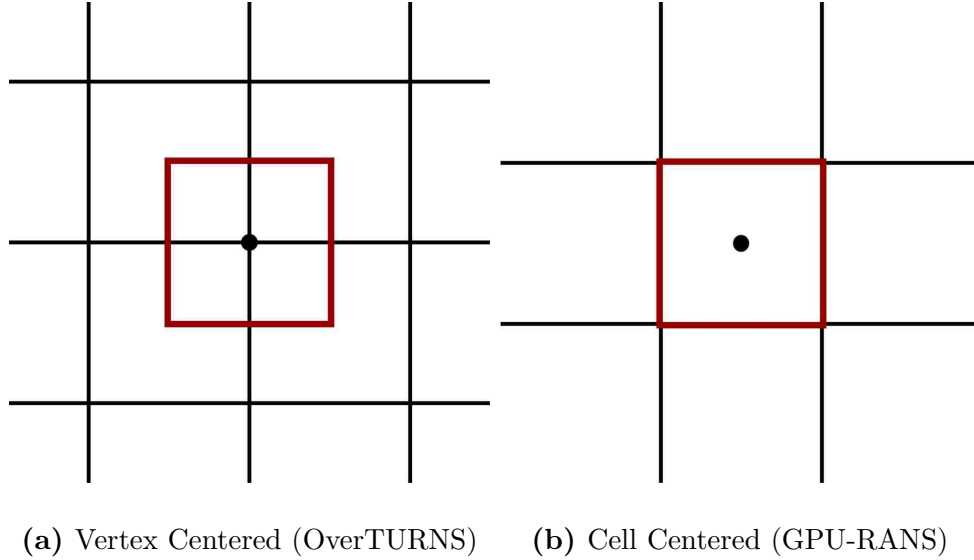
(a) Vertex Centered (OverTURNS)   **(b)** Cell Centered (GPU-RANS)

Figure 2.4 – Control volumes used for vertex centered schemes and cell centered schemes, the red outline is a control volume and the black lines are the computation mesh

2.5.7.3   Periodic Boundary

Some simulations, such as hovering rotors, can be simplified by assuming periodicity in a coordinate direction. To implement the periodic boundary condition, the density and pressure in the ghost cell is set to match the associated physical cell. The velocity vector is also set to match the physical cell, after performing an appropriate coordinate rotation.

2.5.7.4   Far-field Boundary

In external flow simulations an artificial boundary is created when the flow domain is truncated to a finite size. The boundary condition needs to be implemented such that outgoing waves are not spuriously reflected back into the domain, and

only physical disturbances are propagated in the domain from the exterior. Non-reflecting boundary conditions based on the Riemann invariants are used to ensure waves are properly propagated into and out of the domain. On one hand, when the flow is outgoing the Riemann invariants are extrapolated from the interior cells. On the other hand, if the flow is incoming the Riemann invariants are prescribed based on the free-stream values. In the absence of strong flow gradients in the conservative quantities, this boundary condition allows small disturbances to pass through the far-field boundary. In addition, mesh stretching is employed to dissipate strong flow gradients numerically before they reach the far-field boundary. The far-field boundary is typically placed far from the any body surfaces or other regions of flow activity. Two dimensional airfoil simulations typically place the far-field boundary between 20 and 50 chord lengths away from the airfoil surface. Three dimensional rotor simulations typically place the far-field boundary 10 rotor radii from the rotor.

2.5.8   Overset Mesh Connectivity

OverTURNS includes an overset mesh capability. Overset (or chimera) mesh systems are a set of independent computational meshes, and can be used in situations where a single mesh is not feasible. The overset mesh capability also allows for adaptive mesh refinement and modelling complex geometries without requiring the use of an unstructured mesh. Typical uses of overset meshes include multi-element airfoils and for capturing the wake of rotor systems. An important component of the overset methodology is the connectivity and data transfer mechanism. There are

three main steps: hole cutting, receiver point identification, and determining donor cells and interpolation weights. Hole cutting defines regions, called holes, that lie inside solid boundaries. These hole regions are excluded from the solution and a list of receiver points surrounding the hole region is determined. These receiver points are known as hole fringe points, which ensure that points adjacent to hole regions have numerical boundary conditions and are used to propagate information between overlapping meshes. The other receiver points occur on the body mesh (typically towards the outer boundary) where information from other meshes is required. Once receiver cells have been determined, donor cells are chosen with a search algorithm and are used to provide information to the receiver cells. Typically, donor cells are chosen to have similar cell volumes to their associated receiver cells. A weighted sum based on linear interpolation is used to pass information from donor cells to receiver cells. The overset technique is illustrated in Fig. 2.5. A more detailed discussion of the Implicit Hole Cutting algorithm used in OverTURNS is presented in [51] and [52].

2.5.9   Parallelization Techniques

As simulations increase in computational expense, it becomes increasingly important to utilize parallel computing power to decrease the time required to perform these simulations. Two forms of parallelization are presented in this work. The first is used by OverTURNS and is intended to be used with computing clusters. The second is the GPU-acceleration utilized by the GPU-RANS solver, which is targeted
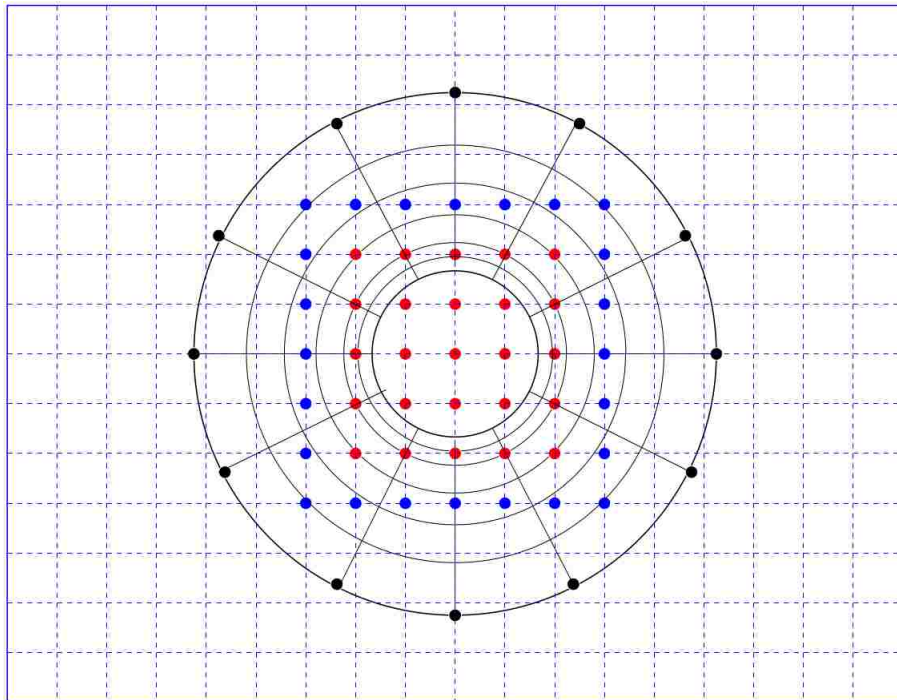
Figure 2.5 – Schematic of the implicit hole cutting technique. Red circles: Hole points, Blue circles: Receiver (hole fringe) points, Black circles: Receiver (Chimera boundary) points. (Reproduced from Ref. [52])

at increasing simulation speeds for a single computer utilizing graphics cards.

2.5.9.1   MPI

The OverTURNS code is capable of running on multiple processors simultaneously by using the Message Passing Interface (MPI) library. The simulation is split using domain decomposition, which splits the computational domain into multiple similarly sized blocks. The governing equations are then solved independently on each of the sub-domains and each sub-domain is assigned its own processor, allowing all of the sub-domains to be solved in parallel. After a timestep has been completed for all of the sub-domains, data is exchanged between blocks that have a common interface using MPI. Figure 2.6 shows the domain decomposition of the Sandia 100m blade computational mesh utilized in the wake capturing results. It should be noted that the blade mesh is only split in the spanwise direction since splitting in the other directions can adversely affect solution convergence and accuracy. This degradation in solution quality arises when there are strong gradients across a domain split, which occurs in regions like the boundary layer where there are strong gradients in the wall-normal direction.

2.5.9.2   GPU

GPUs have been developed to produce real-time, high-definition graphics, as a result they are highly parallel processors with large memory bandwidths. Current high-end GPUs have thousands of cores that can run concurrently allowing for large
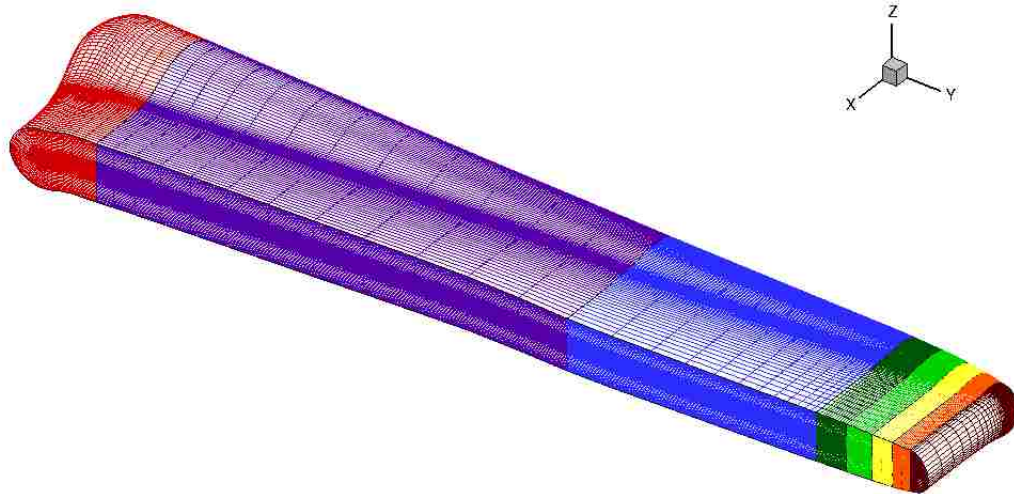
Figure 2.6 – Spanwise domain decomposition of the C-O topology Sandia blade mesh, each sub-domain is represented by a different color

numbers of calculations to be handled in parallel. Applying the capabilities of GPUs to the RANS solver results in a significant speedup of the solver run speed.

The GPU-RANS solver is written using the CUDA programming language [20], which allows programs to utilize the GPU computing resources. Because of memory bandwidth considerations, which determines the speed at which can be passed to and from the GPU, the solver is written to execute almost entirely on the GPU with minimal data transfers to and from the host system. Within the solver there are two types of parallelism.

The first type is fine-grain parallelism. Fine-grain parallelism is used for operations that can be performed independently on all of the cell volumes. Algorithms that can be parallelized in a fine-grain manner include inviscid fluxes, viscous fluxes, and some reconstruction schemes. These calculations are completed by spawning a GPU thread for each cell and running them all in parallel.
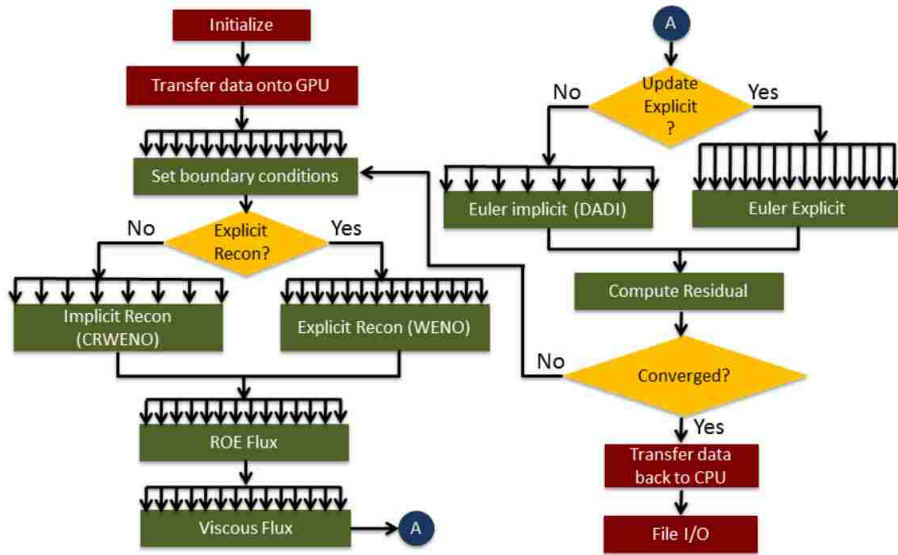
71

Figure 2.7 – Flowchart for the GPU-RANS solver, the level of parallelism (fine-grain vs. coarse-grain) is indicated by the number of arrows

Coarse-grain parallelism is the second type of parallelism found in the GPU-RANS solver. Some operations, such as implicit time stepping, require inverting a linear system that is composed of multiple cells. Each linear system is assigned a GPU thread and all of the systems are solver in parallel. Though schemes that require coarse-grain parallelism suffer from some performance penalty, the advantages associated with the implicit schemes typically offset it. Figure 2.7 shows the structure of the GPU solver and the level of parallelism (fine-grain vs. coarse-grain) is indicated by the number of arrows, with more arrows corresponding to fine-grain parallelism and fewer arrows corresponding to coarse-grain parallelism.

2.6 Summary

The present chapter focused on the governing equations and numerical methodology utilized by OverTURNS and the GPU-RANS solver. The flow field is modeled using the RANS equations, which are discussed in Section 2.3. Reconstruction of the flow variables at cell interfaces was accomplished using the MUSCL scheme. The inviscid fluxes were calculated using Roe's flux difference splitting scheme. The viscous fluxes were evaluated using second order central differencing. The Spalart-Allmaras model, discussed in Sec. 2.5.4, was used for turbulence modeling. The following modifications to the Spalart-Allmaras turbulence models were used:

1. The $\gamma - Re_\theta -$SA transition model was used to model laminar to turbulent transition (Sec. 2.5.4.1)

2. An adverse pressure gradient correction was utilized to improve the sensitivity of the SA model to adverse pressure gradients (Sec. 2.5.4.2)

3. DDES modeling was included to prevent the production of excess modeled turbulence (Sec. 2.5.4.3)

Turkel's low Mach preconditioner was utilized to improve the accuracy and convergence rate for simulations of low speed flows. Connectivity between meshes in the overset mesh system was accomplished using the implicit hole cutting technique outlined in Section 2.5.8. OverTURNS utilizes MPI, discussed in Section 2.5.9.1, to split simulations across multiple computers in a computing cluster. The GPU-RANS solver utilizes GPU acceleration to decrease simulation run time, which is

discussed in Section 2.5.9.2.

Chapter 3: Two Dimensional Airfoil Computational Simulations

In this chapter improved turbulence and transition models (discussed previously in Sec. 2.5.4) were used to simulate several wind turbine airfoils. Two-dimensional simulations of steady flow past the S809 and S827 wind turbine airfoils, shown in Fig. 3.1, were performed for a range of angles of attack and for $\mathrm{Re} = 1 \times 10^6$ and $\mathrm{Re} = 2 \times 10^6$. Airfoil performance data was then extracted from the simulations and was compared to experimental results for lift, drag, skin friction coefficient, and pressure coefficient produced by Somers [8], [17].
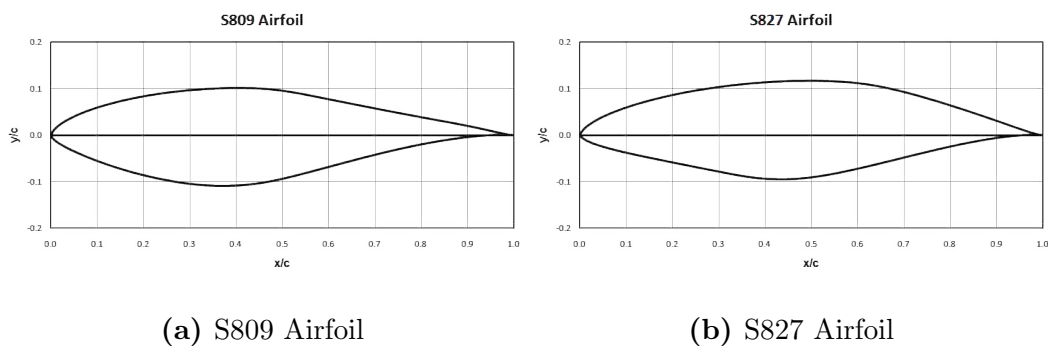

(a) S809 Airfoil   (b) S827 Airfoil

Figure 3.1 – Geometric profiles of the S809 and S827 airfoils

(a) View of entire mesh   **(b)** View of near airfoil region
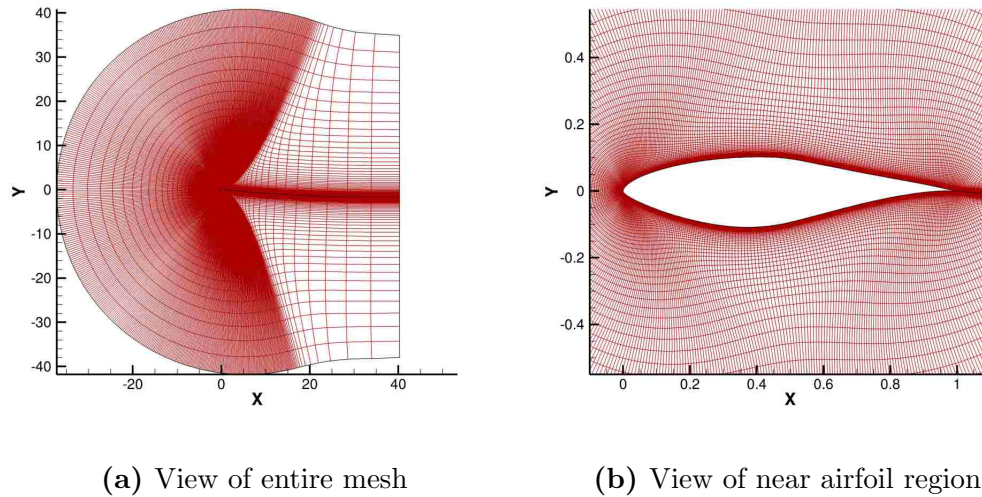
Figure 3.2 – C-mesh utilized for the S809 simulations

3.1   Computational Grids

All two-dimensional simulations utilized structured, body-fitted, C-meshes, such as the one shown in Fig. 3.2. The outer boundary of the meshes was located 40 chords away from the airfoil surface to avoid spurious wave reflections, discussed previously in Sec. 2.5.7.4. The mesh has 491 points in the wrap around direction, with 403 points on the airfoil surface. There are 131 points in the wall-normal direction and the wall grid spacing is chosen to ensure a $y+$ value under 1 for all Reynolds numbers simulated.

3.2   S809 Results

The S809 airfoil is a 21% thick airfoil designed to maintain laminar flow over large portions of its surface. The NREL Phase VI wind turbine rotor utilizes the

S809 airfoil exclusively [10]. Experimental performance data was available from NREL [8]. Two-dimensional flow past an S809 airfoil was simulated at a Mach number of 0.1 and Reynolds numbers of 1×10^6 and 2×10^6. Multiple angles of attack between $0°$ and $20°$ were investigated.

(a) Re $= 1 \times 10^6$ (b) Re $= 2 \times 10^6$
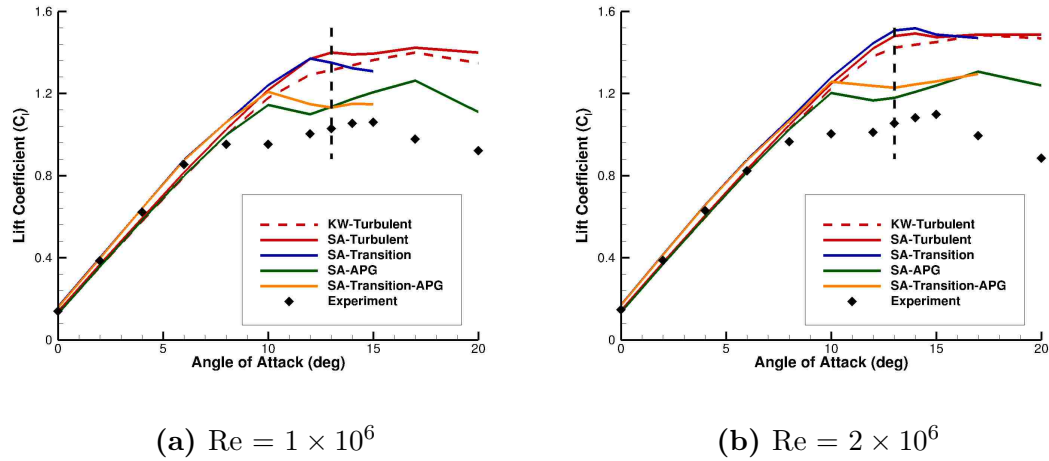
Figure 3.3 – Comparison of lift for S809 airfoil between CFD and experimental data
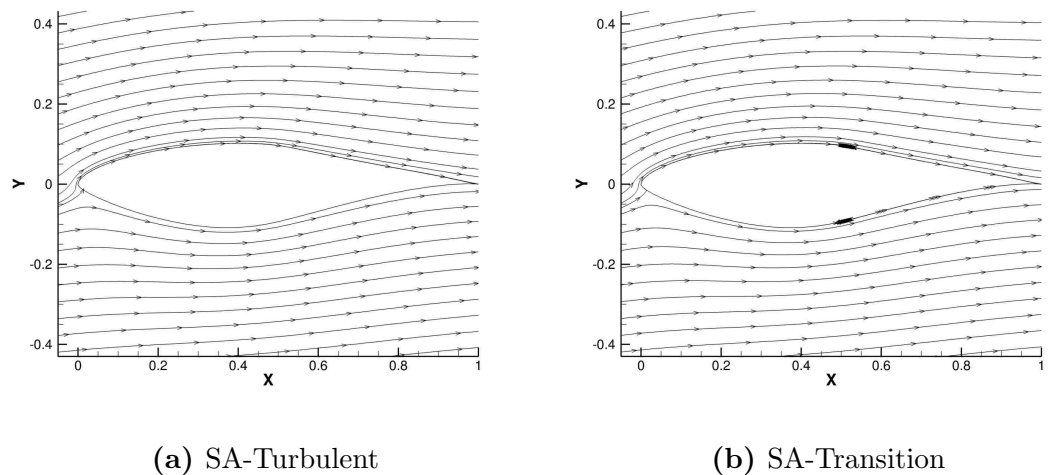

(a) SA-Turbulent   (b) SA-Transition

Figure 3.4 – S809 streamlines at Re $= 1 \times 10^6$ and a $6°$ angle of attack

Figure 3.3 shows plots of the predicted lift coefficients compared to experimen-
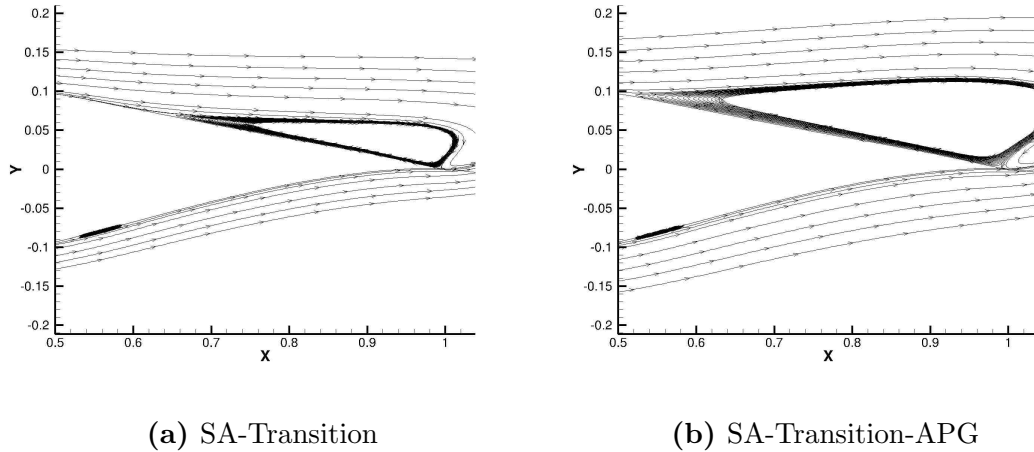
(a) SA-Transition (b) SA-Transition-APG

Figure 3.5 – S809 trailing edge streamlines at Re $= 1 \times 10^6$ and a 13° angle of attack

tal results. At angles of attack above 8° the SA-Turbulent model (hereafter referred to as baseline SA model) significantly over-predicted the angle of attack for stall onset and the maximum lift. The addition of the APG correction lowered predicted lift values at angles of attack above 10° by about 13%, improving agreement of the lift predictions with the experimental results. At angles of attack below 12° the addition of the transition model increased predicted lift slightly, about 5% to 10% compared to the baseline SA model. Figure 3.4 shows streamlines over the S809 airfoil for the baseline SA model and the SA model with transition, which illustrates the lack of separated flow at a 6° angle of attack. The addition of transition modeling captured the laminar separation bubbles on the airfoil, which can be seen in Fig. 3.4b. The lift increase that was observed can be attributed to the laminar separation bubbles increasing the effective camber of the airfoil. Because increasing Reynolds number reduces laminar separation bubble size, the lift increase due to transition modeling is lower for Re $= 2 \times 10^6$ compared to Re $= 1 \times 10^6$. The APG

correction increased the amount of separation predicted at the trailing edge as the airfoil approached stall, shown by the streamlines at the trailing edge plotted in Fig. 3.5 for a 13° angle of attack. There was also a small laminar separation bubble captured on the lower surface, which can be seen in Fig. 3.5, due to the shape of the airfoil creating an adverse pressure gradient that led to the transition onset.
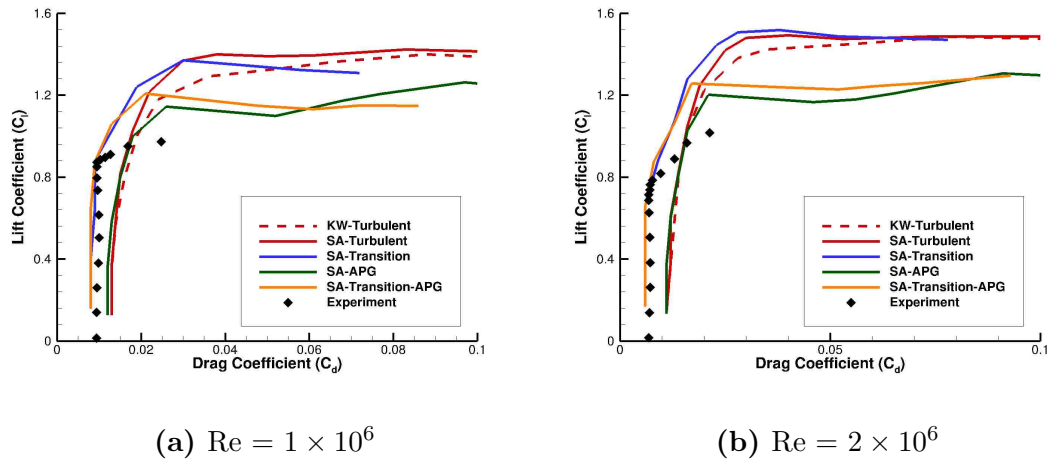

(a) $Re = 1 \times 10^6$

(b) $Re = 2 \times 10^6$

Figure 3.6 – Comparison of drag for S809 airfoil between CFD and experimental data

Focusing on the drag polars for $Re = 1 \times 10^6$ and $Re = 2 \times 10^6$ plotted in Fig. 3.6 it can be seen that at low values of C_l the baseline SA model over-predicted the drag because it was treating the boundary layer as fully turbulent. Adding the transition modeling allowed the region of laminar flow to be captured, lowering predicted drag by 30% to 50%, bringing the predicted drag at low C_l into better agreement with the experimental data. Increasing the Reynolds number reduced the predicted drag for low C_l, which was expected since the increase in Reynolds corresponds to a reduction in the viscous effects responsible for skin friction. The
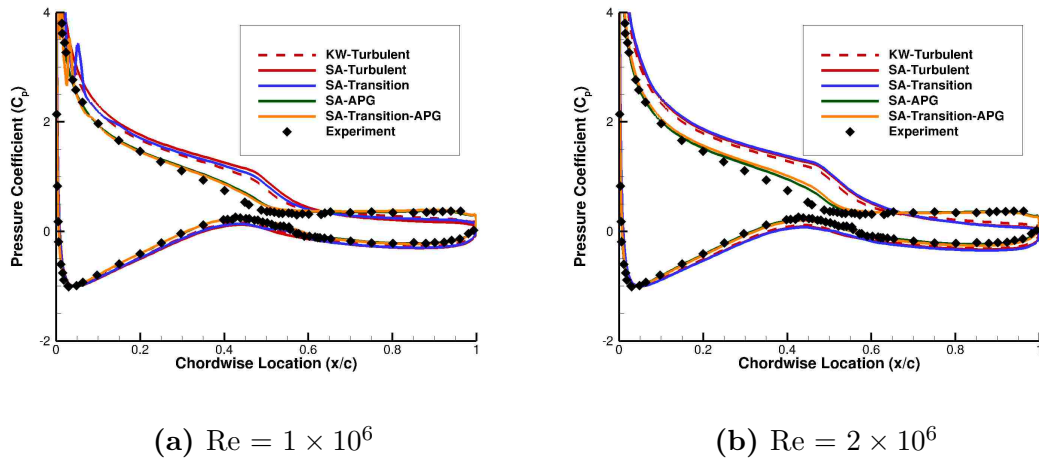
(a) $Re = 1 \times 10^6$ **(b)** $Re = 2 \times 10^6$

Figure 3.7 – Comparison of surface pressure profiles for S809 airfoil between CFD and experimental data at a 13° angle of attack

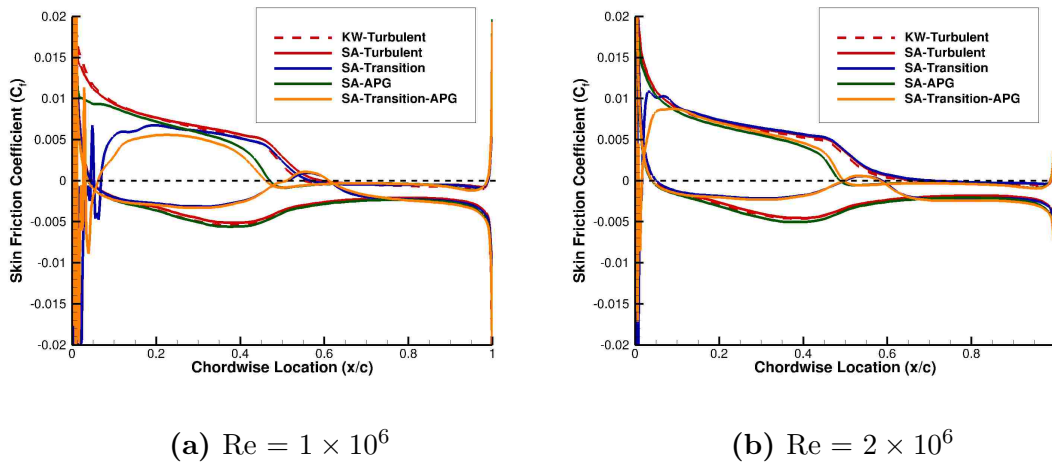**(a)** $Re = 1 \times 10^6$ **(b)** $Re = 2 \times 10^6$

Figure 3.8 – Skin friction profiles for S809 airfoil at a 13° angle of attack

drag polars also show that increasing Reynolds number decreases the C_l at which the boundary layer transitions to mostly turbulent flow, indicated by the point where C_d starts increasing.

The flow at an angle of attack of 13° was in the incipient stall region, which provides a useful comparison of different turbulence modeling options. Instanta-
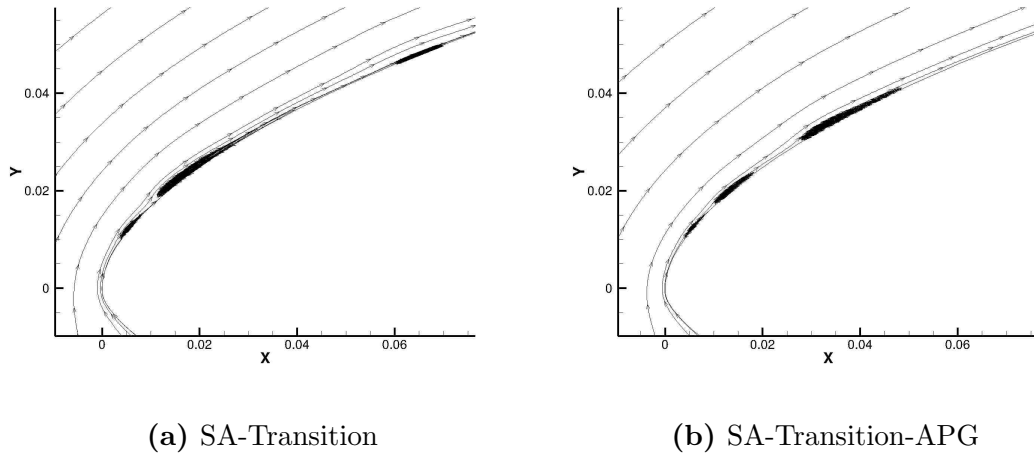
(a) SA-Transition

(b) SA-Transition-APG

Figure 3.9 – S809 leading edge streamlines at Re $= 1 \times 10^6$ and a 13° angle of attack

neous pressure distributions on the airfoil surface are plotted in Fig. 3.7 at an angle of attack of 13°. The improvement in the predicted surface pressure profile was dominated by the APG correction, which brought the predicted pressures along the upper surface significantly closer to their experimentally measured values. Skin friction profiles are plotted at an angle of attack of 13° in Fig. 3.8. The overall skin friction levels are noticeably reduced with the addition of the transition model, which was expected in regions of laminar flow. In addition, the transition location on the lower surface can be seen where the skin friction coefficient temporarily switches sign. This location corresponds to the laminar separation bubble on the lower surface seen in Figs. 3.5a and 3.5b. The oscillations in skin friction near the leading edge of the are due to a series of bubbles of reversed flow. Figures 3.9a and 3.9b shows streamlines over the airfoil at the leading edge, the series of reversed flow bubbles corresponds to the oscillations in skin friction seen in Fig. 3.8. The transition location measured by the experiments occurred below a chordwise location of 0.05,

but for angles of attack above 10° no data on the presence of laminar separation bubbles was available [8].

3.3 S827 Results

The S827 airfoil is a 21% thick airfoil intended for use on stall-regulated horizontal axis wind turbines. The airfoil is designed to maintain laminar flow over large portions of its surface. Experimental performance data is available from experimental studies by NREL [17]. Two-dimensional flow past an S827 airfoil is simulated for multiple angles of attack between 0° and 20° at a Mach number of 0.1 and Reynolds numbers of 1×10^6 and 2×10^6.

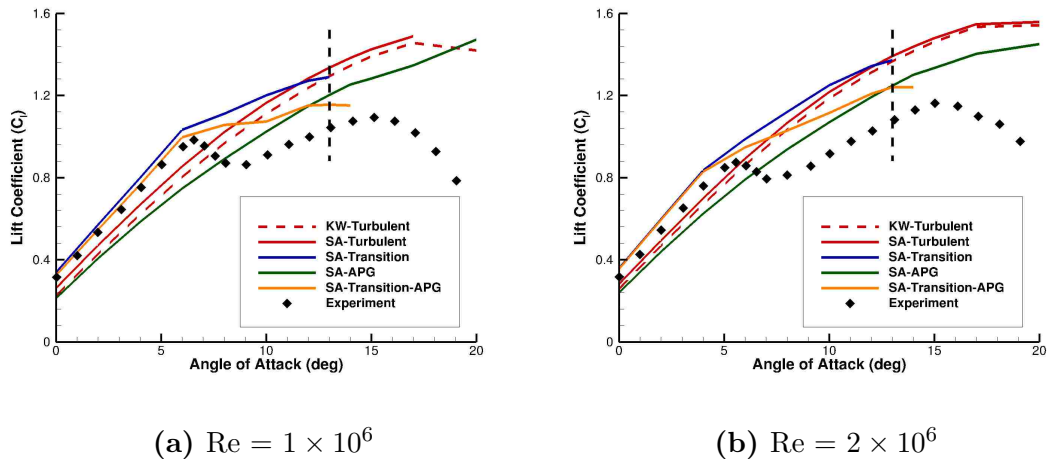(a) Re = 1×10^6 (b) Re = 2×10^6

Figure 3.10 – Comparison of lift for S827 airfoil between CFD and experimental data

The predicted lift coefficients are plotted and compared to experimental results in Fig. 3.10. The baseline SA model significantly over-predicted the angle of attack for stall onset and the maximum lift. Similar to the S809 airfoil, predicted lift
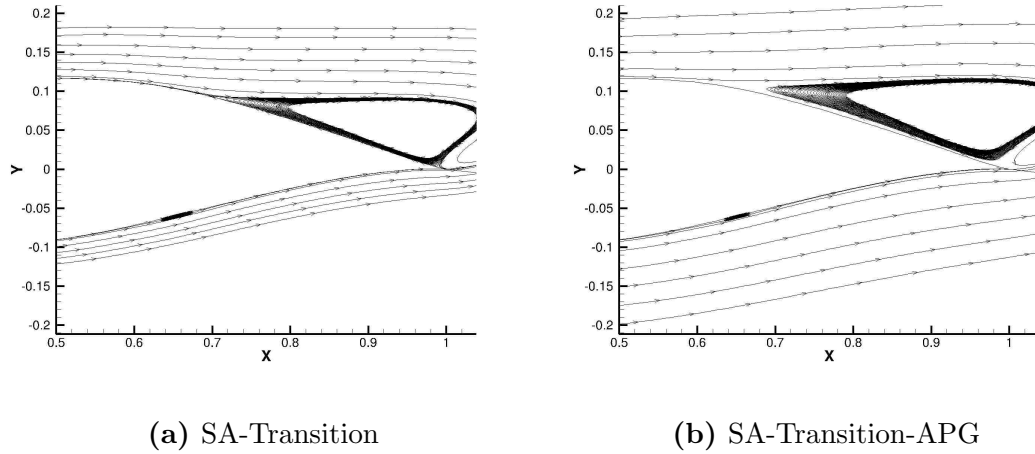
(a) SA-Transition

(b) SA-Transition-APG

Figure 3.11 – S827 streamlines at Re $= 1 \times 10^6$ and a 13° angle of attack

(a) Surface pressure profile
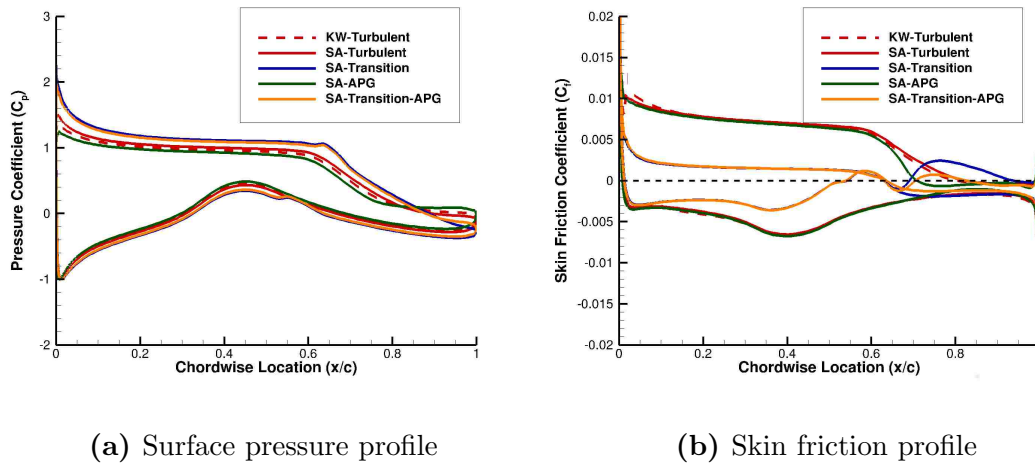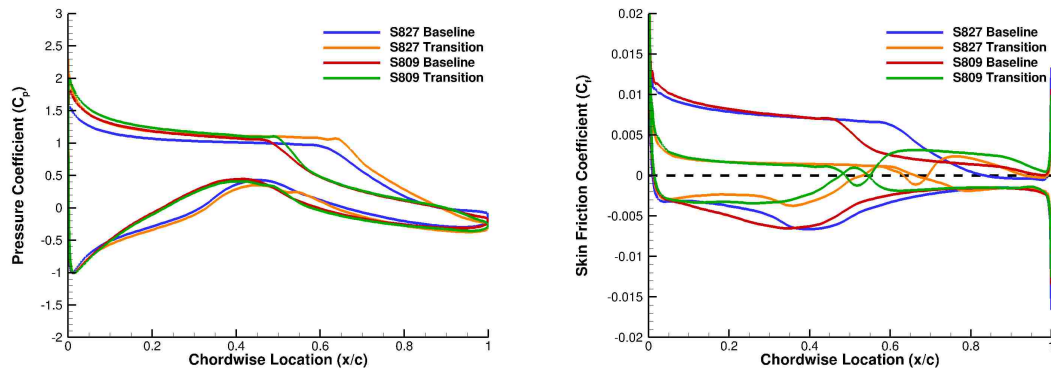
(b) Skin friction profile

Figure 3.12 – Skin friction and surface pressure profiles for S827 airfoil at a 6° angle of attack

values at angles of attack above 8° were decreased by about 13% by the addition of the APG correction, which increased the amount of predicted separation, shown by the trailing edge streamlines at a 13° angle of attack in Fig. 3.11. Below an angle of attack of 7° the baseline SA model under-predicted the lift. The addition of transition modeling was important when simulating the S827 airfoil as it increased

(a) Surface pressure profile   **(b)** Skin friction profile

Figure 3.13 – Comparison of skin friction and surface pressure profiles for the S809
and S827 airfoils at a 6° angle of attack

the predicted lift by 14% to 20%, improving the agreement of lift predictions with
experimental results at angles of attack below 7°. Figure 3.12 shows the surface
pressure profiles and the skin friction profiles for the S827 airfoil at a 6° angle of
attack, illustrating that the increased accuracy of lift predictions below a 7° angle
of attack was caused by a reduction in the surface pressure along the upper surface
between the leading edge and the 90% chord location. The surface pressure profiles
for the S827 and S809 airfoils at a 6° angle of attack are compared in Fig. 3.13
with and without transition modeling. Figure 3.13 shows that for both the S809
airfoil and S827 airfoil there was a difference in surface pressure predictions on the
upper surface upstream of the transition onset location when the baseline SA model
was compared to the SA model with transition. The primary difference was that
in the case of the S809 airfoil the difference in surface pressure profiles diminished
significantly after the transition onset while the difference in surface pressure profiles

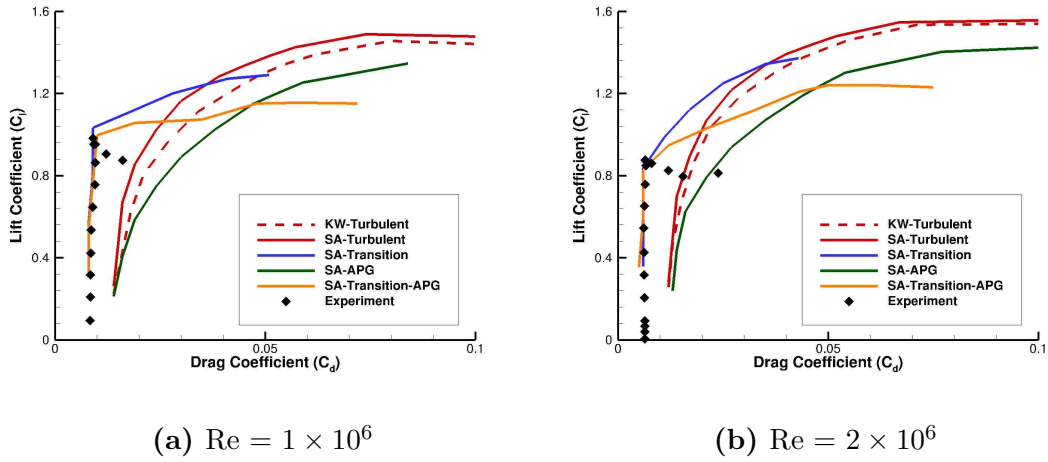continued to the 90% chord location for the S827 airfoil.

(a) Re = 1×10^6 **(b)** Re = 2×10^6

Figure 3.14 – Comparison of drag for S827 airfoil between CFD and experimental

data

(a) Re = 1×10^6 **(b)** Re = 2×10^6
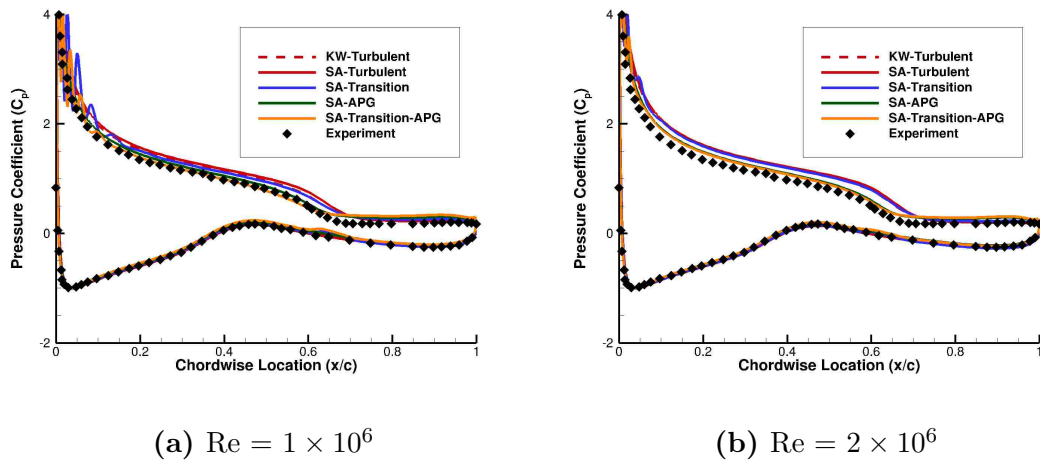
Figure 3.15 – Surface pressure profiles for S827 airfoil at a 13° angle of attack

Drag polars are plotted in Fig. 3.14, showing that adding transition modeling

decreased predicted drag by about 50%, significantly increasing the agreement of

drag predictions with experimental results at low angles of attack. The skin friction

coefficient profile at a 6° angle of attack is plotted in Fig. 3.12b, illustrating that the drag decrease was due to dramatically lower skin friction coefficients in the laminar region on the upper surface. Even utilizing transition modeling and the APG correction, it was difficult to accurately capture the first lift bucket that occurs near an angle of attack of 7°. The experimental results for the S827 illustrated the importance of transition in creating the lift bucket, which suggests that improving the transition model further should improve predictions of the lift bucket.
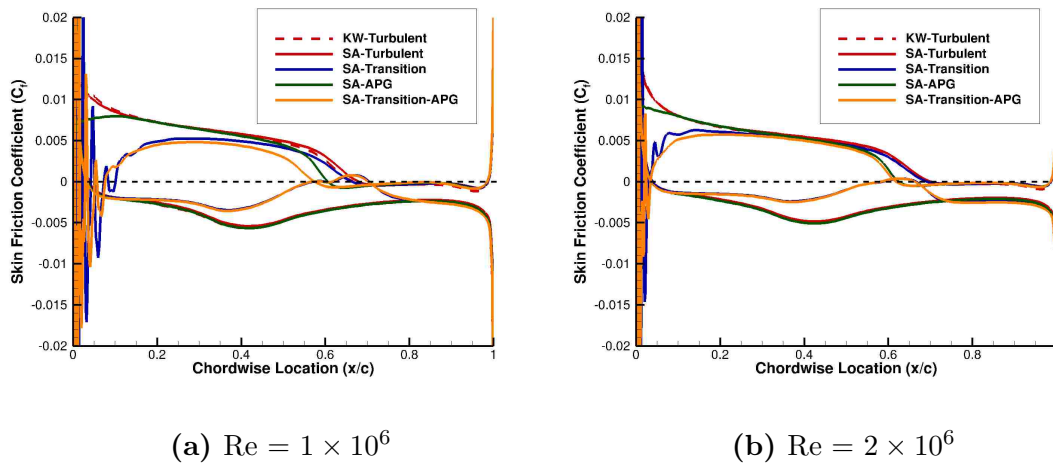

(a) Re $= 1 \times 10^6$ **(b)** Re $= 2 \times 10^6$

Figure 3.16 – Skin friction profiles for S827 airfoil at a 13° angle of attack

At angles of attack above 8° the effects of transition modeling and the APG correction on surface pressure profiles and skin friction profiles were similar to the effects seen in the S809 airfoil case. Surface pressure profiles are plotted in Fig. 3.15, which shows that the APG correction improved the pressure profile at angles of attack above 8°. The skin friction profile in Fig. 3.16 showed a reduction in overall skin friction levels for a significant portion of the blade. The presence of a laminar separation bubble on the lower surface can be seen in the skin friction plot in
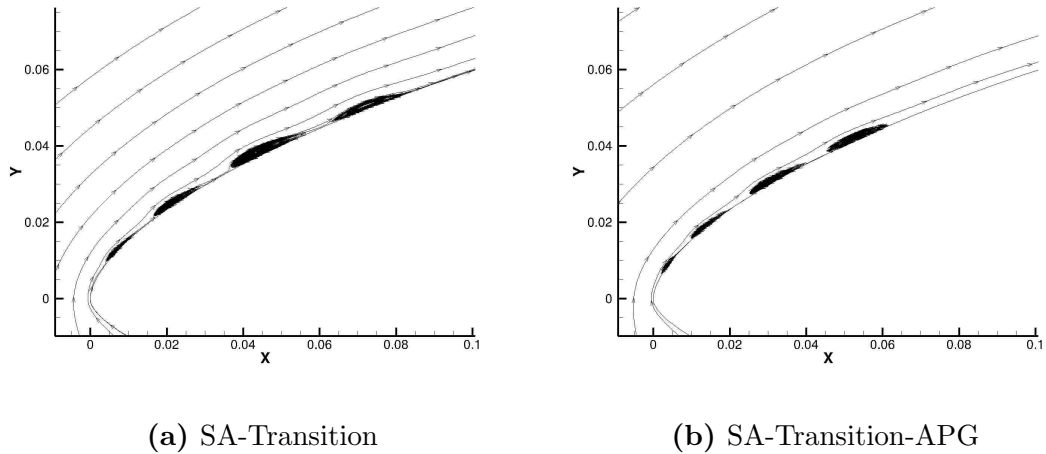
(a) SA-Transition

(b) SA-Transition-APG

Figure 3.17 – S827 leading edge streamlines at Re $= 1 \times 10^6$ and a 13° angle of

attack

Fig. 3.16, which also shows that increasing the Reynolds number decreased the size

of the laminar separation bubble. The laminar separation bubble observed in the

skin friction plot corresponds to the small separated region that can be seen with

the help of the streamlines in Fig. 3.11a and 3.11b. The oscillations in the skin

friction coefficient near the leading edge were again due to some small separated

regions, illustrated by the streamlines at the leading edge in Fig. 3.17a and 3.17b.

3.4   GPU Acceleration

This section details several modifications that were made to the GPU-RANS

solver originally developed by Thomas [31]. The transition model presented in Chap-

ter 2, Section 2.5.4.1 was implemented in the GPU solver to enable it to produce

the same results as OverTURNS for the two-dimensional airfoils. The implementa-

tion of the flux routines and reconstruction routines was modified to handle caching

data on the GPU more efficiently, resulting in a 10% to 15% speedup of the solver. The runtime of the GPU-RANS solver and OverTURNS were compared for the two-dimensional airfoils. It was found that the GPU-RANS solver was a 5 times faster than OverTURNS, completing the two-dimensional simulations in 19% of the time required by OverTURNS. In addition, extending the GPU code to full three-dimensional wind turbine rotor simulations was explored. Terms required to simulate arbitrary motion of the grid were added, which allows for the rotation required to perform the rotor simulations. Instead of overset meshes, the hybrid FVM-RANS methodology was implemented to model the wind turbine wake, the details of this implementation are presented in Appendix A.

3.5   Summary

In this chapter the S809 and S827 wind turbine airfoils were simulated to evaluate the advantages of transition modeling and the APG correction when applied to wind turbine airfoil simulations. The baseline SA model over-predicted drag at low angles of attack and at high angles of attack it over-predicted the stall onset angle and maximum lift. Applying the transition model brought drag predictions at lower angles of attack into line with the experimental data. Including the APG correction decreased the maximum predicted lift and the predicted stall angle of attack, bringing the simulation predictions closer to the experimentally determined values. The next chapter presents the results from three dimensional simulations of the Sandia 100 m blade.

Chapter 4: Sandia 100 m Blade Computational Simulations

In this chapter, simulation results from the Sandia 100 m wind turbine blade are presented. The effects of adding transition modeling and DDES were investigated at several wind speeds. Results obtained using both transition modeling and DDES were compared to results from Corson et al. [53] for the full range of wind speeds between 6.0 ms⁻¹ and 17.0 ms⁻¹.

4.1   Computational Grids

These simulations utilized an overset mesh system consisting of a C-O topology blade mesh and a cylindrical wake mesh, as shown in Fig. 4.1. The implicit hole cutting method described in Chapter 2 (Section 2.5.8) was used to pass information between the different overset meshes. The computational expense was significantly reduced by taking advantage of the rotational periodicity of the 3-bladed rotor and modeling only one blade and the corresponding third (120°) of the wake cylinder and using periodic boundary conditions.
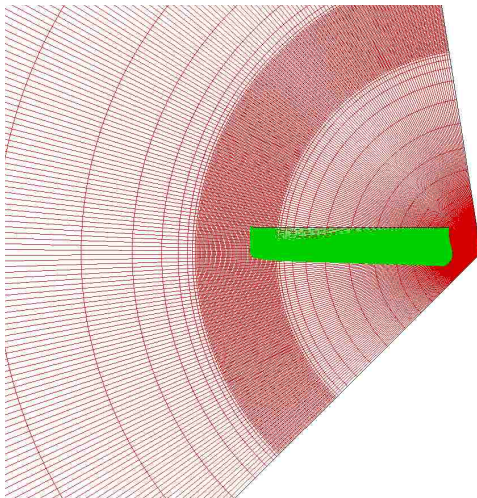
The background mesh extended from 0.03 rotor radii (R) to $3.5R$ in the radial direction and from $3.0R$ above the rotor to $8.0R$ below the rotor in the axial direction. The background mesh dimensions were $184 \times 104 \times 160$ in the azimuthal, radial,
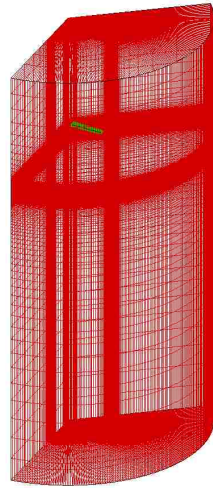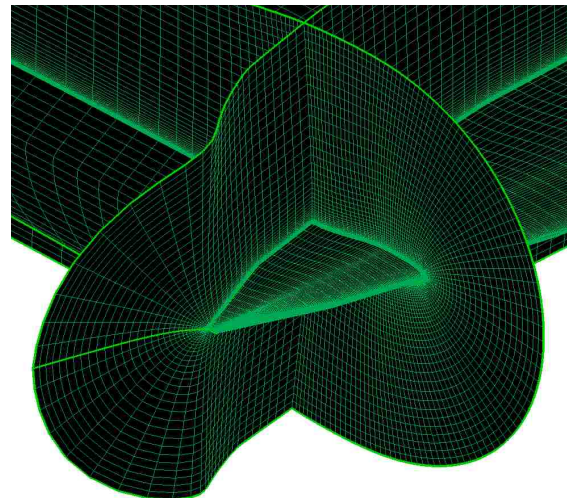
(a) Cylindrical wake mesh
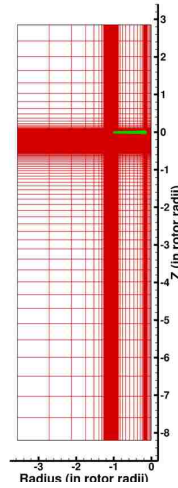
(b) Side view

(c) Top view

(d) C-O blade mesh

Figure 4.1 – Sandia 100 m blade overset mesh system with the blade mesh in green and background mesh in red

and axial directions, respectively. Points in the background mesh were clustered to provide a high mesh resolution (with a radial spacing of 0.05 root chord lengths) in the radial regions where the tip and root vortices convect. In the axial region near the blade, points were clustered to provide an axial spacing of 0.1 root chord
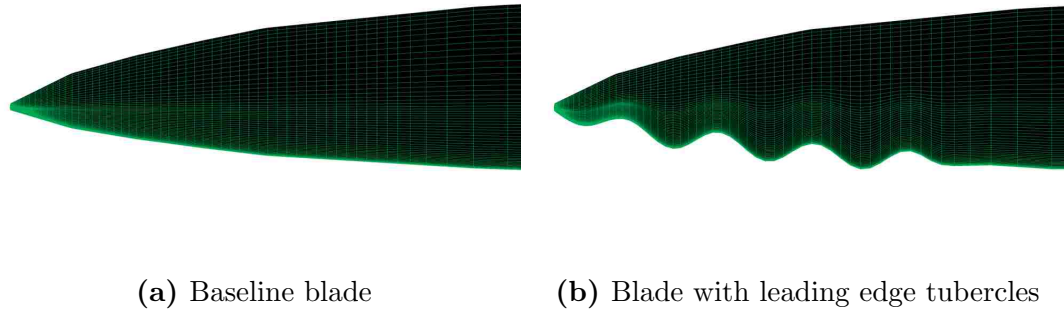
(a) Baseline blade   **(b)** Blade with leading edge tubercles

Figure 4.2 – Comparison of outer 10% of the blade surface with and without leading edge tubercles

lengths between $0.1R$ and $0.5R$ above and below the blade, respectively. The mesh utilized for the simulations with leading edge tubercles has the same dimensions as the baseline blade mesh, the only difference is a modification of the blade surface to add tubercles to the outer 10% of the blade. The resulting mesh at the surface of the blade tip is shown in Fig. 4.2 with the baseline blade for comparison.

The blade mesh is a structured, body-fitted C-O mesh. The dimensions are $171 \times 101 \times 75$ in the wrap-around, spanwise, and wall-normal direction, respectively. There are 100 points along the airfoil surface in the wrap-around direction. The wake cut extends approximately 1 root chord lengths downstream. The outer boundary in the wall-normal direction is about 1 root chord lengths from the surface. The wall-normal spacing at the blade surface is chosen to ensure a $y+$ value under 1.0.

4.2 Wake Capturing Results

The simulations were performed for a range of wind speeds between 6.0 ms^{-1} and 17.0 ms^{-1}. The wind speeds simulated as well as the associated rotor RPM and blade pitch are given in Table 4.1. The associated tip Mach numbers range from 0.1361 to 0.2332 and the tip Reynolds numbers range from 3.093×10^6 to 5.301×10^6.

Wind Speed (ms^{-1})	Rotor Speed (RPM)	Collective Pitch (degrees)
6.0	5.650	0.0
7.0	6.590	0.0
8.0	6.933	0.0
9.0	7.036	0.0
10.0	7.157	0.0
11.0	7.291	0.0
11.3	7.401	0.0
12.0	7.438	3.231
13.0	7.438	6.166
15.0	7.438	10.12
17.0	7.438	13.26

Table 4.1 – Operating points used for simulations

All cases were executed until the thrust and power varied less than 0.2% during a revolution. The number of revolutions required for convergence changed depending on the wind speed, ranging from 20 revolutions for low wind speed cases to 8 revolutions for the high wind speed cases. The additional revolutions for low wind speed cases were required to allow the transients in the wake to convect downstream and become fully developed.

4.2.1 Wind Turbine Performance Comparison

The rigid blade results produced by Corson et al. [53] are used as a reference for the predicted wind turbine performance. Corson et al. utilized *AcuSolve*, which is a flow solver based on the Galerkin/Least-Squares finite element method. The flow was assumed to be incompressible due to the low Mach numbers involved. The SA model was used for turbulence modeling and the rigid blade simulations did not utilize transition modeling or DDES.

OverTURNS was run with and without transition modeling and DDES to determine their effect on the predicted performance values for three cases spanning the range of wind speeds. The predicted thrust and power, shown in Table 4.2, show that including transition modeling and DDES increased the predicted thrust by 2% to 4% and increased the predicted power by 4% to 7%. The spanwise airloads both in-plane and out-of-plane are shown in Fig. 4.3 along with airloads calculated by Corson et al. [53] using AcuSolve, as a reference. The addition of transition modeling and DDES increased both in-plane and out-of-plane loadings, but the effect was more pronounced for the in-plane load distribution, as shown in Fig. 4.3. The other wind speeds investigated showed a similar pattern. The predicted in-plane load distribution was not as smooth as the values given by Corson et al., shown in Fig. 4.3, this was due in part to the coarseness of the mesh on the inner two-thirds of the blade.

The effect of leading edge tubercles on the performance was investigated. Only three of the cases were used for this comparison in order to investigate the effect

Wind Speed (ms⁻¹)	Turbulence Modeling	Thrust (kN)	Power (MW)
6.0	SA	609.7	2.063
6.0	SA-Transition-DDES	623.8 (+2.29%)	2.220 (+7.33%)
11.3	SA	1738	13.44
11.3	SA-Transition-DDES	1777 (+2.18%)	13.93 (+3.58%)
15.0	SA	969.5	12.13
15.0	SA-Transition-DDES	1004 (+3.51%)	12.83 (+5.61%)

Table 4.2 – Comparison of OverTURNS predicted performance with different turbulence modeling options

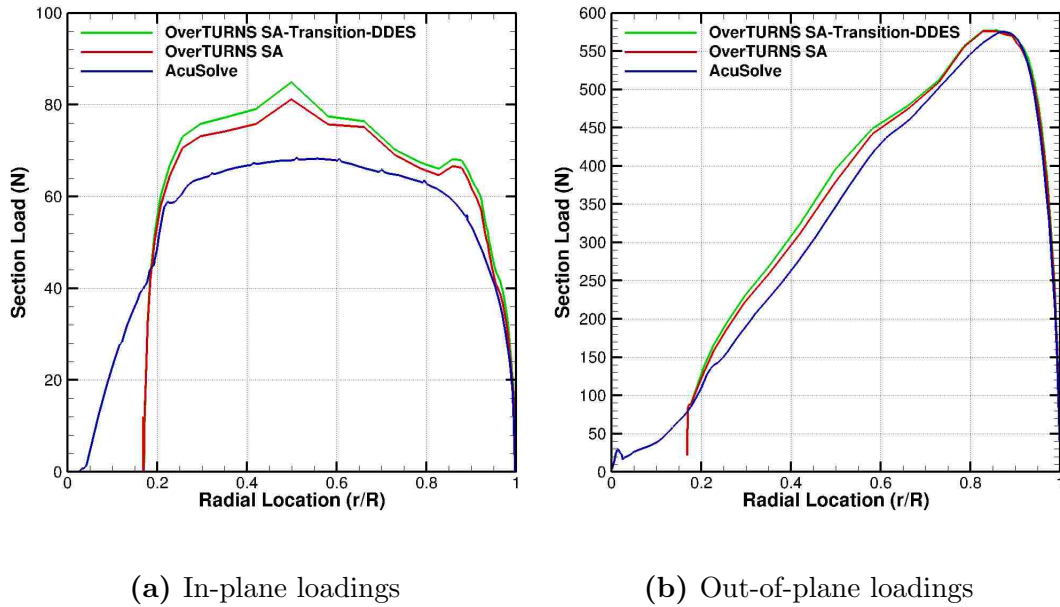**(a)** In-plane loadings

(b) Out-of-plane loadings

Figure 4.3 – Comparison of in-plane and out-of-plane sectional airloads at an 11.3 ms⁻¹ wind speed for OverTURNS and AcuSolve results

of tubercles for a representative set of wind speeds without requiring a full sweep of wind speed. Both transition modeling and DDES were enabled for these cases. Table 4.3 shows that the tubercles had a minimal effect on the performance values, decreasing thrust and power by less than 1% in all three cases. The spanwise airload distributions, shown for an 11.3 ms⁻¹ wind speed in Fig. 4.4, reflect this effect, with
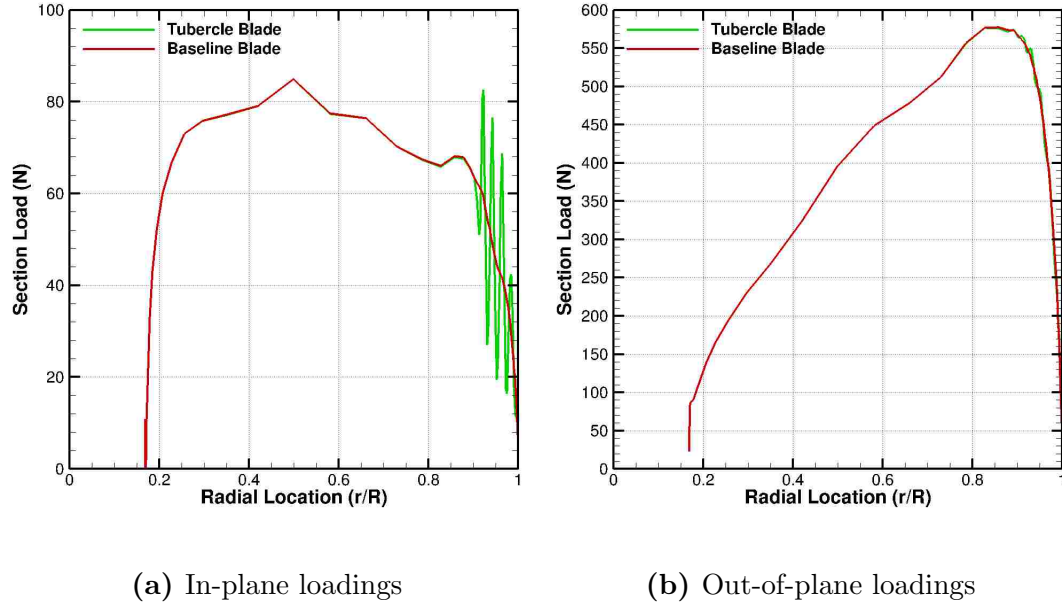
(a) In-plane loadings   **(b)** Out-of-plane loadings

Figure 4.4 – Comparison of in-plane and out-of-plane sectional airloads at an 11.3 ms^{-1} wind speed for OverTURNS for the baseline blade and the blade with leading edge tubercles

very little difference except in the immediate vicinity of the tubercles, a pattern that was also seen in the other wind speeds investigated. A comparison of the spanwise loadings for the outer 15% of the blade is shown in Fig. 4.5. The addition of tubercles primarily affected the in-plane airload distribution by introducing large oscillations in the sectional airloads near the tip. The oscillations were due to pressure differences along the leading edge on the upwind side, with the surface pressure significantly higher at tubercle crests compared to pressures in the tubercle troughs.

The performance predictions of OverTURNS and AcuSolve are shown in Fig. 4.6. Both OverTURNS and Acusolve showed the proper trend of increasing power in the speed controlled region (3.0 ms^{-1} to 11.3 ms^{-1}). In the pitch controlled region (above 11.3 ms^{-1}) there was a slight drop in power, this occurs because the blade pitches

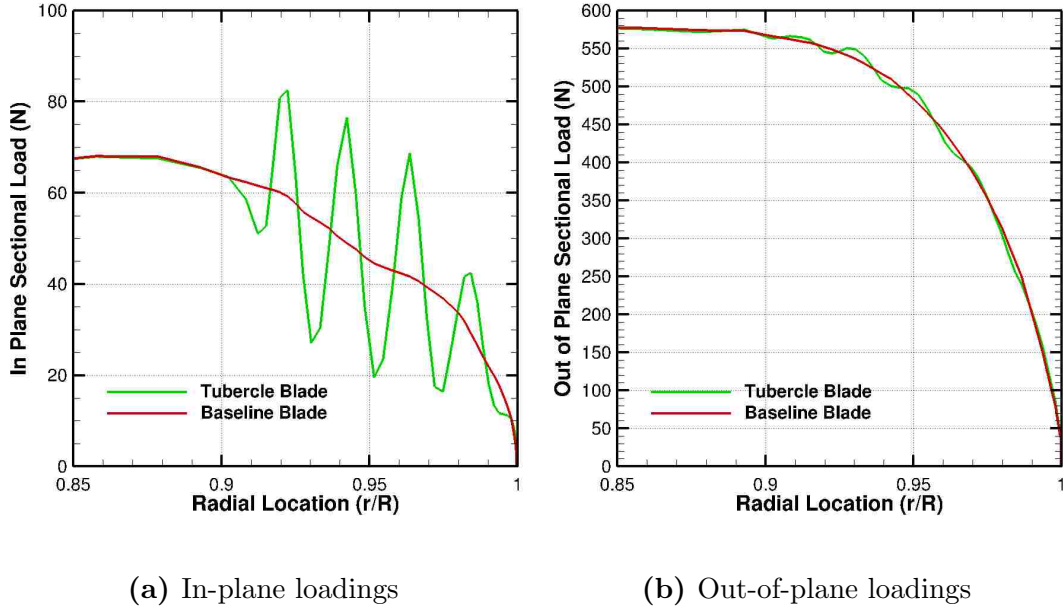**(a)** In-plane loadings

(b) Out-of-plane loadings

Figure 4.5 – Comparison of in-plane and out-of-plane sectional airloads at an
11.3 ms^{-1} wind speed on the outer 15% of the blade for OverTURNS
for the baseline blade and the blade with leading edge tubercles

Wind Speed (ms^{-1})	Blade	Thrust (kN)	Power (MW)
6.0	Baseline	623.8	2.220
6.0	Tubercles	623.6 (-0.03%)	2.204 (-0.73%)
11.3	Baseline	1777	13.93
11.3	Tubercles	1776 (-0.06%)	13.88 (-0.37%)
15.0	Baseline	1004	12.83
15.0	Tubercles	1001 (-0.30%)	12.76 (-0.54%)

Table 4.3 – Comparison of blade with and without leading edge tubercles using Over-
TURNS with transition modeling and DDES

were calculated by FAST to generate constant power in that region, shown by the

constant power that FAST maintains. The drop can be attributed to the CFD

solvers capturing losses that were not captured by the simplified aerodynamic model

in FAST. To maintain constant power in the pitch controlled region the collective
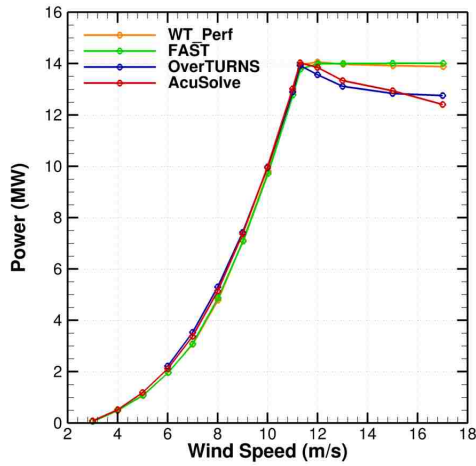
(a) Rotor power
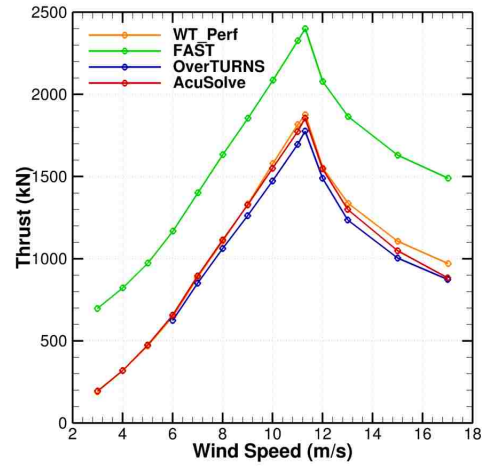
(b) Rotor thrust

Figure 4.6 – Performance comparison of OverTURNS, AcuSolve, WT_perf, and

FAST results

was lowered as wind speed increased to maintain constant power, this lowered the

angle of attack of the blade and led to lower thrust levels in the pitch controlled

region. OverTURNS consistently predicted thrust values 4% to 5% lower than the

AcuSolve results. The predicted power was generally within 3% of the AcuSolve

results, except at 6.0 ms^{-1} and 7.0 ms^{-1} where the predicted power was 5% higher

than the AcuSolve results. A transition model was not used in the AcuSolve simu-

lations, as such the consistently lower predicted thrust values can be attributed at

least partly to the inclusion of transition modeling in OverTURNS.

4.2.2 Flow Field

This section will take a more detailed look at the flow fields generated by OverTURNS. First, the effects of improved turbulence modeling on the wake geometry are detailed. Second, the consequences of adding leading edge tubercles are investigated.

4.2.2.1 Turbulence Modeling Comparison

The effects on the flow field due to the addition of transition modeling and DDES are investigated in this section. The comparisons focus on a single case, the 6.0 ms^{-1} wind speed case, because the effects were essentially the same for the other two wind speeds where the comparisons were made, 11.3 ms^{-1} and 15.0 ms^{-1}.

Simulated oil flows and intermittency plots were used to evaluate the effect of adding the transition model. The simulated oil flows were generated by plotting streamlines on a surface that was two computational cells away from the wall. Figure 4.7 shows the simulated oil flow at a wind speed of 6.0 ms^{-1}, showing that there was a significant region of separated flow on the upwind surface of the blade. The addition of the transition model did not significantly affect the extent of separated flow near the root on the upwind side. Based on the two dimensional airfoil simulations in Section 3.2 of Chapter 3, this outcome was expected since the transition model did not significantly affect the predicted stall angle. The intermittency plot shown in Fig. 4.8 shows that there were significant amounts of laminar flow near the root and in the outer 10% of the blade radius.
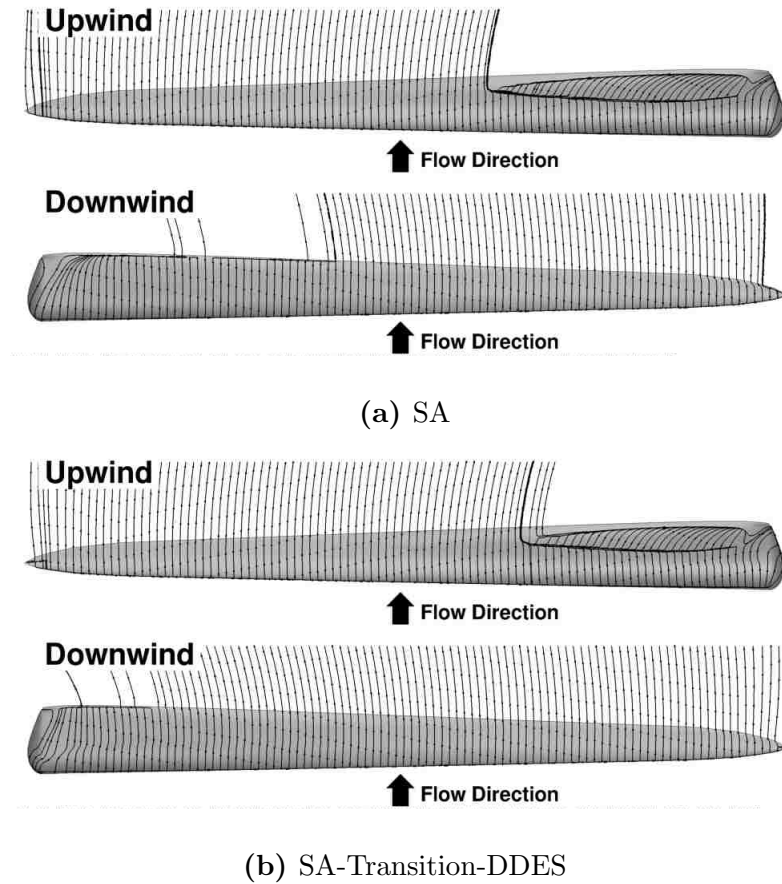
(a) SA

(b) SA-Transition-DDES

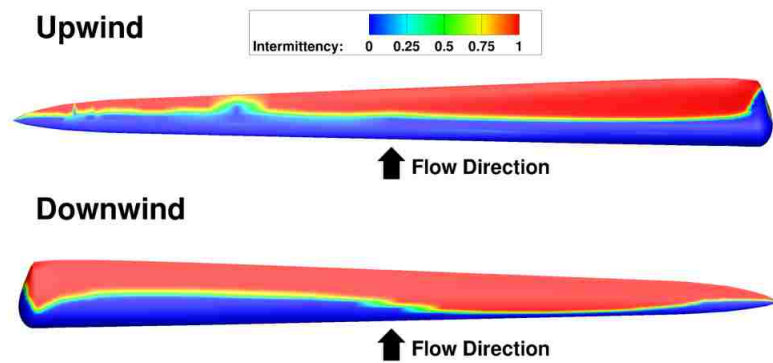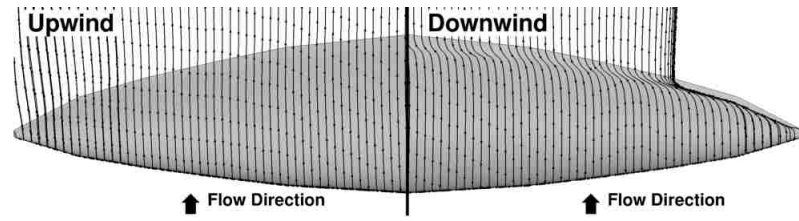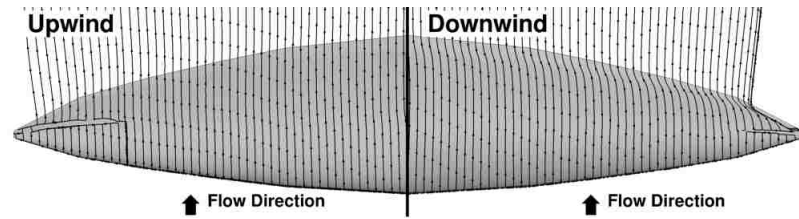**Figure 4.7** – Simulated oil flow on the blade surface at 6.0 ms^{-1} wind speed

Figure 4.8 – Intermittency on the blade surface at 6.0 ms^{-1} wind speed

Focusing on the tip region, it be can seen in Fig. 4.9 that including the transition model allowed the laminar separation bubble near the tip to be captured. The

(a) SA

(b) SA-Transition-DDES

Figure 4.9 – Simulated oil flow at the blade tip at 6.0 ms^{-1} wind speed, highlighting the laminar separation bubble (LSB)
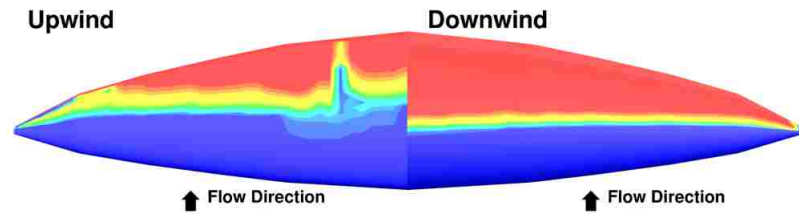

Figure 4.10 – Intermittency at the blade tip at 6.0 ms^{-1} wind speed

location of the laminar separation bubble is reflected in the intermittency plot in Fig. 4.10 where the laminar to turbulent transition occurs at the same location. The laminar separation bubble did not extend along the entire transition region.

The addition of DDES primarily affected the tip and root vortex. Comparing the eddy viscosity contours at the blade tip shown in Fig. 4.11, it is observed that the addition of DDES significantly lowered eddy viscosity levels in the resulting tip vortex. On the other hand, vorticity levels at both the root and tip were similar
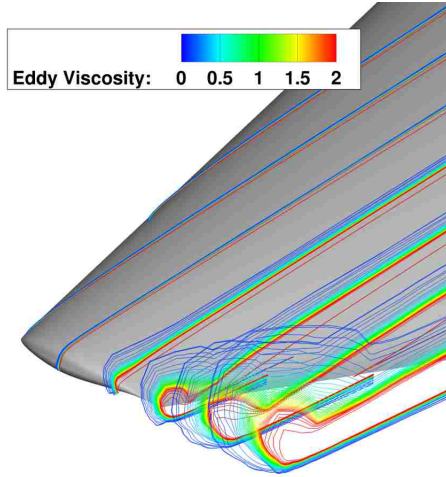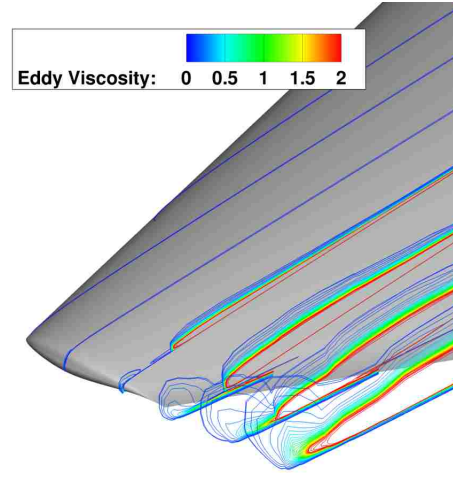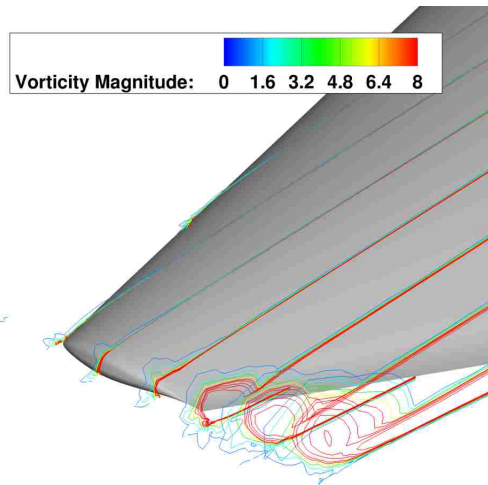
(a) SA   **(b)** SA-Transition-DDES

Figure 4.11 – Blade tip eddy viscosity contours at 6.0 ms^{-1} wind speed

(a) SA   **(b)** SA-Transition-DDES

Figure 4.12 – Blade tip vorticity contours at 6.0 ms^{-1} wind speed

whether or not DDES was enabled. Figure 4.12 shows contours of vorticity magnitude at the blade tip. Enabling DDES primarily affected the dissipation of the tip vortex, allowing it to convect with less dissipation by lowering modeled turbulence

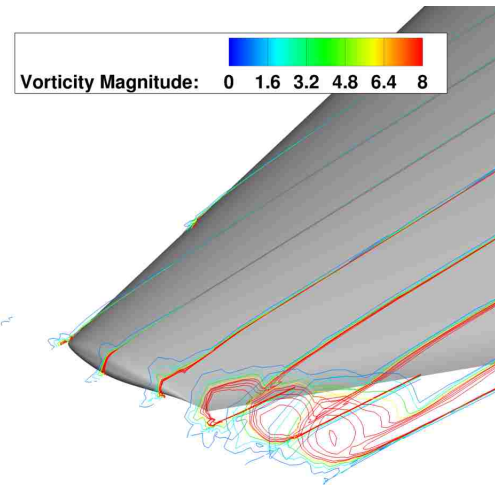**(a)** SA   **(b)** SA-Transition-DDES
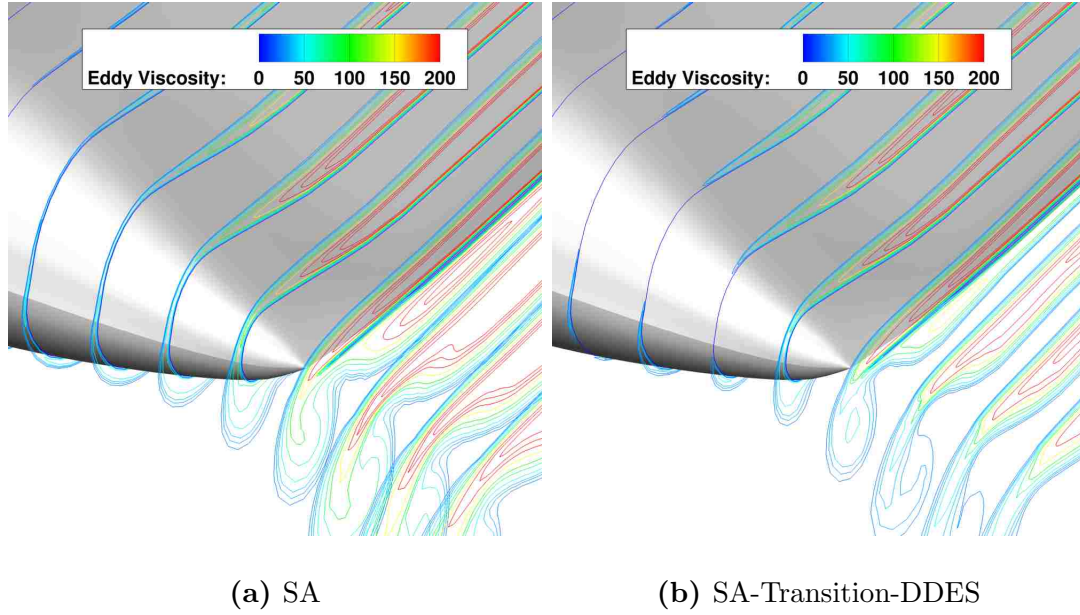
Figure 4.13 – Blade root eddy viscosity contours at 6.0 ms^{-1} wind speed

(a) SA   **(b)** SA-Transition-DDES
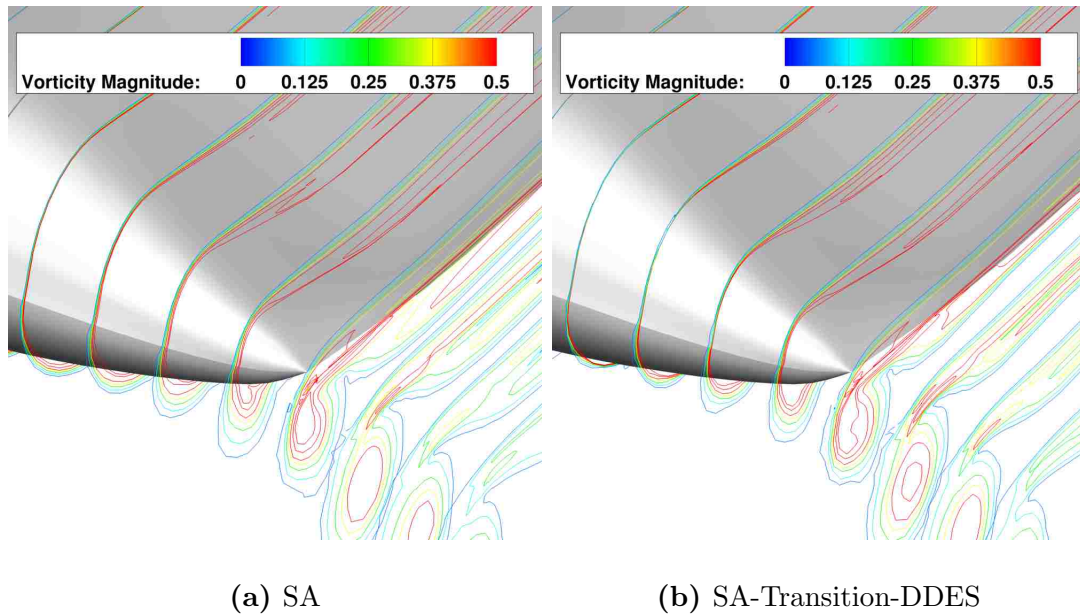
Figure 4.14 – Blade root vorticity contours at 6.0 ms^{-1} wind speed

levels. Figure 4.13 shows the eddy viscosity levels at the root of the blade and illustrates that enabling DDES drastically lowered eddy viscosity levels in the root vortex. The reduction in eddy viscosity increased the vorticity in the root vortex,

which is shown by the vorticity magnitude contours in Fig. 4.14.

Figure 4.15 – Wake structure at a wind speed of 6.0 ms⁻¹, shown by a vorticity magnitude iso-surface colored by non-dimensional pressure

(a) SA   (b) SA-Transition-DDES

Figure 4.16 – Eddy viscosity contours 35.8° behind blade at 6.0 ms⁻¹ wind speed

(a) SA　　　　　　　　**(b)** SA-Transition-DDES

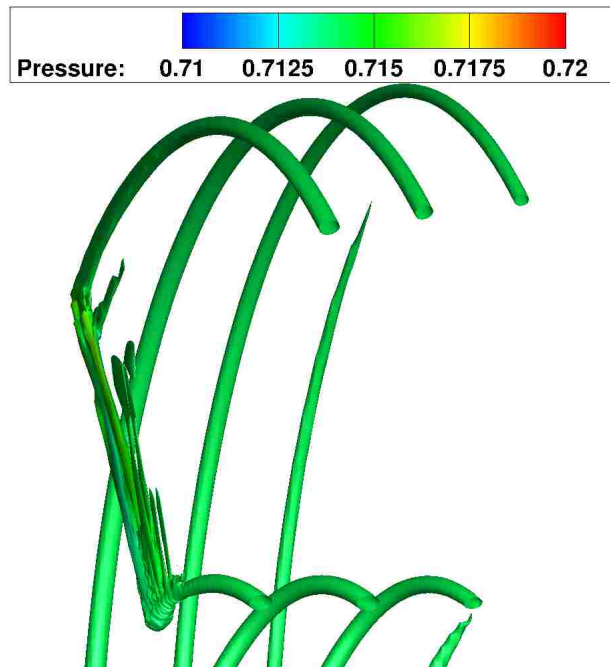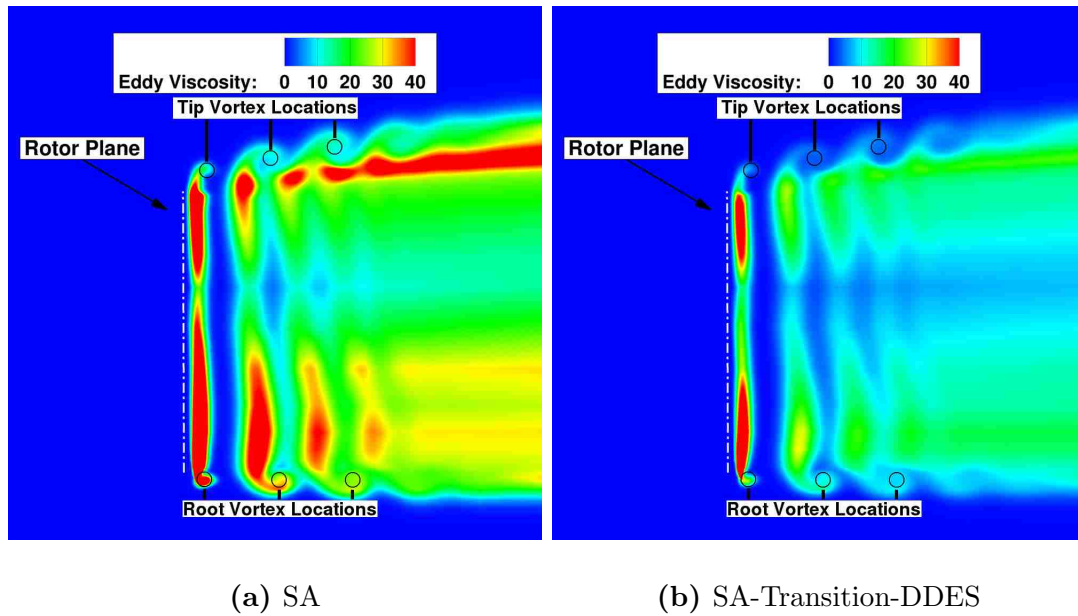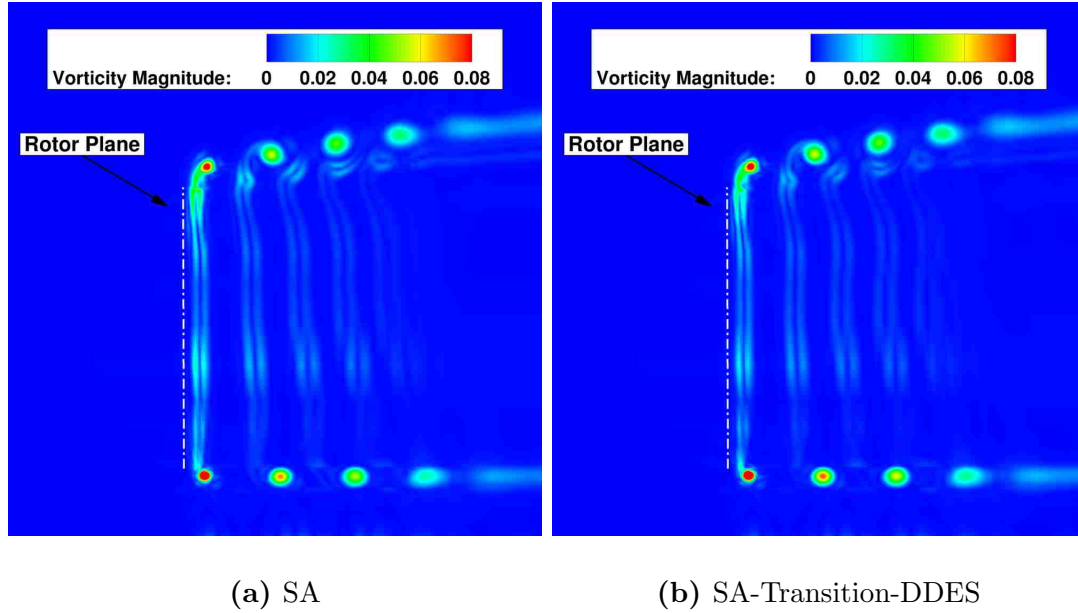**Figure 4.17** – Vorticity contours 35.8° behind blade at 6.0 ms⁻¹ wind speed

The helical wake structure generated using the SA model with transition modeling and DDES is shown in Fig. 4.15. To compare wakes generated with the baseline SA model and with the SA model using the transition model and DDES, eddy viscosity contours are shown in Fig. 4.16 for a slice of the flow field 35.8° behind the blade. As expected the addition of DDES modeling decreased the eddy viscosity in the wake of the blade. While higher eddy viscosity levels were still maintained in the region directly downstream of the separated flow, Fig. 4.16 shows that the tip vortex and root vortex experienced reduced levels of eddy viscosity, particularly near their core regions. Figure 4.17 shows vorticity magnitude contours for a slice of the flow field 35.8° behind the blade, illustrating that both the root and tip vortices experience less dissipation due to modeled turbulence.

4.2.2.2   Tubercle Effects

The performance values predicted for the blade with leading edge tubercles only differed slightly from the baseline blade, so it was expected that the flow fields will not be drastically different. Once again, the analysis is focused on the 6.0 ms^{-1} case because the 11.3 ms^{-1} and 15.0 ms^{-1} cases show the same effects.

Figure 4.18 – Simulated oil flow on the tubercle blade surface at 6.0 ms^{-1} wind speed

Figure 4.19 – Intermittency on the tubercle blade surface at 6.0 ms^{-1} wind speed

As expected, comparing the simulated oil flow on the blade with tubercles in Fig. 4.18 to the baseline blade in Fig. 4.7 shows that tubercles did not significantly affect the flow inboard along the blade. Similarly the transition location, shown by

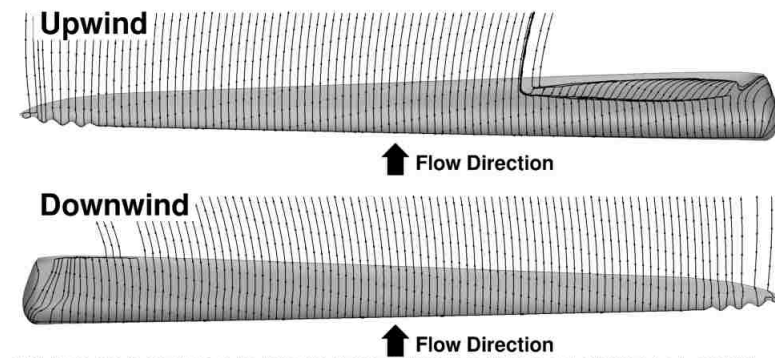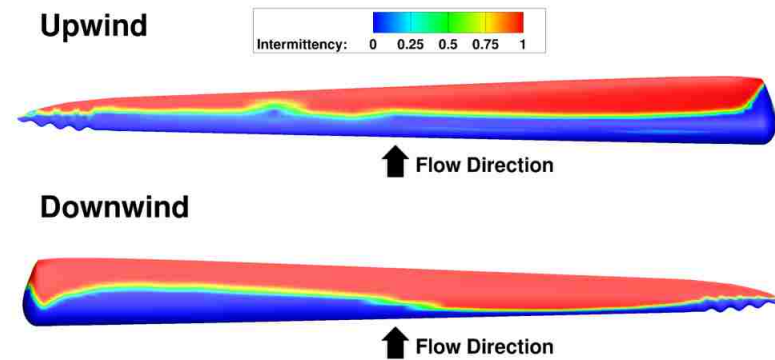the intermittency plot in Fig. 4.19, was only affected in the vicinity of the tubercles.
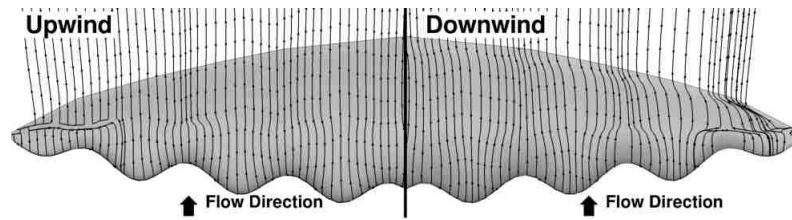
Figure 4.20 – Simulated oil flow at the tubercle blade tip at 6.0 ms^{-1} wind speed
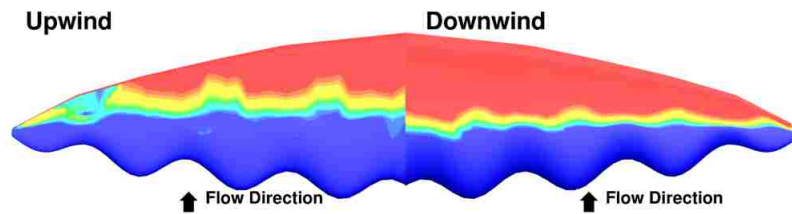
Figure 4.21 – Intermittency at the tubercle blade tip at 6.0 ms^{-1} wind speed

Figure 4.20 focuses on the simulated oil flow at the blade tip, showing that the location of the laminar separation bubble with respect to the local chord changed with the same wavelength as the tubercles. The change in the laminar separation bubble location was reflected in the intermittency plots in Fig. 4.21. These results were even more clear for the 11.3 ms^{-1} wind speed case. On the upwind surface, the changes in the location of the laminar separation bubble can be seen more clearly in Fig. 4.22, which shows the simulated oil flow as well as velocity magnitude contours. The laminar separation bubbles were larger behind the tubercle troughs, possibly due to higher pressure gradients in those locations.

On the downwind surface the transition location varied in sync with the variation in leading edge location. This can be seen in the intermittency plot in Fig. 4.23
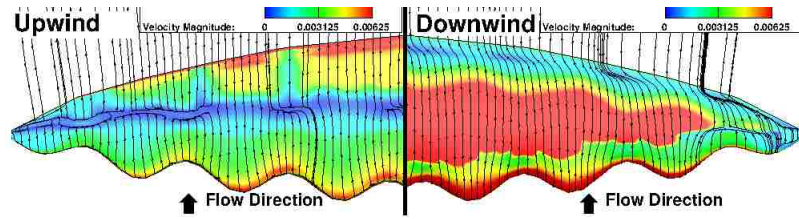
Figure 4.22 – Simulated oil flow and velocity magnitude at the tubercle blade tip at
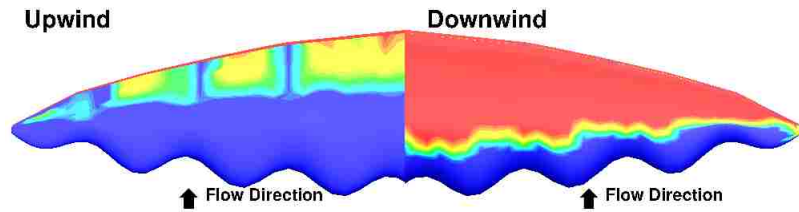
11.3 ms^{-1} wind speed

Figure 4.23 – Intermittency at the tubercle blade tip at 11.3 ms^{-1} wind speed
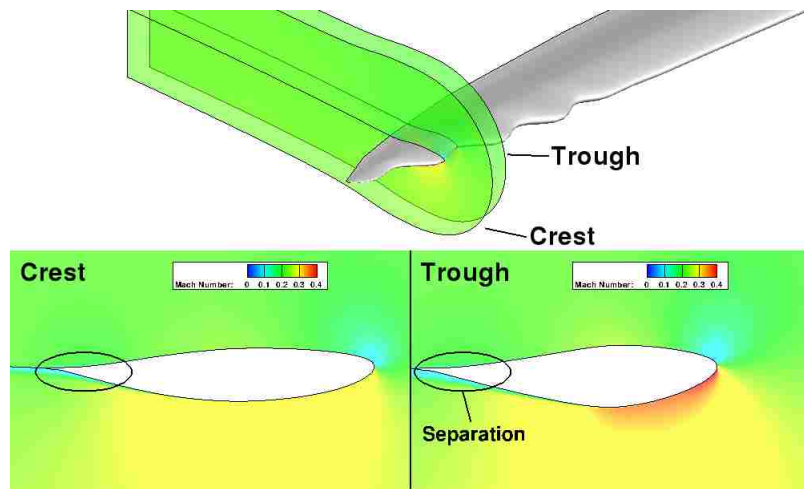
Figure 4.24 – Comparison of Mach number at tubercle crest and trough at 11.3 ms^{-1}

wind speed

and also in the velocity magnitude contours in Fig. 4.22, where the sharp increase

in near wall velocity occured due to the start of the turbulent boundary layer. Fig-

ure 4.24 compares Mach number contours for two slices, one at a tubercle crest and

one at a tubercle trough. The tubercles funnelled the flow, leading to significantly

higher velocities in the tubercle troughs, shown in Fig. 4.24. The higher velocities led to lower surface pressures in the tubercle troughs and areas of incipient separation at the trailing edge, which can be seen as small pockets of low surface velocity.

(a) Baseline   **(b)** Tubercle
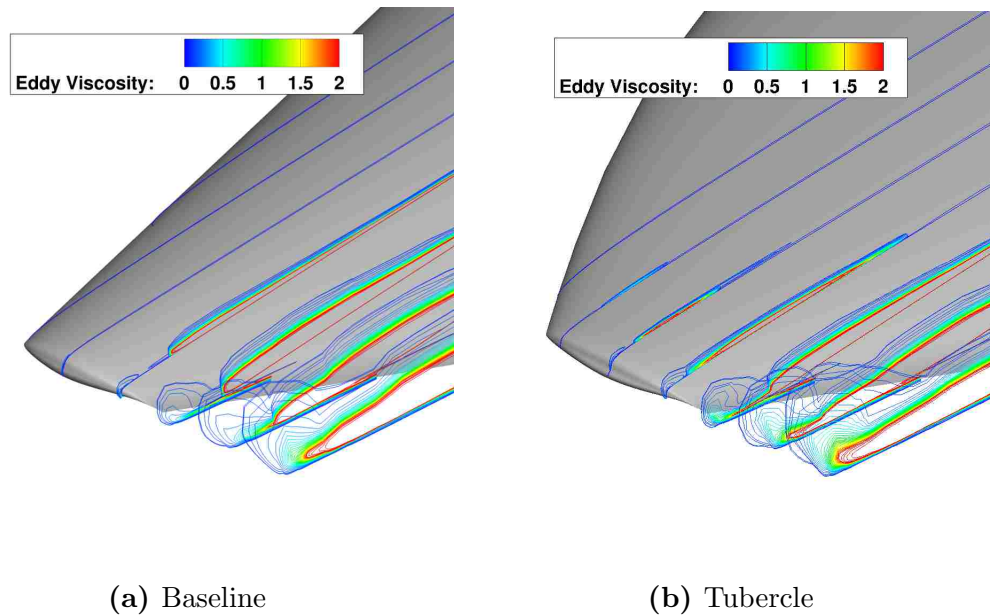
Figure 4.25 – Blade tip eddy viscosity contours at 6.0 ms^{-1} wind speed

Looking at the tip vortex formation, it can be seen in Fig. 4.25 that eddy viscosity levels are slightly increased by the presence of tubercles. Similarly, Fig. 4.26 shows that vorticity levels are also slightly higher when the blade includes leading edge tubercles. However, when comparing the both the eddy viscosity and the vorticity in the wake, shown in Figs. 4.27 and 4.28 respectively, it is apparent that the small differences near the tip did not cause significant changes to the wake structure.

(a) Baseline

(b) Tubercle
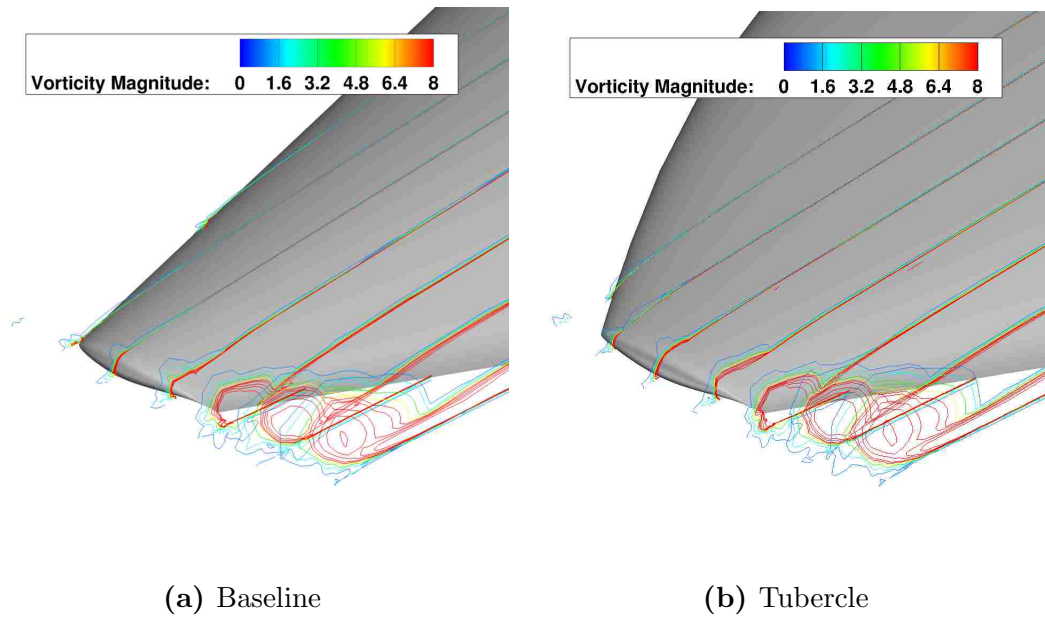
Figure 4.26 – Blade tip vorticity contours at 6.0 ms^{-1} wind speed

(a) Baseline

(b) Tubercle
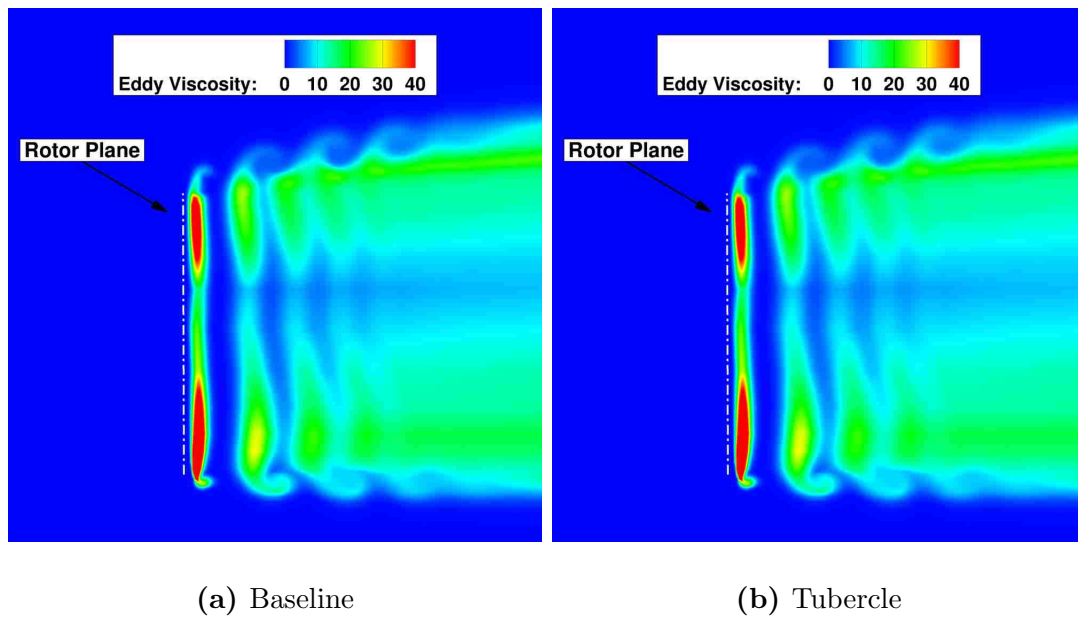
Figure 4.27 – Eddy viscosity contours 35.8° behind blade at 6.0 ms^{-1} wind speed

(a) Baseline   **(b)** Tubercle
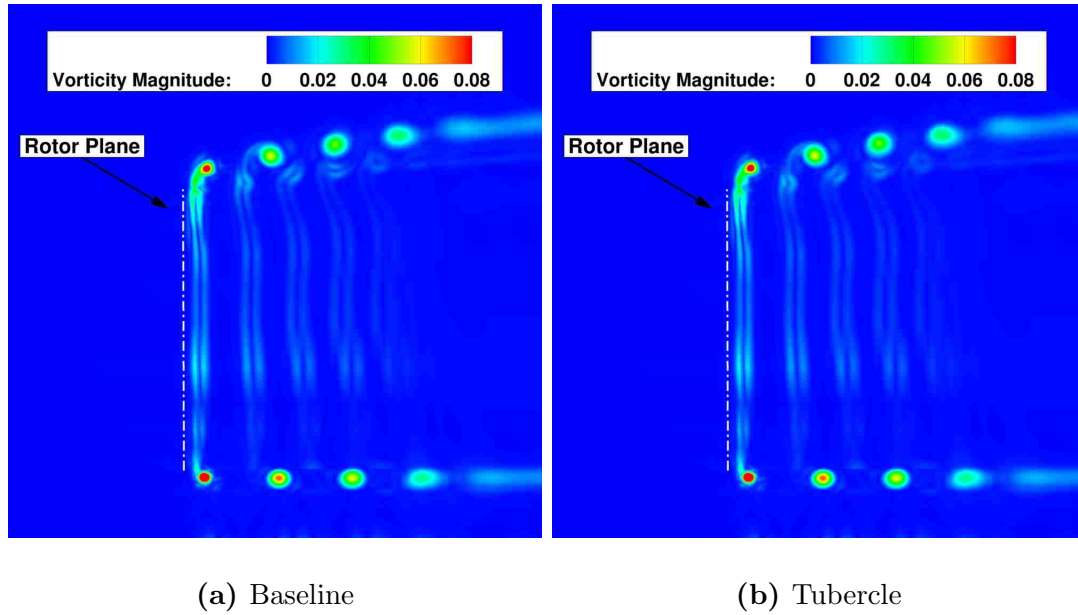
Figure 4.28 – Vorticity contours 35.8° behind blade at 6.0 ms^{-1} wind speed

4.3 Summary

In this chapter the Sandia 100 m blade was simulated to evaluate the effect of transition modeling and DDES modeling on the predicted performance values. The addition of transition and DDES modeling increased both the predicted torque and predicted power. The predicted performance matched well with the performance predicted by Corson et al. using AcuSolve [53]. The addition of DDES modeling lowered the amount of dissipation experienced by tip vortices, improving predictions of vortex strength in the wake. The effect of adding tubercles was investigated at several wind speeds. It was observed that tubercles have a very slight performance penalty at normal operating conditions. The performance penalty was small because tubercles primarily affect flow in the post-stall region, but pitch-controlled turbines are designed to operate below the stall angle of attack.

Chapter 5:   Conclusions

5.1   Summary

The drive to reduce wind energy generation costs has led to a constant drive for increased wind turbine sizes. The large scale of modern wind turbines make full scale experimental tests challenging using current facilities, which has significantly increased the importance of computational simulations. In the past simplified aerodynamic models have been widely used in conjunction with structural models as a relatively quick way to evaluate wind turbine performance. However, the higher aerodynamic loads on the blade and its increased flexibility has led to wind turbine operating conditions outside the range where these simplified aeroelastic models are valid. An alternative is the use of three-dimensional CFD simulations to accurately evaluate wind turbine performance for realistic operating conditions.

The present work evaluates the use of CFD simulations for both two-dimensional wind turbine airfoil simulations and three-dimensional wind turbine rotor simulations. Specifically, the effects of including transition modeling and other improvements to turbulence modeling were investigated for both two-dimensional and three-dimensional simulations. The S809 and S827 wind turbine airfoils were simulated and validated against experimental results produced by NREL. The Sandia $100\,\mathrm{m}$

blade was simulated and the performance and flow predictions were compared to previous experimental and numerical works. A preliminary evaluation of the effects of leading edge tubercles on the Sandia 100 m blade was performed for its nominal operating conditions.

5.2 Observations

This section summarizes the key observations and conclusions from this work.

5.2.1 Two-Dimensional Airfoil Simulations

1. The baseline Spalart-Allmaras model over-predicted lift at high angles of attack and over-predicted drag at low angles of attack.

2. Including transition modeling significantly improved the drag predictions for the two-dimensional airfoils. Large regions of laminar flow were seen on both the S809 and S827 airfoils at low angles of attack. Capturing the laminar regions with transition modeling lowered the predicted drag by 30% to 50% compared to the baseline SA model.

3. The transition modeling also improved lift predictions at low angles of attack by capturing laminar separation bubbles on both the upper and lower surfaces of both airfoils. The result was a 5% to 10% increase in predicted lift compared to the baseline SA model for angles of attack where the laminar separation bubbles were present.

4. The APG correction improved performance predictions in the post stall region by reducing the predicted angle of attack for stall. The angle of attack where stall was predicted for the S809 airfoil was reduced by 2° compared to the baseline SA model, resulting in a 13% reduction in the maximum predicted lift.

5. The S827 lift predictions were lowered by the inclusion of the APG correction for angles of attack above 6°, but the drop in lift at 6° was still not captured.

5.2.2   Three-Dimensional Rotor Simulations

1. Transition modeling noticeably changed the wind turbine performance predictions for the Sandia 100 m blade. The predictions of both power and thrust were increased by the inclusion of transition modeling, particularly at low wind speeds.

2. The transition model captured significant regions of laminar flow, particularly on the upwind surface. Capturing the laminar flow on the downwind surface led to lower surface pressures on the downwind surface, accounting for some of the difference in predicted performance.

3. Significant amounts of separated flow were predicted for the inboard third of the Sandia 100 m blade. The extent of separated flow was not significantly affected by the transition model.

4. Tubercles were found to have a minimal impact on wind turbine performance

at normal operating conditions, reducing predicted power and thrust by less than 1% compared to the baseline blade.

5. Adding tubercles significantly changed the spanwise distribution of in-plane sectional airloads in the region of the tubercles. Peaks in the sectional airloads occurred behind the tubercle troughs where there were isolated regions of low surface pressure. Higher surface pressures behind the tubercle crests led to lower sectional airloads at the crests. The low surface pressures in the tubercle troughs occurred because the flow going through the tubercle troughs was accelerated due to the tubercle geometry.

5.3   Key Contributions

The key contributions of this work are the following:

1. The GPU-RANS solver turbulence model was extended to include the $\gamma - Re_\theta - SA$ transition model.

2. Improvements in data caching on the GPU were implemented in the GPU-RANS solver. A 10% to 15% speedup was achieved by utilizing shared memory to cache data in the flux routines and the reconstruction routines.

3. The GPU-RANS solver was modified to include terms that allow arbitrary grid motion to be simulated. The grid motion terms can be used for modeling the rotation of wind turbine rotors.

4. The turbulence modeling modifications were validated for use with wind tur-

bine airfoils using the S809 experimental data. The need to further refine thetransition modeling and APG correction were highlighted by the inability to fully capture the performance characteristics of the S827 airfoil.

5. The importance of transition modeling for capturing large blade aerodynamic performance was demonstrated.

6. Leading edge tubercles were evaluated for a large pitch-controlled blade. It was shown that tubercles have minimal effect on turbine performance at nominal operating conditions.

5.4   Future Work

There are several directions in which this work could be extended:

1. The current transition model depends on empirical correlations and has only been rigorously validated for two dimensional flow and three dimensional flow without significant crossflow. Additional work investigating the transition modeling for crossflow and features like tubercles is needed for studying wind turbine performance in off design conditions.

2. The APG correction utilizes empirical correlations that have only been validated for two dimensional flows. The APG correction needs to be validated for three dimensional flows before it is can be applied with confidence to wind turbine simulations.

3. It was shown that leading edge tubercles do not significantly affect normal

115

operating performance. Since there are no significant performance penalties, the next step is to evaluate if leading edge tubercles provide any advantages to off design performance or blade structural dynamics. Conditions involving yawed flow and wind gusts are of particular interest.

4. It was observed that low speed simulations converged slowly, requiring two to three times as many timesteps for convergence. Improving the low Mach pre-conditioning should improve the convergence rate, decreasing the turnaround time for generating results for low wind speeds.

5. In this work, a rigid blade was assumed. In actuality, significant blade deflections are typically found on large blades. Coupling the aerodynamics predictions with a method to model the blade deflections and structural dynamics would improve predictions of wind turbine performance and provide important information about the aeroelastic behavior of the blade.

Chapter A: Appendix A: Hybrid FVM-RANS

RANS simulations typically require large numbers of mesh points, in part because it is necessary to extend the domain to prevent the creation of unrealistic numerical boundaries, as discussed in Section 2.5.7.4. It is possible to reduce the required size of the RANS domain by utilizing RANS only in regions where viscous and turbulent phenomena need to be accurately resolved. The reduced sized RANS domain can then be connected to a lower fidelity model that can be used for the rest of the flow domain. In the past, Sitaraman et al. [54] simulated flow through a helicopter rotor using a RANS model to simulate the near blade region and coupling it to a free-vortex method (FVM) that simulated the wake structure.

A.1   Free-Vortex Method (FVM)

The free vortex method utilized in this work discretizes the wake geometry into vortex filaments. The filament strength is calculated based on the bound circulation of the rotor blade. The bound circulation is determined based on the spanwise distribution of aerodynamic loading along the blade. The Biot–Savart law is used to calculate the mutual influence between vortex filaments. Filament convection velocity is calculated by combining the influences of all the other vortex filaments

with the free-stream velocity. The initial free wake structure is computed based on the aerodynamic loads calculated in the wake capturing simulations.

A.2   Wake Coupling

To couple the free wake structure to the RANS solver the far-field boundary condition in the RANS solver is modified. The far-field boundary is based on the combination of the free-stream velocity and the combined effects of the free wake structure. The vortex filament positions and strengths are input from the free wake structure. Then the field velocities are computed using the Biot–Savart law. The pressure is determined based on the velocity field using Bernoulli's equation. Density is calculated using the pressure field and isentropic relations. The Riemann invariant discussed in Section 2.5.7.4 is constructed using these calculated primitive variables instead of the free-stream values.

Bibliography

[1] U.S. Department of Energy, *20% Wind Energy by 2013: Increasing Wind Energys Contribution to U.S. Electricity Supply,* U.S. Department of Energy, DOE Report No. GO-102008-2567, July 2008.

[2] Manwell, J. F., McGowan, J. G., and Rogers, A. L., *Wind Energy Explained: Theory, Design, and Application,* Second Edition. John Wiley and Sons, 2009.

[3] Griffith, D. T., "The SNL100-01 blade: carbon design studies for the Sandia 100-meter blade," Sandia National Laboratories Technical Report No. SAND2013-1178, February 2013.

[4] TPI Composites, "Innovative design approaches for large wind turbine blades," Sandia National Laboratories Technical Report No. SAND2003-0723, March 2003.

[5] TPI Composites, "Innovative design approaches for large wind turbine blades – final report," Sandia National Laboratories Technical Report No. SAND2004-0074, May 2004.

[6] Standish, K. J., and van Dam, C. P., "Aerodynamic analysis of blunt trailing edge airfoils," *Journal of Solar Engineering,* Vol. 125, pp. 479-487, 2003.

[7] Griffith, D. T., and Ashwill, T. D., "The Sandia 100–meter All–glass Baseline Wind Turbine Blade: SNL100–00," Sandia National Laboratories Technical Report No. SAND2011-3779, June 2011.

[8] Somers, D. M., *Design and Experimental Results for the S809 Airfoil,* NREL Report No. SR-440-6918, January 1997.

[9] NASA, "National full-scale aerodynamics complex," published March 2, 2005. Retrieved from: http://www.nasa.gov/centers/ames/multimedia/images/2005/nfac.html

[10] Hand, M. M., Simms, D. A., Fingersh, L. J., Jager, D. W., Cotrell, J. R., Schreck, S., and Larwood, S. M., "Unsteady Aerodynamics Experiment Phase VI: Wind Tunnel Test Configurations and Available Data Campaigns," NREL Report No. TP-500-29955, December 2001.

[11] Butterfield, C. P., Musial, W. P., Scott, G. N., and Simms, D. A., "NREL Combined Experimental Final Report—Phase II," NREL Report No. TP-442-4807, August 1992.

[12] Johnson, W., "A comprehensive analytical model of rotorcraft aerodynamics and dynamics," NASA Report No. TM-81182, June 1980.

[13] Johnson, W., "Rotorcraft aerodynamic models for a Comprehensive Analysis," *American Helicopter Society 54th Annual Forum,* May 1998.

[14] Jonkman, J. M., and Buhl Jr., M. L., "FAST User's Guide," NREL Report No. EL-500-29798, 2005.

[15] Jonkman, J. M., "Modeling of the UAE wind turbine for refinement of FAST_AD," NREL Report No. TP-500-34755, December 2003.

[16] Laino, D.J., and Hansen, A.C., "Users Guide to the Wind Turbine Dynamics Computer Software AeroDyn," Windward Engineering, LC, August 2001.

[17] Somers, D. M., *Design and Experimental Results for the S827 Airfoil,* NREL Report No. SR-500-36345, January 2005.

[18] Lobitz, D. W., "Aeroelastic stability predictions for a MW-sized blade," *Wind Engineering,* Vol. 7, No. 3, pp 211-224, 2004.

[19] Resor, B., and Paquette, J., "Uncertainties in prediction of wind turbine blade flutter," In *52nd AIAA Structures, Structural Dynamics, and Materials Conference,* AIAA paper 2011-1947, 2011.

[20] *NVIDIA CUDA C Programming Guide,* NVIDIA, 2014.

[21] Dumitrescu, H., and Cardos, V., "Rotational effects on the boundary-layer flow in wind turbines," *AIAA Journal,* Vol. 42, No. 2, pp. 408-411, 2004.

[22] Medida, S., *Correlation-based transition modeling for external aerodynamic flows,* PhD Thesis, University of Maryland College Park, 2014.

[23] Simms, D., Schreck, S., Hand, M., and Fingersh, L. J., "NREL Unsteady Aerodynamics Experiment in the NASA-Ames Wind Tunnel: A Comparison of Predictions to Measurements," NREL Report No. TP-500-29494, June 2001.

[24] Duque, E., Burklund, M., and Johnson, W., "Navier-Stokes and Comprehensive Analysis Performance Predictions of the NREL Phase VI Experiment," *Journal of Solar Engineering,* Vol. 125, pp. 457-467, 2003.

[25] Leclerc, C., and Masson, C., "Predictions of aerodynamic performance and loads of HAWTS operating in unsteady conditions," In *1999 ASME Wind Energy Symposium,* AIAA paper 99-0066, 1999.

[26] Medida, S. and Baeder, J. D., "Adverse pressure gradient modification to turbulence models for wall-bounded flows," In *21st AIAA Computation Fluid Dynamics Conference,* AIAA Paper 2013-2426, 2013.

[27] Medida, S., and Baeder, J. D., "Application of the correlation-based $\gamma - Re_{\theta t}$ transition model to the Spalart-Allmaras turbulence model," In *20th AIAA Computational Fluid Dynamics Conference,* AIAA Paper 2011-3979, 2011.

[28] Xu, G., and Sankar, L. N., "Application of a viscous flow methodology to the NREL Phase VI rotor," In *2002 ASME Wind Energy Symposium,* AIAA paper 2002-0030, 2002.

[29] Benjanirat, S., Sankar, L. N., and Xu, G., "Evaluation of turbulence models for the prediction of wind turbine aerodynamics," In *41st Aerospace Sciences Meeting and Exhibit,* AIAA paper 2003-0517, 2003.

[30] Gorski, J. J., "A new near-wall formulation for the $k - \epsilon$ equations of turbulence," In *24th Aerospace Sciences Meeting,* AIAA paper 86-0556, 1986.

[31] Thomas, S., *A GPU-accelerated, hybrid FVM-RANS methodology for modeling rotorcraft brownout,* PhD Thesis, University of Maryland College Park, 2013.

[32] Vestas Wind Systems A/S, "Worlds most powerful wind turbine now operational," published January 28, 2014. Retireved from: http://www.vestas.com/en/media/ /media/eaf56b4c49964c8faf5f550ad0b1dec0.ashx

[33] Kooijman, H.J.T., Lindenburg, C., Winkelaar, D., and van der Hooft, E. L., "DOWEC 6 MW pre-design: aero-elastic modeling of the DOWEC 6 MW pre-

design in PHATAS," Energy Research Center of the Netherlands Report No. ECN-CX-01-135, September 2003.

[34] Fish, F. E., and Battle, J. M., "Hydrodynamic Design of the Humpback Whale Flipper," *Journal of Morphology,* Vol. 225, No. 1, pp. 51-60, 1995.

[35] Watts, P., and Fish, F. E., "The influence of passive, leading edge tubercles on wing performance," In *12th International Symposium on Unmanned Untethered Submersible Technology,* 2001.

[36] Fish, F. E., and Lauder, G. V., "Passive and Active Flow Control by Swimming Fishes and Mammals," *Annual Review of Fluid Mechanics,* Vol. 38, pp. 193-224, 2006.

[37] Sutherland, W., "The viscosity of gases and molecular force," *Philosophical Magazine,* Series 5, Vol. 36, No. 223, pp. 507-531. 1893.

[38] Blazek, J., *Computational Fluid Dynamics: Principles and Applications,* Second Edition. Elsevier Science, 2006.

[39] Van Leer, B., "Towards the ultimate conservative difference scheme: V. a second-order sequel to Godunov's method," *Journal of Computation Physics,* Vol. 32, No. 1, pp. 101-136, 1979.

[40] Koren, B., "Upwind schemes, multigrid and defect correction for the steady Navier-Stokes equations," In *Proceedings of the 11th International Conference on Numerical Methods in Fluid Dynamics,* 1988.

[41] Roe., P., "Approximate Riemann solvers, parameter vectors and difference schemes," *Journal of Computational Physics,* Vol. 135, No. 2, pp. 250-258, 1997.

[42] Launder, B. E., Reece, G. J., and Rode, W., "Progress in the development of a Reynolds-stress turbulent closure," *Journal of Fluid Mechanics,* Vol. 68, No. 3, pp. 537-566, 1975.

[43] Durbin, P., "A Reynolds stress model for near wall turbulence," *Journal of Fluid Mechanics,* Vol. 249, pp. 465-498, 1993.

[44] Spalart, P. R. and Allmaras, S. R., "A one-equation turbulence model for aerodynamic flows," *Recherche Aerospatiale,* No. 1, pp. 5-21, 1994.

[45] Spalart, P. R., Deck, S., Shur, M. L., Squires, K. D., Strelets, M. Kh., and Travin, A., "A new version of detached eddy simulation, resistant to ambiguous grid densities," *Theoretical Computational Fluid Dynamics,* Vol. 20, pp. 181-195, 2006.

[46] Scotti, A., Meneveau, C., and Lilly, D. K., "Generalized Smagorinsky model for anisotropic grids," *Physics of Fluids A: Fluid Dynamics,* Vol. 5, No. 9, 1993.

[47] Jameson, A. and Yoon, S., "Lower-upper implicit schemes with multiple grids for euler equations," *AIAA Journal,* Vol. 25, No. 7, pp. 929-935, 1987.

[48] Pulliam, T. H., and Chaussee, D. S., "A Diagonal Form of an Implicit Approximate-Factorization Algorithm," *Journal of Computational Physics,* Vol. 39, No. 2, pp. 347-363, 1981.

[49] Pulliam, T., "Time accuracy and use of implicit methods," In *11th AIAA Computational Fluid Dynamics Conference,* AIAA paper 1993-3360, 1993.

[50] Turkel, E., "Preconditioning techniques in computational fluid dynamics," *Annual Review of Fluid Mechanics,* Vol. 31, pp. 385-416, 1999.

[51] Lee, Y., *On overset grids connectivity and vortex tracking in rotorcraft CFD,* PhD Thesis, University of Maryland College Park, 2008.

[52] Lakshminarayan, V. K., *Computational investigation of micro-scale coaxial rotor aerodynamics in hover,* PhD Thesis, University of Maryland College Park, 2009.

[53] Corson, D. A., Griffith, D. T., Ashwill, T., and Shakib, F., "Investigating Aeroelastic Performance of Multi-MegaWatt Wind Turbine Rotors Using CFD," In *53rd Structural Dynamics and Materials Conference,* AIAA paper 2012-1827, 2012.

[54] Sitaraman, J., and Roget, B., "Prediction of helicopter maneuver loads using a coupled CFD/CSD analysis," 26th International Congress of the Aeronautical Sciences, 2008.